Synthesis and transport properties of nanostructured topological insulators

Vanda Pereira

CFisUC, Department of Physics

University of Coimbra

Supervisor

Prof. Dr. José António Paixão

This dissertation is submitted for the degree of

Master of Physics

September 2016

"Sempre chegamos ao sítio aonde nos esperam"

José Saramago, *A Viagem do Elefante*

Agradecimentos

Primeiramente, gostava de agradecer ao Professor Doutor José Antonio Paixão por me ter dado a oportunidade de estudar um tema tão apelativo e desafiante. Obrigada pela orientação, explicações e sugestões imprescindíveis para a realização deste trabalho.

Agradeço também à Marta, cuja amizade, companheirismo e experiência foram extremamente valiosos este ano. Obrigada por todo o apoio no trabalho laboratorial e ainda pelas sugestões e incentivos quando os resultados não eram os esperados.

À Professora Doutora Manuela Ramos Silva, agradeço o incentivo, os conselhos dados e a preparação laboratorial proporcionada no início deste mestrado.

Ao Anthony, Renan, Tomé e João, agradeço as longas conversas, toda a ajuda e, acima de tudo, os óptimos momentos partilhados ao longo destes cinco anos em Coimbra.

À Rita, Joana e Rafael, obrigada pelos anos (tantos!) de amizade e compreensão.

Aos meus pais, por serem o melhor exemplo que poderia ter. Obrigada pela presença constante, paciência, incentivos, carinho e amor incondicional.

Ao Emanuel, por me mostrar que a distância física não podia ser menos importante. Obrigada por, mesmo distante, me acompanhares em todos os passos. Obrigada pela ajuda e por acreditares sempre em mim.

A todos, muito obrigada.

Abstract

Topological insulators (TIs) are a new quantum state of matter that has attracted great interest due to their unique properties and potential applications in spintronics. These materials have an energy gap in the bulk, like an ordinary insulator, but have helical conducting states on the surface. These states arise from the combination of spin-orbit coupling and time reversal symmetry. Bismuth chalcogenides have been the most extensively studied materials due to their simple surface states and single Dirac cones. Bi_2Se_3, in particular, has an approximately ideal Dirac cone, which makes it particularly interesting as a prototype of topological insulators.

In this work, we synthesized Bi_2Se_3, $Bi_2Se_{3-x}Te_x$, $x = 0.1$, 0.3, 0.5 and Bi_2Te_3 by a microwave-assisted method. The structural, morphological and composition characterization of the nanocrystals was performed. Furthermore, the transport properties of two samples of Bi_2Se_3 were measured, one of them with impurity phases. In the analyzed nanomaterials one can observe weak anti-localization (WAL) effect, which can be modeled by the Hikami-Larkin-Nagaoka (HLN) formula, and also Shubnikov-de Haas oscillations. For both samples, the dependence of the phase coherence length l_ϕ with temperature followed the expected for a two-dimensional system ($l_\phi \sim T^{-1/2}$), suggesting the existence of 2D surface states in the gap of the 3D material. However, the Hall effect suggests that the bulk is not insulator and the bulk states are relevant to the transport properties.

The most important result of this work is that we have shown that polycrystalline samples of Bi_2Se_3, even those that are contaminated with parasitic phases, preserve the WAL effect. The relatively high coherence length of the electrons measured in the nanomaterial led us to conclude that the quantum phenomena of weak anti-localization and SdH oscillations are robust to the presence of non-magnetic impurities and structural defects.

Keywords: Topological insulator, weak anti-localization, Shubnikov-de Haas oscillations, magnetoresistance, nanostructured materials

Resumo

Os isoladores topológicos são um novo estado da matéria que tem suscitado grande interesse devido às suas propriedades únicas e a potenciais aplicações em spintrónica. Estes materiais possuem um *gap* energético no *bulk*, como os demais isoladores, mas possuem estados condutores helicoidais na superfície. Estes estados surgem da combinação do acoplamento spin-órbita e da simetria de reversão temporal. Os calcogenetos de bismuto têm sido os materiais estudados mais extensivamente devido aos seus estados de superfície simples e cones de Dirac únicos. Bi_2Se_3, nomeadamente, tem um cone de Dirac aproximadamente ideal, o que o torna particularmente interessante como protótipo dos isoladores topológicos.

Neste trabalho procedeu-se à síntese por micro-ondas de Bi_2Se_3, $Bi_2Se_{3-x}Te_x$, $x = 0.1, 0.3, 0.5$ e Bi_2Te_3, e à caracterização estrutural, morfológica e de composição dos nanocristais obtidos. Além disso, foi realizado o estudo das propriedades de transporte de duas amostras de Bi_2Se_3, uma das quais com fases correspondentes a impurezas. Os nanomateriais analisados possuem anti-localização fraca (WAL), que pode ser modelada pela fórmula de Hikami-Larkin-Nagaoka (HLN), bem como oscilações Shubnikov-de Haas. Para ambas as amostras, o comportamento do comprimento de coerência de fase l_ϕ com a temperatura segue o esperado para um sistema bidimensional ($l_\phi \sim T^{-1/2}$), evidenciando a existência de estados de superfície 2D existentes no *gap* do material 3D. No entanto, o efeito de Hall sugere que o *bulk* destas amostras não é isolador, sendo os estados de *bulk* relevantes para as propriedades de transporte.

O resultado mais importante deste trabalho reside no facto de se ter mostrado que as amostras policristalinas de Bi_2Se_3, mesmo aquelas contaminadas com fases parasíticas, preservam o efeito de WAL. Concluímos que, dado o relativamente elevado comprimento de coerência eletrónica medido no nanomaterial, os fenómenos quânticos de anti-localização fraca, bem como as oscilações quânticas SdH, são robustas à presença de impurezas não magnéticas e defeitos estruturais.

Palavras-chave: Isolador topológico, anti-localização fraca, oscilações Shubnikov-de Haas, magnetorresistência, materiais nanoestruturados

Contents

List of Figures

List of Tables

Nomenclature

Acronyms / Abbreviations

AC   Alternate current

ARPES Angle-resolved photoemission spectroscopy

BSE   Backscattered electrons

CFE   Counterflow heat exchanger

DOS   Density of states

DSP   Digital signal processor

EDS   Energy Dispersive X-Ray Spectometry

EG   Ethylene glycol

ETO   Electrical Transport Option

HLN   Hikami-Larkin-Nagaoka

IML   Intermediate lens

LL   Landau level

PPMS   Physical Property Measurement System

QH   Quantum Hall

QSH   Quantum Spin Hall

SDD   Silicon Drift Detector

SdH   Shubnikov-de Haas

SE   Secondary electrons

SEM   Scanning Electron Microscopy

SOC   Spin-orbit coupling

TI   Topological insulator

TKNN Thouless, Kohmoto, Nightingale, den Nijs

TR   Time-reverse

TRIM Time reversal invariant momentum

TRS   Time reversal symmetry

WAL Weak antilocalization

WL   Weak localization

XRD X-ray diffraction

Chapter 1

Introduction

In condensed-matter physics, the order of a state of matter is usually described by the symmetries they spontaneously break: crystalline solids, magnets and superconductors are therefore described by translational, rotational and gauge symmetries, respectively. In the recent years a new state of matter has emerged, where no spontaneous break of symmetry occurs. Instead, its behavior depends only on the topology. These materials, the topological insulators (TIs), are therefore a new class of materials with important quantum-mechanical properties. These have a typical insulator behavior in the bulk, with separated conduction and valence bands, while having conducting states at the surface. However, these were not the first class of topological materials. The first example of a quantum state with no spontaneous break of symmetry was the Quantum Hall (QH) state, discovered in 1980 [1]. The QH effect is verified in electronic systems subjected to strong magnetic fields and it consists of a conducting channel along the boundary, the edge state, around the insulating bulk. This state defines a topological phase since some properties, as the quantized Hall conductance, are insensitive to smooth changes and only change when the system undergoes a phase transition.

A few years later, in 1988, Haldane proposed that QH effect could occur even in the absence of a macroscopic magnetic field [2]. Alternatively, the electrons would move on a lattice and would be driven by forces resulting from their motion in the said crystal lattice, analogue to the Lorentz force for an electric charge in a magnetic field [3]. More recent studies replaced those forces by the spin-orbit coupling, a relativistic effect in which the degrees of freedom of the spin and momentum are coupled, causing the electrons to feel a spin-dependent force. In 2003 some simplified models were introduced [4], showing that spin-orbit coupling could lead to quantum spin Hall (QSH) effect, although it does not break time-reversal symmetry. Note that this is opposite to what happens in the QH state, where the applied magnetic field breaks time-reversal symmetry. The

quantum spin Hall effect can be regarded as a combination of two quantum Hall states, where electrons with spin-up or spin-down will move in opposite directions in the edge. However, these models were not realistic, since they failed, for example, to predict if the QSH would survive the addition of impurities [5]. In 2005 Kane and Mele proposed a more realistic model similar to a graphene model with spin-orbit coupling (SOC) [6]. Here, SOC acts as spin-dependent magnetic field for the electron spins, aligning them in relation to the momentum direction and, therefore, causing spin polarization.

However, the graphene used to build the model could not be used to experimentally observe the QSH effect, since the spin-orbit coupling in this material is very weak. But another theoretical advance was made in 2006 by Bernevig, Hughes and Zhang [7], who predicted that CdTe/HgTe/CdTe quantum wells should give rise to a 2D topological phase. One year later, this prediction was verified by König et al. [8], where the quantized charge conductance was observed, as a plateau similar to what happens in the quantum Hall effect, but in zero magnetic field. Hence, this was the first experimental observation of a 2D topological insulator.

Although there is no quantum Hall state in 3D, the topological insulator state can be generalized to a three-dimensional state. However, it is a subtle generalization and is considered as one of the milestones in the topological insulators field [9, 10]. It consists of an evolution of the edge states based on the intrinsic band structure. Thus, the 1D edge states in the QSH effect would evolve into 2D surface states in three-dimensional topological insulators [11].

For a topological insulator to form there must exist a strong spin-orbit coupling, in order to modify the band structure significantly. Since spin-orbit coupling is a relativistic effect, obtained as a consequence of the Dirac equation in the nonrelativistic limit, only heavy elements will have a strong interaction and the Dirac fermion physics (with linear energy dispersion relations) becomes relevant. Pure bismuth is a semimetal with a strong spin-orbit coupling. Besides that, the most promising candidates seem to be semiconductors with small bandgaps, since the bandgap should not be much larger than the energy-scale of SOC. Bi_xSb_{1-x} was the first material predicted to be a three-dimensional topological insulator [12], in 2007. The experimental verification occurred soon after that by Hsieh et al. [13]. Its unusual surface bands were observed by angle-resolved photoemission spectroscopy (ARPES). This technique uses a high-energy photon to eject an electron from a crystal. The bulk or surface electronic structure can then be determined by the analysis of the momentum of the projected electron. High-resolution ARPES allows to separate the surface states from that of the bulk, since the former do not disperse in the direction perpendicular to the surface, while bulk states do. The

experimental discovery of Bi_xSb_{1-x} motivated a search for other topological insulators, namely ones with simpler surface states and larger band gaps, since that would allow to observe topological insulator phases at higher temperatures. The new generation of topological insulators of Bi_2Se_3 and Bi_2Te_3 have simpler surface states predicted by theory and confirmed by ARPES. In addition, they are pure compounds, rather than alloys like Bi_xSb_{1-x}, which would, in principle, favor the higher purity of the synthesis [14].

However, not every material is suitable for ARPES, which demands good quality single crystals. When these are not available, transport experiments are used to confirm the TI materials. One should confirm that the transport is surface-dominant and that the carriers are Dirac fermions. Some of the properties of these materials can help to characterize them. Dirac fermions are known to acquire a Berry phase of π when the wave vector is rotated along a closed path [15]. This π Berry phase leads to a destructive interference between two time-reversed paths, which leads to the weak anti-localization effect. Besides that, when a crystalline solid is subjected to high magnetic fields, the Landau quantization leads to oscillation phenomena generally called quantum oscillations [16]. Since the phase factor of the oscillations is related to the Berry phase, one can therefore understand if the electrons responsible for the oscillations are Dirac fermions and, ultimately, confirm the TI nature of the material. This is important since there are other phenomena, as trivial accumulation or inversion layers, that may cause surface-dominated transport [16].

The possible applications in spintronics and quantum computing, closely related to the transport properties of these materials, have created a great interest for this unique state of matter. The study of such an interesting "hot topic" in physics, coupled to the importance of the transport properties in TIs, are the motivation for this work. Therefore, the goal of this thesis is the synthesis of materials with possible topological insulator phases, namely Bi_2Se_3, $Bi_2Se_{3-x}Te_x$, $x = 0.1$, 0.3, 0.5 and Bi_2Te_3, and their characterization via Powder X-Ray Diffraction, Scanning Electron Microscopy and transport measurements using a magnetometer.

The dissertation is structured as follows: **Chapter 2** is dedicated to the introductory aspects of the topology in topological insulators. Concepts as the Berry phase, the $\mathbb{Z}_2$ topology, two and three-dimensional TIs are discussed in this chapter. A short introduction to the materials of our interest is also presented. In **Chapter 3** we discuss the theoretical aspects of the transport properties in the scope of this thesis. The weak localization and anti-localization effects are presented, as well as the quantum oscillations observed in the resistivity. The **Chapter 4** consists of a description of the experimental

methods, including the equipment used on the synthesis and characterization measurements. In **Chapter 5** a presentation and discussion of the results is reported. The first six sections are dedicated to the characterization and morphology studies of the synthesized compounds, whereas in the last three sections we report the transport properties measured in three samples. Finally, in **Chapter 6**, the conclusions and suggestions for further work are presented.

Chapter 2

Topology in Topological Insulators

2.1   Topology and Band Theory

One of the goals of condensed matter physics is to characterize phases of matter. One of the common ways to understand the phases of certain materials is the symmetries they spontaneously break. However, there are some phases that cannot be understood in those terms. In the recent decades, it was discovered that the quantum Hall state, that does not break any symmetries, can be described in terms of topological order. Some of the properties of this state, such as the quantized Hall conductivity and the number of conducting edge modes, can be understood as consequences of the topological structure of the state. With the recent discovery of topological insulator materials, the interest in the study of topological order increased. In order to understand the concepts of topological order, it is necessary to review the key elements of topology and band theory.

Topology is a branch of mathematics dedicated to the study of objects insensitive to smooth deformations. One of the most well known and illustrative examples is the example of closed two-dimensional surfaces in 3-dimensions. A sphere can be smoothly deformed into a disk, but it can never be smoothly deformed into the surface of a doughnut. These two surfaces are topologically distinct. The topological invariant is, in this case, called the genus, g, which is essentially the number of holes. Integers cannot change smoothly and, consequently, surfaces with different genus cannot be deformed into one another. On the other hand, surfaces with the same genus are said to be topologically equivalent.

For surfaces, the topological invariant that characterize an object can be determined by the Gauss-Bonnet theorem. It states that the integral of the Gaussian curvature, K,

over a surface defines an integer topological invariant, known as Euler characteristic,

$$\chi = \frac{1}{2\pi} \int_S K \, dA. \tag{2.1}$$

This invariant is directly related to the genus by $\chi = 2 - 2g$.

Although this was an illustrative example, the principles concerning topological insulators are similar. The topological invariant will, however, describe more abstract objects. In fact, topology for electronic materials is caused by the "foldings" of the wave function of the electrons. The topology in cause is then the topology of the Hilbert space.

Similarly to what was described for the two-dimensional surfaces, insulators are said to be equivalent if they can be interchanged by slowly changing the Hamiltonian, maintaining the system in the ground state. The equivalence can be understood in terms of adiabatic continuity. The scale of how low the adiabatic process must be is defined by the energy gap, E_G. Therefore, if there is an adiabatic path connecting two insulators with the energy gap remaining finite, the insulators are topologically equivalent. Also, if two inequivalent insulators are connected, the energy gap must be zero at some point, causing a phase transition.

Assuming that the material is crystalline, the translation symmetry allows the single particle states to be labeled by their momentum $\mathbf{k}$. These states can be written according to Bloch's theorem

$$|\psi(\mathbf{k})\rangle = e^{i\mathbf{k}\cdot\mathbf{r}} |u(\mathbf{k})\rangle, \tag{2.2}$$

where $|u(\mathbf{k})\rangle$ is a cell periodic eigenstate of the Bloch Hamiltonian,

$$\mathcal{H}(\mathbf{k}) = e^{i\mathbf{k}\cdot\mathbf{r}} \mathcal{H} e^{-i\mathbf{k}\cdot\mathbf{r}}. \tag{2.3}$$

The eigenvalues $E_m(\mathbf{k})$ and eigenstates $|u_m(\mathbf{k})\rangle$ define the energy bands that collectively form the band structure of the solid, m being the band index.

All conventional insulators are equivalent and equivalent to the vacuum (from Dirac's theory, vacuum has an energy gap for pair production, a conduction band for electrons and a valence band for positrons). However, not all electronic states with an energy gap are equivalent, the simplest being the quantum Hall state described in section 2.3.

2.2   Berry Phase

The Berry phase is an important notion in the discussions of topological phases. It arises from the intrinsic phase ambiguity of a quantum mechanical wave function: the Bloch states are invariant under the transformation

$$|u(\mathbf{k})\rangle \rightarrow e^{i\phi(\mathbf{k})} |u(\mathbf{k})\rangle . \tag{2.4}$$

Thus, when $\mathbf{k}$ is transported around a closed loop, the Bloch state $|u(\mathbf{k})\rangle$ acquires a well defined Berry phase. The Berry connection, $\mathbf{A}$, is defined as

$$\mathbf{A} = -i \langle u(\mathbf{k})| \nabla_{\mathbf{k}} |u(\mathbf{k})\rangle . \tag{2.5}$$

Besides that, one can also define the Berry curvature as

$$\mathcal{F} = \nabla \times \mathbf{A}. \tag{2.6}$$

The Berry phase is given by the line integral of the Berry connection or, according to Stokes' theorem, by the surface integral of the Berry flux,

$$\gamma_C = \oint_C \mathbf{A} \cdot d\mathbf{k} = \int_S \mathcal{F} \, d^2\mathbf{k}. \tag{2.7}$$

In a quantum-mechanical system, the Berry phase is the accumulated phase factor when completing a closed path in the parameter space. Furthermore, the Berry connection has a similar role to the vector potential for electromagnetic fields, corresponding to the gauge field defined in that parameter space.

2.3   Integer Quantum Hall Effect and TKNN invariant

The Quantum Hall state occurs when an electron gas confined to two dimensions is placed in a strong magnetic field. In these conditions, the electron's circular orbit is quantized with cyclotron frequency $\omega_c = eB/m$, leading to quantized Landau levels with energy $E_m = (m + \frac{1}{2})\hbar\omega_c$.

This state is similar to an ordinary insulator in the sense that an energy gap separates the N occupied Landau levels from the empty states. The Landau levels can therefore be viewed as a band structure. However, an electric field causes an Hall current charac-

terized by

$$\sigma_{xy} = \frac{Ne^2}{h}. \tag{2.8}$$

The quantum Hall state differs from an ordinary insulator by their topologies. The Chern invariant is a topological invariant $n \in \mathbb{Z}$ that can be interpreted as the invariant that characterizes the classes of $\mathcal{H}(\mathbf{k})$ that can be continuously deformed into one another. Physically it can be understood in terms of the Berry phase [17] associated with the Bloch wave functions $|u_m(\mathbf{k})\rangle$. The Chern invariant is the total Berry flux in the Brillouin zone,

$$n_m = \frac{1}{2\pi} \int_S \mathcal{F}_m d^2\mathbf{k}. \tag{2.9}$$

The total Chern number n is a sum over all the occupied bands (N),

$$n = \sum_{m=1}^{N} n_m. \tag{2.10}$$

If we take a path encircling the Brillouin zone, n_m (and therefore n) can only be an integer multiple of 2π, due to the single-valued nature of the wave-function.

Thouless, Kohmoto, Nightingale and den Nijs (TKNN) [18] showed that the integer in the quantized Hall conductivity (eq. 2.8) is the Chern number n. This is why this invariant is also known as TKNN invariant. Thus, since n is a topological invariant, it cannot change when the Hamiltonian changes smoothly, which helps to understand the robust quantization of σ_{xy}. Moreover, the conductivity σ_{xy} is quantized to integer multiples of e^2/h.

As was referred in section 2.1, the integral of the Gaussian curvature over a surface defines a topological invariant. Similarly, the Chern number is an integral of a related curvature, the Berry curvature.

The topological classification of gapped band structures has a consequence of extreme importance: if there is an interface where the topological invariant changes, there must exist a gapless conducting state at the interface. Considering an interface between the quantum Hall state and the vacuum, one can understand the edge states in terms of the skipping motion of the electron (Fig. 2.1(a)). It is known that a charged particle in a uniform magnetic field will cycle around the magnetic flux due to the Lorentz force. When the particle is close to the boundary, its trajectory is interrupted and the particle bounces back from the rigid boundary and skips along it. The electronic states responsible for this motion propagate only in one direction along the edge, forming a
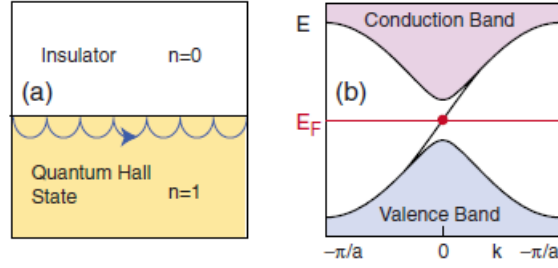
Figure 2.1: Interface between an ordinary insulator and the QH state. (a) Skipping motion of the particles near the boundary. (b) Existence of a conducting channel connecting the valence and conduction bands. [14]

conducting channel along the boundary, called the edge state (Fig. 2.1(b)).

Furthermore, since the group velocity of the particles in the bulk is much slower than that of the cyclotron, the electrons in the bulk are localized by impurities or disorders. The particles on the edge, on the contrary, have a higher group velocity and are not affected by impurities or disorders. Thus, the edge state constitutes a perfect one-dimensional conducting channel.

2.4 $\mathbb{Z}_2$ Topological Invariant

The distinction between an ordinary insulator and a topological insulator is suggested by the robustness of its edge states. This state is characterized by a topological invariant, called the $\mathbb{Z}_2$ invariant. This index nomenclature comes from the group of integer numbers $\mathbb{Z}$ and, specifically, the $\mathbb{Z}_2$ quotient group that classifies even and odd numbers. The $\mathbb{Z}_2$ index gives a classification based on parity. In a very simple way, the invariant expresses if the number of times that the one-dimensional edge state crosses the Fermi level between 0 and π/a (with a the lattice constant) is even or odd [16].

2.4.1 Time reversal symmetry (TRS)

The time reversal (TR) operator for spin $^1/_2$ particles is given by

$$\Theta = e^{i\pi S_y/\hbar} K, \tag{2.11}$$

where S_y is the spin operator and K is the complex conjugate operator. The operator satisfies $\Theta^2 = -1$.
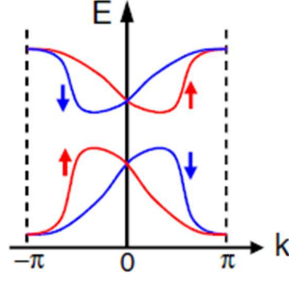
Figure 2.2: Kramers pairs of bands. Each pair of bands are degenerated at the TRIMs. [16]

A time reversal Bloch Hamiltonian must satisfy

$$\Theta\mathcal{H}(\mathbf{k})\Theta^{-1} = \mathcal{H}(-\mathbf{k}). \tag{2.12}$$

This identity proves the existence of Kramers pairs, i.e., that the energy bands of a TR system have the same energy for $+\mathbf{k}$ and $-\mathbf{k}$. Each pair of bands are degenerate at the time reversal invariant momentum (TRIM), where $+\mathbf{k}$ and $-\mathbf{k}$ become equivalent due to the periodicity of the Brillouin zone. At values of $\mathbf{k}$ other than the correspondent for TRIMs, the degeneracy is lifted by the spin-orbit coupling, as illustrated in Figure 2.2.

Equation 2.12 also allows to classify the classes of Hamiltonians that can be slowly deformed into one another without closing the energy gap.

Therefore, additionally to the TKNN classification of quantum Hall states, there is another classification ($\mathbb{Z}_2$ index) for time invariant systems with possible values 1 or 0 [6] that applies to TI in two and three dimensions.

2.4.2 $\mathbb{Z}_2$ index formulas

The formulation presented next for the $\mathbb{Z}_2$ invariant follows the approach reported by Fu and Kane [19].

It is convenient to represent the TR operator in the Bloch wave function basis as a matrix. A convenient matrix is

$$w_{\alpha\beta} = \langle u_\alpha(\mathbf{k})| \Theta |u_\beta(-\mathbf{k})\rangle, \tag{2.13}$$

with α and β the band indices. This matrix relates to the Bloch states by

$$|u_\alpha(-\mathbf{k})\rangle = \sum_\beta w_{\alpha\beta}^*(\mathbf{k})\Theta \,|u_\beta(\mathbf{k})\rangle . \qquad (2.14)$$

$w_{\alpha\beta}$ is an unitary matrix with the following property:

$$w_{\beta\alpha}(-\mathbf{k}) = -w_{\alpha\beta}(\mathbf{k}). \qquad (2.15)$$

This means that at a TRIM $\mathbf{\Lambda}_a$ (where $\mathbf{k}$ and $-\mathbf{k}$ coincide), the w matrix becomes antisymmetric, i.e.,

$$w_{\beta\alpha}(\mathbf{\Lambda}_a) = -w_{\alpha\beta}(\mathbf{\Lambda}_a). \qquad (2.16)$$

Pfaffian is generally defined for an antisymmetric matrix and can be related to the determinant by

$$\text{Pf}[A]^2 = \det[A]. \qquad (2.17)$$

Therefore, we can define

$$\delta_a = \frac{\text{Pf}[w(\mathbf{\Lambda}_a)]}{\sqrt{\det[w(\mathbf{\Lambda}_a)]}} = \pm 1. \qquad (2.18)$$

The $\mathbb{Z}_2$ topological invariant ν is given by

$$(-1)^\nu = \prod_{a=1}^{4} \delta_a. \qquad (2.19)$$

This invariant classifies the two-dimensional insulators according to their Hilbert spaces: "twisted" if $\nu = 1$ and trivial if $\nu = 0$.

One can extend this formulation to 3D systems and its physical origin can be easily understood. For simplicity, consider a cubic system with lattice constant $a = 1$ (See Fig. 2.3). In the Brillouin zone of this system there are eight TRIMs denoted by Λ_{n_1,n_2,n_3} where the Bloch Hamiltonian becomes TR symmetric, with $\Theta\mathcal{H}(\mathbf{\Lambda}_{n_1,n_2,n_3})\Theta^{-1} = \mathcal{H}(-\mathbf{\Lambda}_{n_1,n_2,n_3})$. The six planes of the 3D Brillouin zone each have the same symmetries described for the 2D system, and therefore they can be described by a $\mathbb{Z}_2$ invariant. However, those six invariants are not all independent and only four invariants can be independently determined [16]. Using the definition in equation 2.18, we can write the
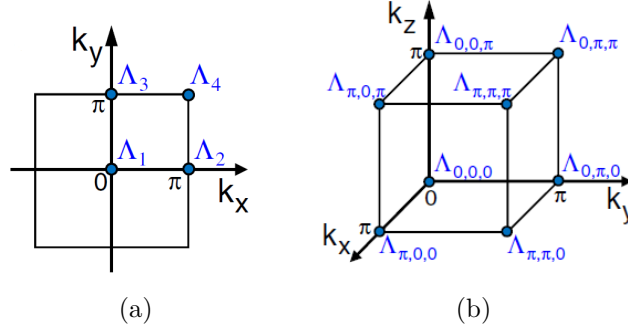
Figure 2.3: Time-reversal invariant momenta for (a) a square 2D Brillouin zone and (b) a cubic Brillouin zone. [16]

four invariants as

$$(-1)^{\nu_0} = \prod_{n_j=0,\pi} \delta(\Lambda_{n_1,n_2,n_3}), \qquad (2.20)$$

$$(-1)^{\nu_i} = \prod_{n_{j\neq i}=0,\pi;n_i=\pi} \delta(\Lambda_{n_1,n_2,n_3}) \qquad (i=1,2,3). \qquad (2.21)$$

Thus, the ν_0 invariant is given by the product of all eight TRIMs, and it is a unique feature for a 3D system. ν_i, however, is a product of four TRIMs, and is similar to the $\mathbb{Z}_2$ invariant defined for bidimensional systems.

2.5 Two-dimensional TI: Quantum Spin Hall Effect

While quantum Hall states require an external magnetic field, which breaks the time-reversal symmetry, the quantum spin Hall (QSH) states are time-reversal invariant and do not need an applied magnetic field.

The QSH insulators are essentially two copies of the QH state with opposite chiralities. It has an upper edge constituted by a forward mover with spin-up and a backward mover with spin-down, and vice-versa for the lower edge.

Kane and Mele [20] described the QSH insulator starting from a graphene model with spin-orbit coupling. The SOC is then responsible for the locking of the spin to the orbital motion of the electron and, therefore, the counterpropagation of opposite spin states characteristic of this state. Taken separately, the Hamiltonians for the spins up and down violate time-reversal symmetry. However, in an applied electric field, the up and down spins have Hall currents in opposite directions that cancel each other, recovering the overall time-reversal symmetry. But a spin current $\mathbf{J}_S = (\hbar/2e)(\mathbf{J}_\uparrow - \mathbf{J}_\downarrow)$

is generated, with a spin Hall conductivity given by $\sigma_{xy}^S = e/2\pi$, thus the name "quantum spin Hall effect".

The previous discussion was held considering the conservation of spin, which does not happen in real systems. The quantized Hall conductivity is just an artifact of a simplified model, invalidated for any real system. However, the QSH state, being two copies of the quantum Hall state, also has gapless edge states. These states, unlike the quantized Hall conductivity, are robust even when spin conservation is violated. The quantum spin Hall edge states always respect the property that the up spins propagate in one direction and the down spins propagate in the opposite, known as "helical", in analogy with the helicity[1] of a particle. They form a unique 1D conductor not susceptible to Anderson localization [21] usual for conductors in disordered systems. On the contrary, those states cannot be localized even for strong disorder. Unless time-reversal symmetry (TRS) is broken, an incident electron will be transmitted perfectly through the region with disorder. Thus, the edge states are protected by time reversal symmetry.

In graphene the conduction and valence bands touch each other in two points in the Brillouin zone. Near those points the electronic dispersion is linear and it can be described by employing the Dirac equation with the rest mass set to zero [22]. The dispersion is therefore called a Dirac cone and the electrons behave as massless Dirac fermions.

Kane and Mele model showed that SOC leads to an opening of a gap at the crossing point of the cone - the Dirac point [16] and that a pair of spin-polarized states with TRS appear at the edge. The spin-polarization of the edge states would be achieved due to the SOC, which has an inherent tendency to align spins in relation to the momentum direction of the electrons. The electrons in the gapless edge states behave has one-dimensional Dirac fermions without mass within the gap opened in the bidimensional Dirac cone. Thus, the bulk electrons behave as two-dimensional massive Dirac fermions due to the finite energy gap at the Dirac point [16].

The two-dimensional topological insulators can be classified by the $\mathbb{Z}_2$ invariant. Consider the Figure 2.4, which illustrates the surface states between two TR invariant points now denoted by $\Gamma_a = 0$ and $\Gamma_b = \pi/a$. In Fig. 2.4(a), the two states connect pairwise, intersecting the Fermi energy an even number of times. The surface states are topologically trivial because disorder can cause the edge states to be eliminated, pushing the surface bands above or bellow E_F. However, in Fig. 2.4(b), the bands intersect E_F an odd number of times, and the edge states cannot be eliminated. Therefore, topologically trivial states will be characterized by $\nu = 0$, while the quantum spin Hall insulator will

---

[1]Correlation between spin and momentum of a particle.
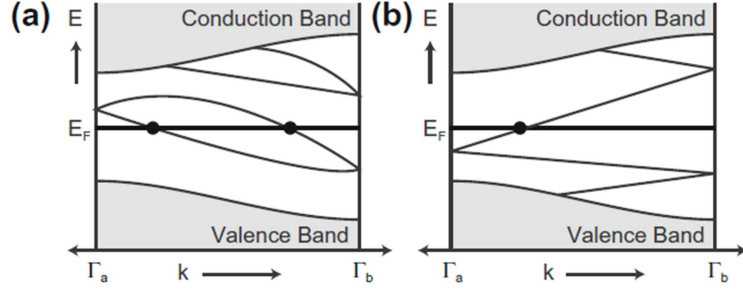
Figure 2.4: Electronic dispersion between two Kramers points labeled as $\Gamma_a = 0$ and $\Gamma_b = \pi/a$. (a) has an even number of states crossing the Fermi energy, while in (b) it is odd. [23]

have $\nu = 1$.

2.6 Three-dimensional TI

The picture of the linear dispersion of the states at their crossing point can be easily generalized into three dimensions. In a 3D topological insulator, the surface states consist of bidimensional Dirac fermions and the dispersion forms a Dirac cone. The crossing point, like in the 2D case, is called the Dirac point and is located at a TR-invariant point.

One of the most interesting properties of the TIs is that they carry a Berry phase of π. This is generally applied to Dirac fermions, as first reported by Ando et al. [15]. The Dirac equation is given by

$$E\psi(\mathbf{r}) = \left(c\mathbf{p} \cdot \alpha + mc^2\beta\right)\psi(\mathbf{r}), \tag{2.22}$$

where m is the rest mass of particle, and α and β are the Dirac matrices, related to the Pauli matrices. The energy eigenvalue of this equation is $E = \pm c\sqrt{\mathbf{p}^2 + mc^2}$. For a two-dimensional massless system with Fermi velocity v_F, the Dirac equation reduces to

$$E\psi(\mathbf{r}) = \hbar v_F \boldsymbol{\sigma} \cdot \hat{\mathbf{k}}\psi(\boldsymbol{r}) = -i\hbar v_F \boldsymbol{\sigma} \cdot \nabla\psi(\mathbf{r}), \tag{2.23}$$

with $\boldsymbol{\sigma} = (\sigma_x, \sigma_y)$ the Pauli matrices and $\hat{\mathbf{k}} = \left(\hat{k}_x, \hat{k}_y\right)$ a wave vector operator defined by $\hat{\mathbf{k}} = -i\nabla$. The eigenfunctions are

$$\psi_\pm(\mathbf{r}) = \frac{1}{\sqrt{2}}\begin{pmatrix} e^{-i\theta(\mathbf{k})/2} \\ \pm e^{i\theta(\mathbf{k})/2} \end{pmatrix}e^{i\mathbf{k}\cdot\mathbf{r}} = u_\pm(\mathbf{k})e^{i\mathbf{k}\cdot\mathbf{r}}, \tag{2.24}$$

with $\theta(\mathbf{k}) = \arctan(k_y/k_x)$. Furthermore, the energy eigenvalues are now given by

$$E_\pm = \pm \hbar v_{\mathrm{F}} k. \tag{2.25}$$

Using equations 2.5 and 2.7, the Berry phase acquired when $\mathbf{k}$ is adiabatically rotated anticlockwise along a closed path C can be calculated as

$$\gamma_C = \oint_C d\mathbf{k} \cdot i \left\langle u_\pm(\mathbf{k}) \right| \nabla_\mathbf{k} \left| u_\pm(\mathbf{k}) \right\rangle = \pi. \tag{2.26}$$

Regarding the classification of these materials, a three-dimensional TI is characterized by four $\mathbb{Z}_2$ topological invariants $(\nu_0; \nu_1\nu_2\nu_3)$ [9, 24, 25]. The 2D surface states of a 3D crystal contain four time-reversal invariant points, $\Gamma_{1,2,3,4}$ in the surface Brillouin zone, where the surface states must be Kramers degenerate. Those points form the 2D Dirac points in the surface band structure. As illustrated in Fig. 2.4, the Fermi surface can intersect a line between two TRIM Γ_a and Γ_b an even or odd number of times. This can be characterized by the four bulk $\mathbb{Z}_2$ invariants.

2.6.1   Weak Topological Insulator

The simplest three-dimensional topological insulator is formed by layering 2D versions, similar to layered quantum Hall states. Figure 2.5(a) illustrates the Fermi surface for coupled layers of quantum spin Hall insulators, stacked along the y direction. In this case, a surface band intersects the Fermi energy between Γ_1 and Γ_2 and between Γ_3 and Γ_4, leading to a non-trivial electronic dispersion similar to Fig. 2.4(b). A weak topological insulator is characterized by $\nu_0 = 0$ and $\nu_i = 1$ for some $i = 1, 2, 3$. The indices ν_i can be interpreted as Miller indices to specify the directions of the layers.

However, this state differs from the 2D case in the sense that the surface states are not protected by time-reversal symmetry. They can, in fact, be localized due to the presence of disorder.

2.6.2   Strong Topological Insulator

A strong topological insulator consists of a distinct phase related in a more subtle way to the 2D quantum spin Hall insulator. In this case $\nu_0 = 1$. This invariant is related to the number of TR invariant points that are enclosed by the Fermi surface circle. In a strong TI, the Fermi circle encloses an odd number of Dirac points. When only one Dirac point is enclosed, we are in the presence of the simplest case of a 3D strong topological insulator (Figs. 2.5(b) and 2.5(c)).
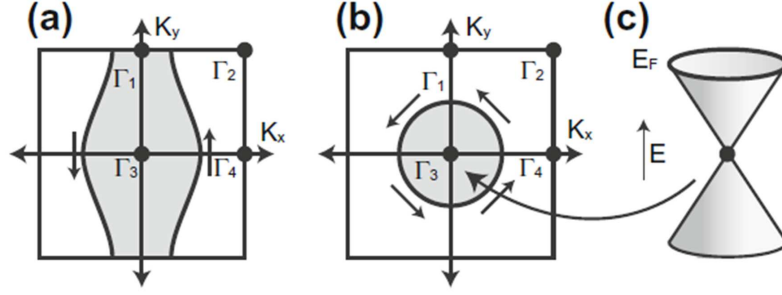
Figure 2.5: Fermi surfaces in the surface of a Brillouin zone for (a) a weak topological insulator and (b) a strong topological insulator. (c) illustrates the simplest case with only one Dirac point. [23]

The surface states of a 3D TI form a unique bidimensional metal. While in a regular metal every point at the Fermi surface has up and down spins, in a TI the TR symmetry requires that states with $\mathbf{k}$ and $-\mathbf{k}$ have opposite spins. This will cause the rotation of the spin with $\mathbf{k}$ around the Fermi circle, leading to an accumulated Berry phase. When an electron encloses a Dirac point, the Berry phase will have a value of π. The Berry phase has important consequences, such as the behavior in a magnetic field (to be discussed in Chapter 3) and the impossibility of localization of the surface states, even for strong disorder. In this sense, the surface states of a 3D strong topological insulator are similar to the edge states in a quantum spin Hall insulator.

2.7   Topological Insulator Materials: Bi_2Se_3 and Bi_2Te_3

Bi_2Se_3 and Bi_2Te_3 are known to be excellent thermoelectric materials, and have been investigated recurrently in the past decades. In the last few years a new interest has arisen in the study of these materials, as they were found to be topological insulators with rather simple surface states. Those are, in fact, the most extensively studied three-dimensional topological insulators. In 2009 the topological surface states of these materials were successfully confirmed by angle-resolved photoemission spectroscopy (ARPES), revealing a nearly idealized single Dirac cone for Bi_2Se_3.

The two compounds share the same structure, with quintuple layers bonded by covalent bonds, stacked as T-Bi-T-Bi-T, with T=Se, Te. Those quintuple layers are connected to each other by weak van der Waals forces, which causes them to cleave easily.

These systems are characterized by the $\mathbb{Z}_2$ invariant $(1;000)$, which means that they are strong topological insulators ($\nu_0 = 1$) with the Dirac cone centered at the Γ point of the surface of the Brillouin zone (see Fig. 2.7). These materials have been a popular
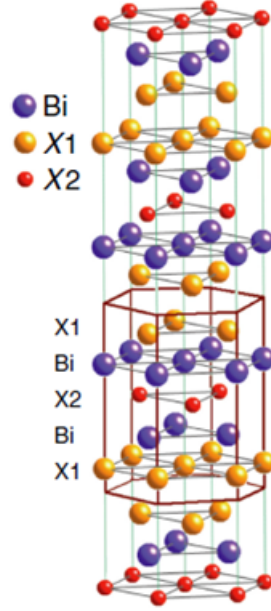
Figure 2.6: Crystal structure of Bi_2Se_3 and Bi_2Te_3, with X1, X2=Se, Te. [16]
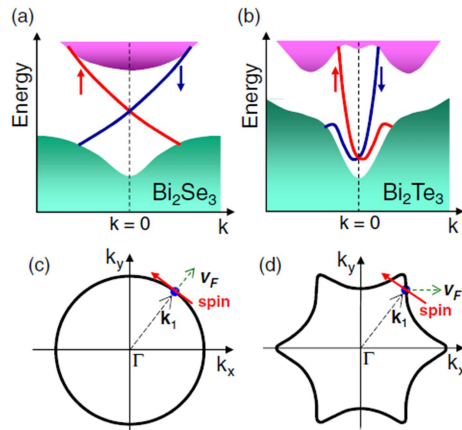
Figure 2.7: Bulk and surface structures for (a) Bi_2Se_3 and (b) Bi_2Te_3. (c) and (d) represent the constant-energy contours of the Dirac cones for the same compounds. [16]

choice in the study of topological insulators due to their simple surface states and the absence of non-topological surface states [16].

However, studying the transport properties of these compounds is not so simple, due to the large residual bulk carriers. Bi_2Se_3, for example, is always n-type because of Se vacancies. In order to overcome those crystalline defects, physicists have tried material doping [26, 27], nanostructuring [28] and electrical gating [29] to reduce the bulk carriers. Moreover, mixing Bi_2Se_3 and Bi_2Te_3 along with Sb_2Te_3 (other well known and characterized TI) in ternary and quaternary compounds has been done with the aim to improve the bulk insulating properties.

Chapter 3

Transport Properties in TIs

It is predicted that the topological insulators have exotic properties closely related to the spin quantum transport, and with possible applications in spintronics and quantum computing. Thus, in the last years, a great amount of studies related to the transport properties of this new quantum state of matter have been reported.

In this chapter we will present the relevant transport properties that were also focus of study in the present work. In the next section, the weak anti-localization (commonly observed in TIs) will be presented, starting from the more common effect observed in ordinary metals, the weak localization effect. The second section will cover the quantum oscillations in TIs, namely the Shubnikov-de Haas oscillations.

3.1 Weak Localization and Weak Anti-localization Effects

For a rectangular two-dimensional conductor, one can relate the conductance, $G = 1/R$, and the conductivity, σ, by:

$$G = \sigma \frac{W}{L}, \tag{3.1}$$

where W and L are the width and length of the sample, respectively. However, when these dimensions are decreased to a certain point, the ohmic behavior no longer holds. The question is then how small can those dimensions be so that the ohmic behavior is still preserved. The answer relies on the relation between three characteristic lengths that classify the transport in solids. Those are the already referred sample size, L; the mean free path l, that measures the average distance an electron travels before its momentum is changed due to elastic scattering; and the phase coherence length, l_ϕ,
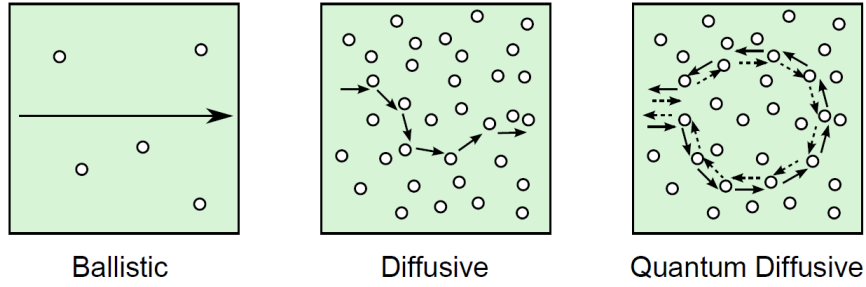
Figure 3.1: Different transport regimes in solids. Impurities are represented by the white circles, while the trajectories of the electrons are represented by arrows. [30]

which is the average distance an electron maintains phase coherence.

The three electronic transport regimes in solids are the ballistic, diffusive and quantum diffusive, as illustrated in Figure 3.1. In the first, $l \gg L$, and the electrons can go through the sample without being scattered. On the other hand, if $l \ll L$, we are in the diffusive regime, and electrons will suffer from scattering. This regime has two different behaviors depending on the phase coherence length, l_ϕ. If $l_\phi \leq l$, it is called semiclassical diffusion, and the conductivity is given by Drude model. In the opposite limit, if $l_\phi \gg l$, the regime is called quantum diffusive and the phase coherence will be maintained, even though the electron suffers from scattering several times. In this regime, a quantum interference between two time-reversed loops (see Fig. 3.1-right) arises, causing a correction to the usual conductivity. The weak (anti-)localization effect appears as a consequence of this correction.

3.1.1 Weak Localization

In a disordered system, the path of an electron depends on the scattering events it suffers. Consider an electron moving from point m to point n. The total probability $R(m \rightarrow n)$ that an electron goes from m to n is given by squaring the sum of the amplitudes of all the possible trajectories connecting both points:

$$R(m \rightarrow n) = |A_1(m{\rightarrow}n) + A_2(m{\rightarrow}n) + \ldots|^2. \tag{3.2}$$

Usually, the interference effects between different paths do not have any relevance, since the phases are random and, in average, cancel out. In this case the previous equation would be equivalent to the sum of the squares of the different amplitudes.

However, when the initial and final points are the same, something different happens. Consider a path starting and ending at the same point m:

$$m \to m_1 \to m_2 \ldots m_{N-1} \to m_N \to m$$

To every path like this, there is a time-reversed path that is obtained by reversing the arrows:

$$m \to m_N \to m_{N-1} \ldots m_2 \to m_1 \to m$$

Thus, the probability can be seen as the sum of the amplitudes for two different sets, one with index i referring to the first path, and other, with index iR referring to the time-reversed path:

$$R(m \to m) = |(A_1 + A_2 + \ldots) + (A_{1R} + A_{2R} + \ldots)|^2 \equiv |A + A_R|^2. \qquad (3.3)$$

In systems with time-reversal symmetry and in the absence of magnetic field, the amplitudes for a carrier propagating clockwise or counterclockwise is equal, $A = A_R$. Hence, the probability is given by

$$R(m \to m) = 4\,|A|^2. \qquad (3.4)$$

On the other hand, in the classical case where there is no interference between the paths, the probability would be

$$R(m \to m) = |A|^2 + |A_R|^2 = 2\,|A|^2. \qquad (3.5)$$

Therefore, the constructive coherence between the two time-reversed paths causes an enhanced probability that the electron scatters in a loop. As a consequence, the electrons are more localized, leading to an increase in the resistivity. Experimentally, it can be seen as an increase in the resistivity (hence, decrease in conductivity) as the temperature decreases, as long as the temperature is low enough for interference to be observed, as illustrated in Figure 3.2(b).

3.1.2 Weak Anti-localization

The weak anti-localization effect is conceptually very similar to the weak localization. In the case of TIs, the phase shift of π acquired when an electron travels along a closed path (the Berry phase discussed in section 2.6) causes the time-reversed paths to interfere destructively. This effect can, however, occur in systems with strong SOC.
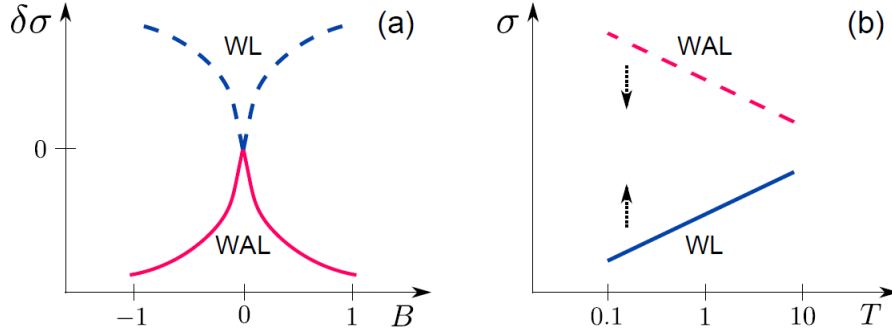
Figure 3.2: Signatures of WL and WAL as a function of (a) the applied magnetic field and (b) the temperature. [30]

A similar phase change occurs in a system with strong spin-orbit coupling, where scattering from an impurity causes a spin rotation, since the spin and momentum are locked. In fact, an electron can contour the impurity by taking a clockwise or counterclockwise turn around it. As the momentum rotates, the spin will rotate by an angle of π or $-\pi$, respectively. This is schematically represented in Figure 3.3. Consequently, the electron spin of the two time-reversed paths differ by $\pi - (-\pi) = 2\pi$. Yet, the wave function for a spin $1/2$ particle acquires a negative sign when the spin undergoes a 2π rotation. Therefore, the amplitudes of the two sets discussed in eq. 3.3 are now related by $A = -A_R$. The probability that an electron travels from a point m to the same point is now:

$$R(m \rightarrow m) = |A + A_R|^2 = 0. \tag{3.6}$$

The interference between the two time-reversed paths is therefore destructive, which reduces the probability of electrons to localize and, consequently, reduces the resistivity. Its dependence with temperature can also be seen in Fig. 3.2(b).

3.1.3 Hikami-Larkin-Nagaoka (HLN) formula

When a magnetic field is applied, the time-reversal symmetry is destroyed and, naturally, the two paths no longer interfere constructively/destructively (WL/WAL). In that sense, the WL/WAL effects are protected by time-reversal symmetry. As a result, a sharp cusp in the conductivity can be observed around $B = 0$ (see Figure 3.2(a)). The magnetic field causes a negative magnetoconductivity in the case of WAL and the opposite for WL.

The magnetic field dependence of the conductivity in 2D systems was reported by
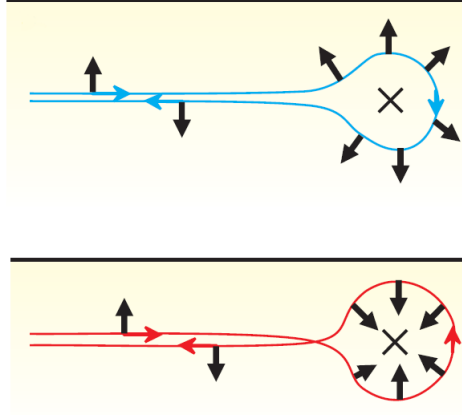
Figure 3.3: When an electron suffers from scattering from a nonmagnetic impurity, it can be scattered in two directions: clockwise along the blue curve (spin rotates by π) or counterclockwise along the red curve (spin rotates by $-\pi$). This leads to a spin rotation of 2π, causing destructive interference. [31]

Hikami, Larkin and Nagaoka in 1980 [32]. The HLN formula represents the change in conductivity with respect to its value in the absence of a magnetic field and it is given in equation 3.7, where Ψ is the digamma function, l_ϕ is the phase coherence length, and the prefactor α is positive for WL and negative for WAL.

$$\Delta\sigma_{xx} = \alpha \frac{e^2}{\pi h} \left[\Psi\left(\frac{\hbar c}{4el_\phi^2 B} + \frac{1}{2} \right) - \ln\left(\frac{\hbar c}{4el_\phi^2 B} \right) \right] \tag{3.7}$$

For the weak anti-localization effect, α should be $-1/2$ for each transport channel with a π Berry phase. In experiments, α was found to have values between around -0.4 and -1.1 , indicating the presence of one or two surface bands contributing to the weak anti-localization effect [33–35]. One can usually find $\alpha \sim -1/2$ in thin films, because the top and bottom surfaces form only one diffusive transport channel [16]. This happens when the thickness of the sample is shorter than l_ϕ, causing the electrons to travel between the two surfaces, through the bulk state, without losing the phase memory.

The weak anti-localization effect was rapidly observed after the discovery of Bi_2Se_3 and Bi_2Te_3 as topological insulators. The poor sample quality causes the mean free path, l, to be short ($\sim 10\,\text{nm}$). The phase coherence length in TIs is, however, of the order of 100-1000 nm. Thereafter, at low temperatures, these materials are in the quantum diffusive regime, where the WAL can occur. The WAL effect is, then, robust to non-magnetic impurities. However, the presence of magnetic impurities will lift the TR symmetry between the two paths, suppressing the WAL cusp [36].

3.2   Shubnikov-de Haas oscillations

A topological insulator should have a completely insulator bulk, and any transport should be carried by the surface states. However, in real cases this is not verified, as the bulk always has residual carriers due to defects or impurities. Therefore, the transport measurements always take into account both the bulk and surface states. Then, one can understand the importance of distinguishing between transport from the 2D surface states or the 3D bulk states. The quantum oscillations offer a way to do so.

The quantum oscillations can be measured in any property that depends on the density of states (DOS). The oscillations observed in conductivity are called Shubnikov-de Haas (SdH) oscillations, while the oscillations occurring in magnetic susceptibility are de Haas-van Alphen. Our focus of interest relies on SdH oscillations, discussed next.

Consider once again electrons confined to two dimensions in the presence of a strong magnetic field. The Landau quantization of the energy states will take place and the DOS will become periodically modulated as a function of the magnetic field. This can be understood since the Landau levels (LL) are separated by $\hbar\omega_c$, with $\omega_c = eB/m$. As the magnetic field is increased, the spacing between the LLs will increase, and the highest LL will be pushed through the Fermi energy, $E_{\rm F}$ (fewer LLs are filled). When $E_{\rm F}$ is positioned at the center of a LL, the DOS will be maximum. On the other hand, when $E_{\rm F}$ lies between two Landau levels, DOS will take a minimum (see Fig. 3.4). In the latter, a minimum in the conductivity σ_{xx} will occur, since a certain amount of LLs are completely filled and the next LL is empty. Therefore, a minimum in the DOS represents a minimum in the conductivity. This simplified vision helps to understand why the conductivity has oscillatory phenomena.

The SdH oscillations are periodic in $1/B$ and the oscillatory part of the longitudinal conductivity is described by

$$\Delta\sigma_{xx} \sim \cos\left[2\pi\left(\frac{F}{B} - \gamma\right)\right], \tag{3.8}$$

where F is frequency of the oscillation and γ is a phase shift. This factor also appears in the Onsager's quantization condition

$$A_n = \frac{2\pi e}{\hbar}B\left(n + \gamma\right), \tag{3.9}$$

with A_n the area enclosed by electrons in the k-space. This relation holds when the n-th LL is crossing the Fermi energy. γ is given by [33]

$$\gamma = \frac{1}{2} - \frac{\gamma_C}{2\pi} - \delta, \tag{3.10}$$
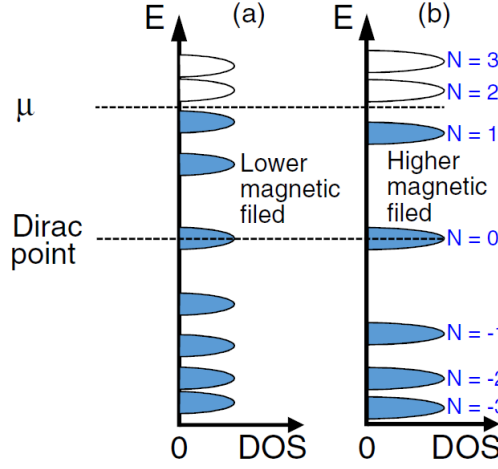
Figure 3.4: Landau quantization; μ is the Fermi level. For a higher magnetic field, the spacing between LLs increase and less Landau levels are occupied. [16]

where γ_C is the Berry phase, which takes values of 0 for a conventional metal and π for Dirac systems, and δ is the phase shift correction determined by the dimensionality of Fermi surface [33], with $\delta = 0$ for 2D Fermi surfaces and $\delta = \pm 1/8$ for 3D Fermi surfaces. Given that $A_n = \pi k_\text{F}^2$, then eq. 3.9 can be written as

$$2\pi(n+\gamma) = \pi k_\text{F}^2 \frac{\hbar}{eB}, \tag{3.11}$$

where $\hbar$ is the reduced Planck constant, e is the electronic charge, B the applied magnetic field and (πk_F^2) the cross-sectional area of the Fermi surface perpendicular to B with radius equivalent to the Fermi wave vector k_F.

Experimentally, γ can be determined from the so-called LL fan diagram. This diagram plots successive values of $1/B$ correspondent to the minimums and maximums of σ_{xx} versus the Landau level n. As discussed earlier, the minimums of σ_{xx} are assigned to integer values of n, while half integers, $n + 1/2$, are assigned to maximums. The plot should make a straight line with slope $F = \frac{\hbar}{2\pi e}\pi k_\text{F}^2$ corresponding to the oscillation frequency. When the linear fit is extrapolated to $1/B \to 0$, the intercept on the n-axis gives the SdH phase γ. For conventional metals, $\gamma = 1/2$ [33]. However, γ gets a non-trivial contribution from the Berry phase of the electrons.

The principal interest in the study of the SdH oscillation is the fact that it is possible to characterize the 2D surface states coexisting with the bulk states. This can be done by taking the dependence of F with the angle between the surface normal and the magnetic field direction, θ. When a wide range of angles is considered, and if the measured frequency changes with $\sim 1/\cos\theta$, then one can conclude with acceptable precision that

the oscillations come from a 2D system. Note that it is necessary that a wide range of θ is considered (e.g., up to 50°), because the SdH oscillations originated from a 3D system with an elongated Fermi surface can also cause the frequency to change in a similar way for smaller angles [16]. Furthermore, for $\theta = 90°$, the SdH oscillations should disappear only if they originate from 2D states.

Thus, when combining the study of the dependence of the SdH oscillations on the angle θ, and the phase γ obtained from the LL fan-diagram, one can confirm the nature of the quantum oscillations.

Chapter 4

Experimental Methods

4.1   Synthesis

Many methods have been proposed for the synthesis of binary bismuth chalcogenides, such as the solvothermal method, metalorganic chemical vapor deposition method and Bridgman technique. However, for these approaches, it is usually needed long reaction times, high temperatures and energy consumption, and toxic solvents [37, 38]. One can overcome this using the microwave-assisted polyol method used in this work. Microwave heating in inorganic chemistry had its first applications in the late 1980´s [39]. In the past decades, it also has attracted much attention in the synthesis of nanostructured materials. Microwave irradiation is more efficient than conventional heating, since it directly transmits the energy into the molecules present in the reaction mixture. This causes an uniform, rapid, heating, opposite to what usually happens with conventional heating, where the reaction vessel temperature can be higher than that of the solution. The rapid heating can therefore reduce the reaction time by orders of magnitude and increase product yield [37].

In this work, stoichiometric ratio of bismuth nitrate ($Bi(NO_3)_3 \cdot 5H_2O$, 99.99 %, Sigma-Aldrich), sodium selenide (Na_2SeO_3, 99 %, Alfa Aesar), sodium tellurite (Na_2TeO_3, 99.5 %, Alfa Aesar) and also potassium hydroxide were dissolved in ethylene glycol, stirred and microwave-heated for short periods of time at 180 °C and with a maximum power of 1000 W. When cooled, the product was separated by centrifugation and washed with water and ethanol. The synthesized nanosheets of Bi_2Se_3 and Bi_2Te_3 are more likely to manifest surface effects, since they have larger surface-to-volume ratios than bulk materials. Moreover, the synthesis was performed recurring to a microwave-assisted polyol method. In this method, the polyol (in this case ethylene glycol) acts both as the solvent and the reducing agent [37, 40–42]. Furthermore, the high permanent dipole of the EG

makes it an excellent susceptor for microwave radiation, leading to overheating, what causes an increased reduction ability [41]. The polyol process consists of three steps. First, the precursor is dissolved in the polyol. The dissolved species will then be reduced by the polyol and finally the polyol serves as a medium for the nucleation and growth of the particles [40]. Several articles [42, 43] suggest two possible paths, consisting of atomic (Path A) or ionic (Path B) mechanisms, represented in the following scheme:

| Path A | • $Bi^{3+} \rightarrow Bi^0$
 • $Bi^0 + T^0 \rightarrow Bi_2T_3$ |
| Path B | • $T^0 \rightarrow T^{2-}$
 • $T^{2-} + Bi^{3+} \rightarrow Bi_2T_3$ |
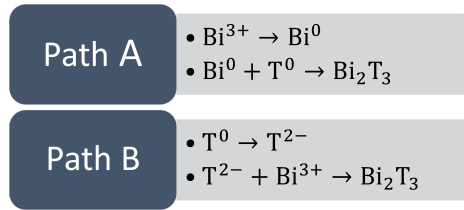
However, more recent studies [37, 41] showed that the process involved is, in fact, ionic. At high temperatures, the ethylene glycol oxidizes to acetaldehyde, used as a reducing agent (Eq. 4.1). The precursor including T=Se, Te (Na_2TO_3) dissociates, forming TO_3^{2-} in solution. Those ions are reduced by EG, forming elemental T (Eq. 4.2). In an alkaline medium (obtained by adding KOH), the freshly generated T produces T^{2-} through disproportionation (Eq. 4.3). Finally, the T^{2-} ions react with the metallic ion Bi^{3+}, forming Bi_2T_3 (Eq. 4.4).

$$2C_2H_6O_2 \rightarrow 2CH_3CHO + 2H_2O \tag{4.1}$$

$$2CH_3CHO + TO_3^{2-} \rightarrow 2CH_3COO^- + T + H_2O \tag{4.2}$$

$$3T + 6OH^- \rightarrow TO_3^{2-} + 2T^{2-} + 3H_2O \tag{4.3}$$

$$3T^{2-} + 2Bi^{3+} \rightarrow Bi_2T_3 \tag{4.4}$$
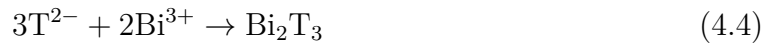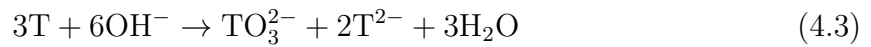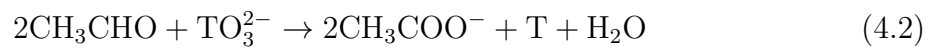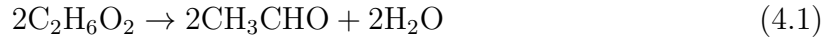
The synthesis was performed in a Milestone Start D Microwave Digestion System (Fig. 4.1). This is equipped with 6 high pressure vessels (SK-10 rotors), with a volume of 100 mL. It includes a reference segment, used for temperature control, and 5 standard segments. The equipment has an industrial magnetron and its typical delivered power is 1200 W, allowing rapid heating. Moreover, a rotating diffuser located above the microwave cavity evenly distributes microwaves throughout the cavity, preventing localized hot and cold spots.
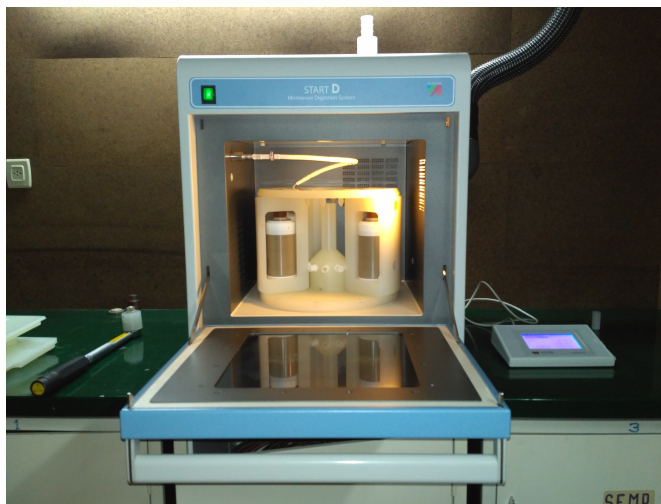
Figure 4.1: Milestone Start D Microwave Digestion System used in this work.

4.2 Structural Characterization: Powder X-ray Diffraction

4.2.1 Introduction

Although nowadays we know the crystalline structure of many materials, whether we are talking about simple materials as metals or more complex as proteins and organic molecules with many atoms, there is a constant need to study the structure of new materials, in order to understand and predict its properties. This can be accomplished using the right techniques. Since the interatomic distances in a crystalline material have the same order of magnitude as the typical X-ray wavelength, these can be diffracted by crystalline structures. Therefore, X-rays are the ideal radiation for these studies.

Powder X-ray diffraction (XRD) is the most convenient method when the sample in study is a polycrystalline material or even when it is obtained as a mixture of phases. One then needs to characterise the sample beyond its elemental composition and identify the phases and, ideally, quantify them.

The experimental equipment can be divided into techniques using parallel beam and focusing methods (as the Bragg-Brentano geometry). The latter was used in this work and will be described in detail later.
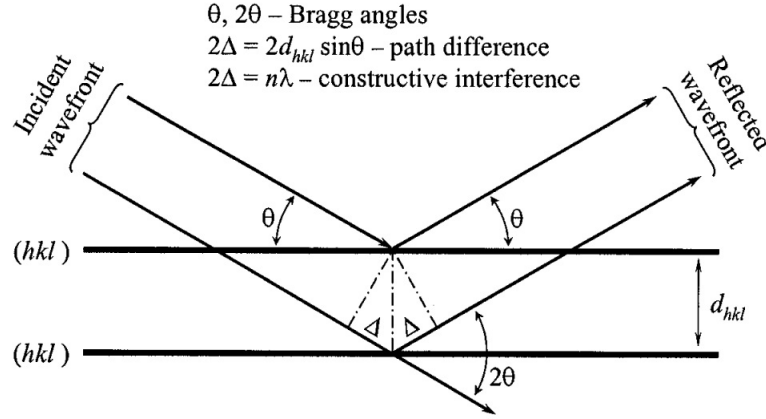
Figure 4.2: Bragg reflection from a set of parallel planes. [44]

4.2.2 X-ray diffraction theory

Although both protons and electrons interact with electromagnetic waves such as X-rays, the fact that electrons are much lighter particles makes their contribution for scattering more prominent. Hence, in a crystal structure the X-rays are scattered by the electrons of the atoms, making possible to determine the electron density. As the crystal structure is periodic, it is possible to determine the constitution of a unit cell from the XRD diffraction pattern.

In 1913, Sir Lawrence Bragg gave a simple, but convincing explanation of the diffraction patterns characteristic of crystalline materials. Consider a set of parallel planes (h, k, l) equally spaced by a distance d. In order to observe an intense beam emerging from the crystal, the beams reflected by consecutive planes must interfere constructively. That condition is given by

$$2d_{hkl} \sin \theta = n\lambda, \tag{4.5}$$

where λ is the wavelength, θ is the angle of incidence, d_{hlk} is the distance between planes of a family of planes and n is the order of the reflection, i.e., for $n = 1, 2, ...$ we get reflections of first, second order, etc. Equation 4.5 states that there is constructive interference when the path length difference between two incident waves is a multiple number of the wavelength.

The scattered amplitude from a unit cell is the structure factor F_{hkl}, defined as

$$F_{hkl} = \sum_{j}^{N} f_j \, \exp[2i\pi(hx_j + ky_i + lz_i)], \tag{4.6}$$

where f_j is the atomic scattering factor for the jth atom in the unit cell with coordinates x_j , y_j and z_j. Each structure factor represents a diffracted beam with amplitude $|F_{hkl}|$ and a relative phase ϕ_{hkl}. One can then write its mathematical relationship as

$$F_{hkl} = |F_{hkl}| \exp(i\phi_{hkl}) \tag{4.7}$$

The intensity of the diffracted beam is proportional to the square of its amplitude,

$$I_{hkl} \propto |F_{hkl}|^2 . \tag{4.8}$$

The experiment consists in measuring the intensity of the scattered beam as a function of the scattering angle. The diffraction pattern is a sum of the individual peaks and a background function. For materials with several phases or polycrystalline materials with complex unit cells, the Bragg peaks can overlap. Thus, it is convenient to fit a model to the entire pattern, refining it against the experimental data. This can be performed by minimization techniques. One of these techniques is the Rietveld method, where the minimized quantity is a weighted sum of the squares of the difference between the calculated and observed patterns.

4.2.3 XRD Equipment

In this work we used a Bruker AXS D8 ADVANCE diffractometer (Fig. 4.3) with DAVINCI design, which provides automatic change of the diffraction geometry. This equipment can operate in parallel beam geometry and Bragg-Brentano parafocusing geometry. Some of its components are listed as follows:

- ceramic sealed tube with a Copper tube ($K_\alpha = 1.5418\,\text{Å}$) which generates the X-rays;

- compact XYZ table which allows the adjustment of the sample position;

- vertical goniometer, where the combination of stepper motors with optical encoders ensures precise positioning of both arms where the source and the detector are placed. It can work in the $\theta - \theta$ or $\theta - 2\theta$ modes;

- LYNXEYE detector, a compound silicon strip detector with 192 strips covering an angular range of $\sim 3^{\text{o}}$. It has a maximum global count rate $> 100,000,000$ cps.

- for parallel beam geometry: Göbel mirror with 40 mm graded multi-layer optics tuned for Cu radiation. This creates a highly parallel beam and suppresses K_β radiation.

Figure 4.3: Bruker AXS D8 ADVANCE X-ray diffractometer. [45]
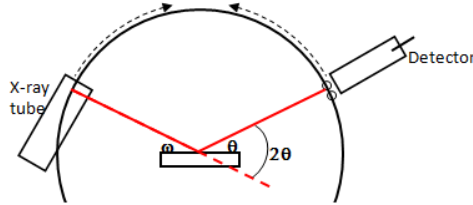
Figure 4.4: Bragg-Brentano geometry. [46]

- for Bragg-Brentano geometry:

    - variable divergence slit controlled by a stepper motor and two sets of Soller slits, controlling the axial divergence: attenuates the divergence of the incident beam before interacting with the sample and the divergence of the diffracted beam before it reaches the detector;

    - 0.02 mm Ni filter, in order to eliminate the β component of the Cu anode ($\text{K}_\beta \approx 1.39\,\text{Å}$). Ni foil is the ideal filter since its absorption edge is $\sim 1.54\,\text{Å}$, just above the wavelength of the K_β line [44].

In the geometry used in this work - Bragg-Brentano parafocusing geometry (see Fig. 4.4) - both the incident and diffracted beams form an angle θ with the surface of the sample. The divergence of the latter is controlled by a Soller slit and eventually it will converge at a receiving slit.

In order to identify the phases we used the ICDD PDF-4+ 2015 database in the DIFFRAC.SUITE EVA 3.0 software. Once this was successfully achieved, DIFFRAC.SUITE TOPAS V5 was used to perform a quantitative analysis.

4.3 Scanning Electron Microscopy (SEM)

4.3.1 Introduction

The resolving power of a microscope is not only limited by the number and quality of the lenses but also by the wavelength of the light used for illumination. The wavelength of the visible light is considerably high and, therefore, the limit of resolution of an optical instrument is rather low. Since electrons have shorter wavelengths, the microscope resolution is better, and we can characterize materials in the micro to nanometer range. Since the invention of scanning electron microscopy in 1937 by von Ardenne, its applications have covered a vast range of subjects, from physics, to biology or medicine.

The SEM scans a focused electron beam over a surface to create an image. It operates in a high vacuum and the samples must be electrically conductive, at least at the surface. If they are not naturally conductive, they are therefore usually coated with an ultrathin coating of electrically conducting material.

Energy Dispersive X-Ray Spectometry (EDS) can be coupled to the SEM, allowing to obtain relevant information on the chemical composition of the specimen.

4.3.2 Fundamental principles

The scanning electron microscope uses a focused beam of high-energy electrons to generate a variety of signals that derive from electron-sample interactions. These are not confined to the sample surface, and can also occur in the bulk, revealing information about the sample, including its morphology, chemical composition, and crystalline structure.

We can classify the electron-sample interactions in two different types, namely elastic and inelastic interactions, which we will discuss next.

4.3.2.1 Elastic Interactions

When an elastic interaction occurs, no energy is transferred from the incident electron to the sample. This happens when the electrons pass through the sample without interacting at all, contributing to the direct beam. But it can also happen when an electron is elastically deflected from its path by a Coulomb interaction with the positive potential of the nucleus, with a force F given by

$$F = \frac{Q_1 Q_2}{4\pi\varepsilon_0 r^2}.$$

$$(4.9)$$
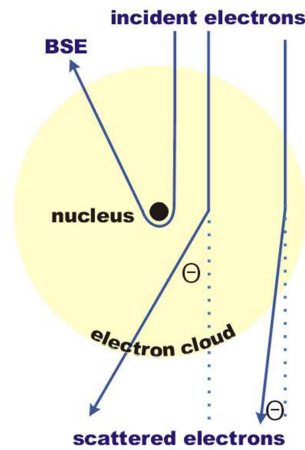
Figure 4.5: Scattering of an electron inside the electron cloud of an atom. [47]

One one hand, we can point the dependence of F on the charge: the Coulomb interaction increases with the atomic number Z. Therefore, the areas with heavier atoms will appear with darker contrast than those of lighter atoms. On the other hand, the closer the electron is to the nucleus, the stronger the interaction will be and, consequently, the scattering angle will increase (Fig. 4.5). This can lead to scattering into high angles and even backscattering (typically when the electron hits a nucleus, producing backscattered electrons, BSE). The latter are most valuable for illustrating contrasts in composition in multiphase samples.

4.3.2.2   Inelastic Interactions

If part of the energy of the incident electron is transferred to the sample, we are in the presence of an inelastic interaction. Several processes can occur, leading to different signals, such as inner-shell ionization, braking radiation and secondary electrons, which will be described as follows.

Inner-shell radiation   The incident electron can transfer energy to an electron localized in any of the atom's electron shells. If the energy is sufficient, it can cause the latter to be ejected from the sample. When this happens, the atom is left in an excited state, where an inner shell (with lower energy) has an electron vacancy, whereas the levels of higher energy are fully occupied. In order to return to the ground state, an electron from a higher shell drops to fill the vacancy. The difference in energy can be released by two processes: the Auger process and characteristic X-rays. In the former, the energy released when the electron falls into the vacancy is transferred to another electron, which is ejected from the sample - Auger electron. The kinetic energy of this electron

corresponds to the difference between the energy of the initial electronic transition and the ionization energy for the electron shell from which the Auger electron originated. Since these electrons are easily absorbed, only the Auger electrons created close to the surface can escape the sample. In the characteristic X-ray process, the energy difference is released by the emission of photons with an energy equivalent to the energy difference of the transition. Each element has a unique set of energy levels, and thus the transition produces a unique set of X-rays, which are characteristic to each element. Therefore, X-ray emission can help to characterize the elemental composition of the sample, using the Energy Dispersive X-ray Spectrometry.

Braking radiation   Also known as *Bremsstrahlung*, the braking radiation is produced by the deceleration of an incident electron in the Coulomb field of the atoms in the sample. The electron loses kinetic energy, which is converted into a photon. *Bremsstrahlung* has a continuous spectrum and is the main constituent of the continuous background in a X-ray spectrum.

Secondary Electron (SE)   Secondary electrons can originate from electrons located in the outer shell that are ejected from the sample or electrons ejected from the inner shell of the specimen by inelastic scattering with the electron beam. These are low-energy (<50 eV) electrons, which originate within a few nanometers from the sample surface. These are therefore most valuable for showing morphology and topography on samples.

4.3.3   SEM Equipment

The experimental system used in this work was a TESCAN VEGA3 SBH SEM. The scanning electron microscope swipes an electron beam over the sample, located in the microscope chamber. The quality of the images depends on the parameters of the electron probe: spot size, aperture angle and beam intensity.

The spot size determines the resolution of the microscope and the magnification. It is considered as a circular spot with a Gaussian intensity profile and it reduces at shorter working distances (distance between the lower objective and the focused surface of the specimen). The aperture angle is the vertex angle of the cone-shaped incident electron beam. The wider the cone, the lower the depth of focus. Finally, the beam intensity is the number of electrons passing through the probe in a specific time. The image noise of the electron microscope is related to the beam intensity. Thus, at lower beam intensities, a larger time for imaging scanning is needed, and vice-versa.

Since the incident beam parameters influence each other, it is their combination that allows the equipment to operate in different modes.

The SEM has two main parts: the electron column, where the electron beam is produced, and the detection system, which will be described in the next subsections.

4.3.3.1 Electron Column

The column of the microscope (Fig. 4.6) consists of the following main parts [48]:

- The *electron gun* consists of a cathode, Wehnelt cylinder and anode.The first two components are connected to the negative electric potential, whereas the anode and the remaining part of the column are at earth potential. The cathode is a tungsten filament that needs to be heated to high temperatures in order to cause the emission of free electrons. The voltage between the Wehnelt cylinder and the anode determinates the accelerating voltage of electrons and therefore their energy. The emission current is changed by maintaining the Wehnelt cylinder at a more negative voltage than the cathode. The system can produce an electron beam with a dimension of 25-50 μm, an energy from 200 eV to 30 keV and an emission current up to 300 μA.

- The *gun centering* allows to tilt the electron beam so that it enters the axis of the optical system of the column. It is formed by a system of electromagnetic deflection coils under the gun.

- The *spray aperture* is placed under the coils referred above and its function is to collimate the electron beam.

- The *condensers C1 and C2* are strong magnetic lenses used to demagnify the spot size that the electron beam produces. The higher the excitation of the condenser, the shorter its focal length and the higher its demagnification.

- The *final aperture* is placed under the condenser C2 and it cuts the size of the final incident beam.

- The *intermediate lens IML* is a magnetic lens used for the aperture change of the beam caused by the final aperture.

- The *stigmator* is an electromagnetic octupole that compensates for astigmatism.

- The *scanning coils* are formed by two sets of deflection coils that deflect the beam off the optical axis and later return it onto the axis. A scanning ramp connects the
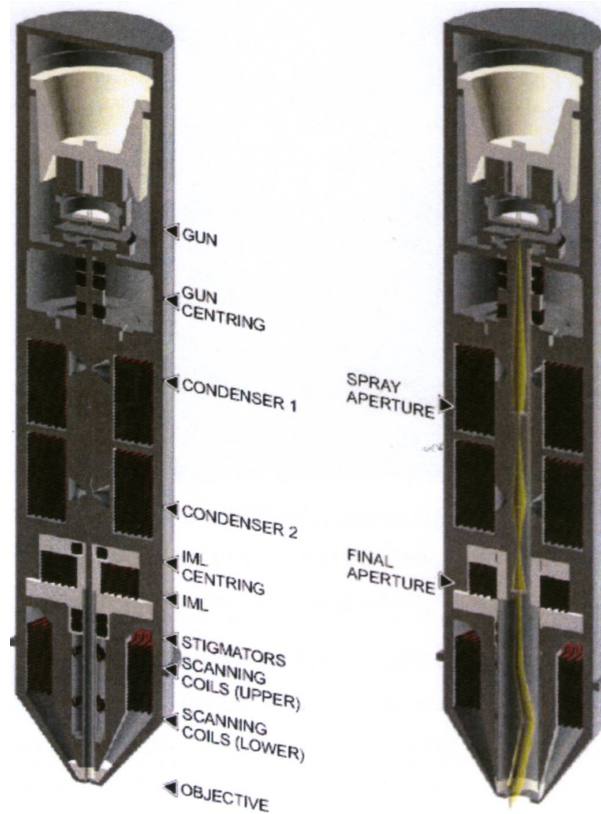
Figure 4.6: VEGA3 SEM cross section and schematic representation of the optical elements. [48]

the coils. The ramp frequency determines the scanning speed of the electron beam and the amplitude determines the microscope's field of view and the magnification.

- The *objective* is the last magnetic lens of the column and forms the resulting electron beam.

4.3.3.2   Detection System

The TESCAN VEGA3 SBH SEM is equipped with three different detectors:

- The *secondary electron (SE) detector* is of Everhart-Thornley type. In order to attract the low-energy secondary electrons arising on the sample surface and focus them onto the scintillator, a positive potential is applied to the grid on the front part of the detector. The scintillator accelerates and converts the incoming electrons into photons. These are then transferred through the light guide to the photo-multiplier outside the chamber of the microscope.

- The *backscattered electrons (BSE) detector* is of the scintillation type. It has an annular (YAG) mono-crystal with a conductive surface placed in the optical axis directly under the lower pole extension of the objective. The high energy backscattered electrons excite the scintillator atoms without any additional acceleration. Those atoms then produce visible radiation photons, which are carried to the photomultiplier.

- The *EDS detector* is a silicon drift detector (SDD), namely a Bruker XFlash 410 M detector. The SDD is a type of energy dispersive solid state detector. It utilizes a drift field structure to guide charges produced by absorbed X-rays to a small anode. Such a detector eliminates the need to be cooled by liquid nitrogen. Instead, it is only moderately cooled by thermoelectric Peltier coolers. The detector has a 10 mm^2 active area and a resolution of 133 eV at Mn K$_\alpha$ wavelength. Besides that, it has a counting rate of 100000 cps and it is able to detect every element from B to Am [49].

4.4   Electronic properties

4.4.1   DynaCool Physical Property Measurement System (PPMS)

A Physical Property Measurement System (PPMS) from Quantum Design was used in this work. This equipment offers a stable environment for measuring different properties such as the magnetic moment, resistivity, specific heat, etc. in a range of temperatures from 1.8 K to 400 K in applied magnetic fields up to 9 T. This device operates using a closed-cycle He cryostat, obviating the need to supply liquid cryogens. Both the superconducting magnet and the sample chamber are cooled by a minimum amount of liquid helium produced by the cryocooler. The helium flows up the cooling annulus, cooling the sample chamber. This flow is driven by the pressure difference between the cooling annulus (maintained at moderated vacuum) and the bucket ($\sim$ 1 atm), which controls the 4 K plate.

It is important to notice that there are two cooling flow modes in this equipment: main flow and low temperature flow. In the former, $\sim$ 4.2 K helium gas in the bucket flows up the counter-flow heat exchanger (CFE), through the mass flow controller, returns to CFE and reaches the cooling annulus.The low temperature flow mode is activated when the temperature is below $\sim$ 10 K. In this mode, 4.2 K liquid from the bucket is expanded through the capillary flow impedance. The inlet pressure is at bucket pressure, around 1 atm, and the outlet is 10 Torr (annulus pressure), what leads to

evaporation of some of the helium, resulting in an outlet flow that is a mixture of liquid and gas at 1.7 K. This mixture flows to the bottom of the cooling annulus (also know as pot). The equipment uses a heater on the impedance, another in the pot and a liquid level sensor in the cooling annulus in order to control simultaneously the level of the liquid in the pot and the flow rate of the gas and, thereafter, controlling the temperature of the sample with high accuracy. Helium finnaly goes through the circulation pump and returns to the bucket, where it will be cooled by the cryocooler and reused [50].

The magnetic field is generated by a TiNb superconducting coil. The magnet is cooled by contact with the 4 K plate (see Fig. 4.7) and its current is controlled by a hybrid digital/analog magnet controller. The PPMS has three thermometers located at different places controlling the temperature of the magnet and the cryostat. Moreover, extra thermometers can be monitored for particular applications.

The system has a built in magnetic shield, which reduces the field experienced outside, allowing other instruments to be placed nearby.

In this work it was used one of the options of the DynaCool equipment, the Electrical Transport Option (ETO), which will be described in the next section.

4.4.2   Electrical Transport Option (ETO)

ETO contains two channels, each with its dedicated electronics, allowing a simultaneous, continuous resistance measurement of two different samples. Each channel contains a precision current source and voltage preamplifiers coupled to a Digital Signal Processor (DSP). The response signal is filtered by the DSP, which filters the AC component and picks out the portion of the response at the same frequency and phase as the drive signal, while eliminating all other components of the signal [51].

This option can operate in two modes: the 2-wire mode, used for high impedance $(2\,\mathrm{M\Omega} - 5\,\mathrm{G\Omega})$, and the 4-wire mode, for low impedance $(\mu\Omega - 10\,\mathrm{M\Omega})$ (Fig. 4.8). For the 2-wire mode, an AC voltage is applied and the AC current response is measured with a current amplifier. However, the most common mode, which is also the one used in this work, is the 4-wire mode, where a sinusoidal current is applied and the AC voltage response is measured. In this mode, the current is applied via the two external contacts, and the two intern contacts measure the voltage drop across a section of the sample. Ideally, the two intern contacts draw very little current. Hence, the current through the sample and the voltage drop are known with high accuracy.

However, there are some factors that can influence the voltage readings, such as the quality of the contacts, the sample characteristics or the thermal and electrical contacts between the puck and the sample. First, we should notice that ohmic and low resistance
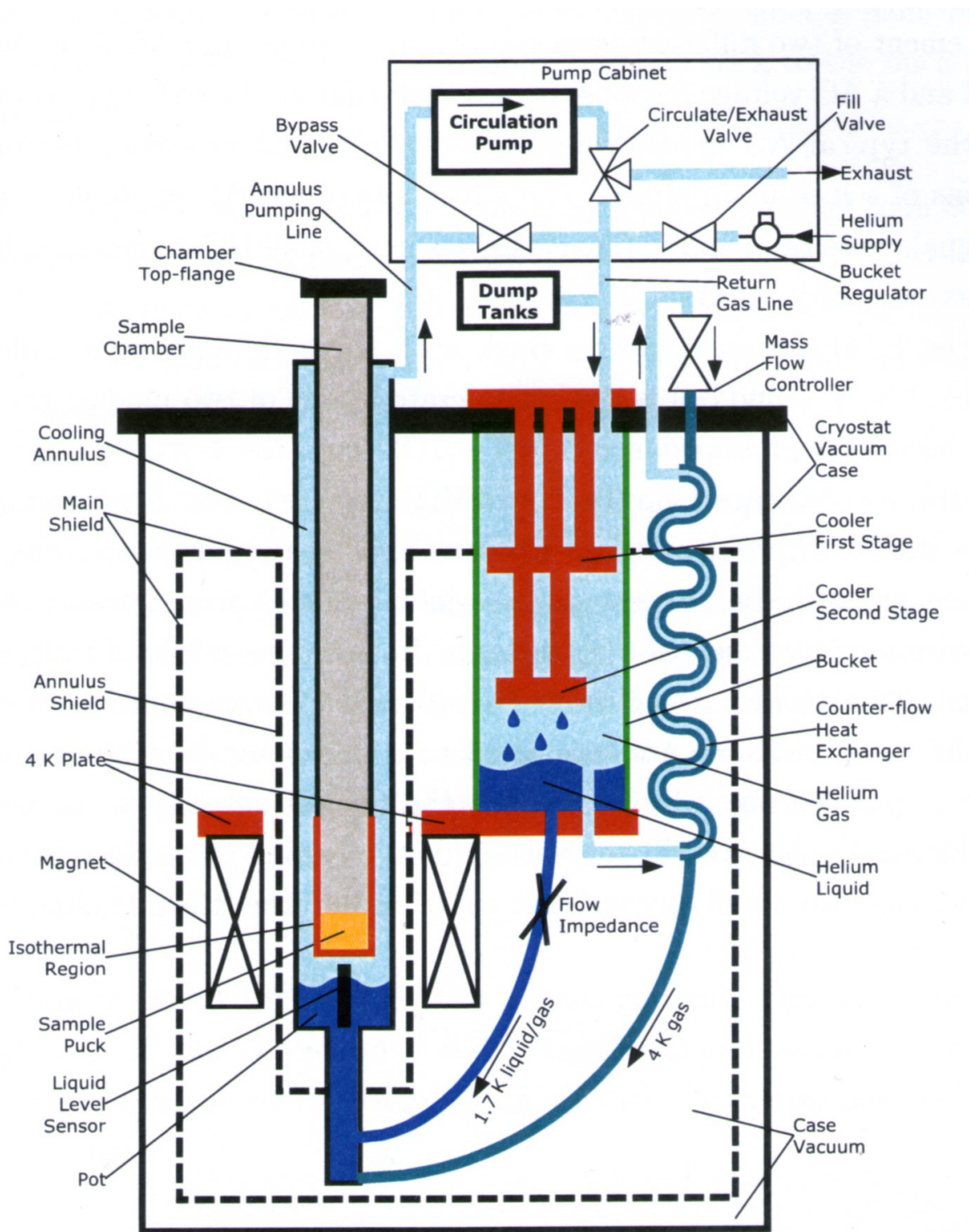
Figure 4.7: Components of the cryostat, chamber temperature and magnetic field control systems of the DynaCool Cryostat. [50]
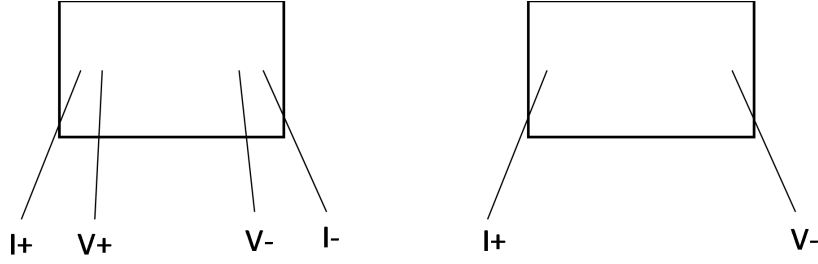
Figure 4.8: Typical placement of the contacts for a four-wire geometry (left) and two-wire geometry (right). Adapted from [51].

contacts are essential. Considering this, we usually use Ag paint to make the contacts between the Au wires and the sample. In order to assure good thermal contact between the sample and the puck and, simultaneously, electrically isolate the sample from the ground, a thin layer of cigarette paper is usually used [52]. The paper is painted on both sides with a small amount of type N grease (used for temperatures up to the room temperature), so that it sticks to the puck and the sample. Finally, it is also helpful if the sample has a regular geometry and if it is homogeneous and isotropic.

4.4.2.1   Resistance

The sample resistance can be calculated according to Ohm's law:

$$R = \frac{V}{I}, \tag{4.10}$$

where I is the current through the sample and V is the voltage drop across the sample. The resistivity of the material can then be calculated as follows

$$\rho = \frac{A}{L}R, \tag{4.11}$$

where L is the voltage lead separation and A is the cross-section area of the sample. This relation holds for a bar with an ideal geometry.

When current passes through the sample, an electric field is created. The voltage contacts should measure the voltage drop in a region where the electrical field lines are approximately linear. Thus, the voltage contacts should be placed in line with the current leads. However, experimentally, it is sometimes difficult to achieve near-perfect linearity. The measured resistance will then be affected by the transverse Hall resistance. In order to correct this effect, and taking into account that the magnetoresistivity is symmetric as a function of the applied magnetic field, we can write the longitudinal
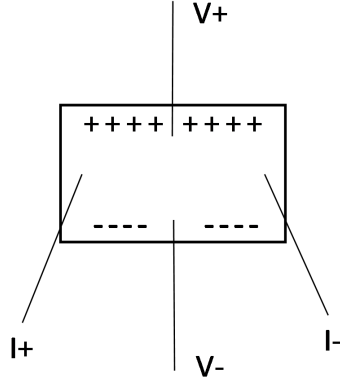
Figure 4.9: Typical lead placement on a rectangular sample for measurement of Hall potential with an applied magnetic field normal to the sample surface. Adapted from [51].

resistance, R_{xx}, as

$$R_{xx} = \frac{R^+ + R^-}{2},$$ (4.12)

where R^+ and R^- are the resistance for positive and negative magnetic fields, respectively.

4.4.2.2   Hall Coefficient

In the 4-wire mode it is also possible to measure the Hall resistance, as long as the wires are placed properly (see Fig. 4.9). When charged particles move perpendicular to a magnetic field, they experience a force perpendicular to both the field and the direction of the particle, expressed as

$$\boldsymbol{F} = q(\boldsymbol{v} \times \boldsymbol{B}).$$ (4.13)

Therefore, charged particles tend to build up on one edge of the sample, leading to a potential difference across the sample, the Hall potential, V_{H}. The separation of the charges creates a transverse electrical field, $\boldsymbol{E}_{\mathrm{H}}$, that opposes the migration of further charge.

The Hall coefficient, R_{H}, is defined as

$$R_{\mathrm{H}} = \frac{E_{\mathrm{H}}}{jB},$$ (4.14)

where j is the current density and B is the magnitude of the magnetic field. The sign of the Hall coefficient indicates the sign of the charged carriers and its magnitude is

related to the density of the carriers in the sample. When the sample geometry is well defined, the current density can be written as I/A, where I is the current and A is the cross-sectional area. Moreover, the Hall field is given by V_{H}/L, where L is the distance between the set of transverse voltage contacts. Therefore, the Hall coefficient is given by

$$R_{\mathrm{H}} = \frac{V_{\mathrm{H}}A}{IBL}. \tag{4.15}$$

On the other hand, the Hall coefficient can be shown to be

$$R_{\mathrm{H}} = \frac{1}{nq}, \tag{4.16}$$

with n representing the charge carrier density and q the charge of the carriers.

When measuring the Hall potential, the voltage contacts must be perpendicular to both the current and the field directions. Considering Fig. 4.9, the magnetic field should be applied perpendicular to the sample surface. From equations 4.10 and 4.15, one can write the Hall coefficient in terms of the measured resistance, R:

$$R_H = \frac{RA}{LB}. \tag{4.17}$$

Comparing 4.17 and 4.16, and knowing the geometry of the sample, one can then calculate the carrier density n

$$n = \frac{1}{mwq}, \tag{4.18}$$

where m is the slope, R/B, and w is the width of the sample, which relates to the cross-sectional area by $A = L \times w$.

Similarly to what happens in the magnetoresistivity measurements, the experimental Hall effect can include a component due to the longitudinal voltage drop that arises from the sample resistance itself. This would be avoided if the voltage contacts were perfectly perpendicular to the current. However, since the longitudinal resistance is usually much larger than the Hall potential, even small errors in contacts placement will be important.

In order to decrease this effect, and knowing that R_{xy} is anti-symmetric as a function of the magnetic field, we can average the measured resistances for positive and negative applied magnetic fields:

$$R_{xy} = \frac{R^{+} - R^{-}}{2}. \tag{4.19}$$

Chapter 5

Results and Discussion

In this work five bismuth chalcogenides were synthesized: Bi_2Se_3, $Bi_2Se_{3-x}Te_x$, with $x = 0.5, 0.3, 0.1$ and Bi_2Te_3. The results are reported next; the first five sections are dedicated to the characterization and morphology studies of the synthesized compounds, and each section will be dedicated to a different compound. In the last three sections we report the transport properties, namely the magnetoresistance and Hall effect of the samples under study. Since we made several synthesis for each compound, they will be identified as Batch I, II, etc. Besides, since not all synthesis were successful, only the most interesting ones will be reported here.

5.1 Bi_2Se_3

5.1.1 Batch I

5.1.1.1 Synthesis

Stoichiometric amounts of bismuth nitrate ($Bi_2(NO_3)_3 \cdot 5H_2O$), sodium selenide (Na_2SeO_3) and also potassium hydroxide (KOH) were dissolved in ethylene glycol (EG) and stirred for several minutes at room temperature, as reported by Xu et al. [37]. The mixture was then heated in the microwave oven described in the previous section. The set target temperature of $180\,°C$ was reached in 10 minutes and after that the temperature was held for 1 minute. The product was then separated by centrifugation and washed with deionized water and ethanol and dried at $50\,°C$ for 3 hours.
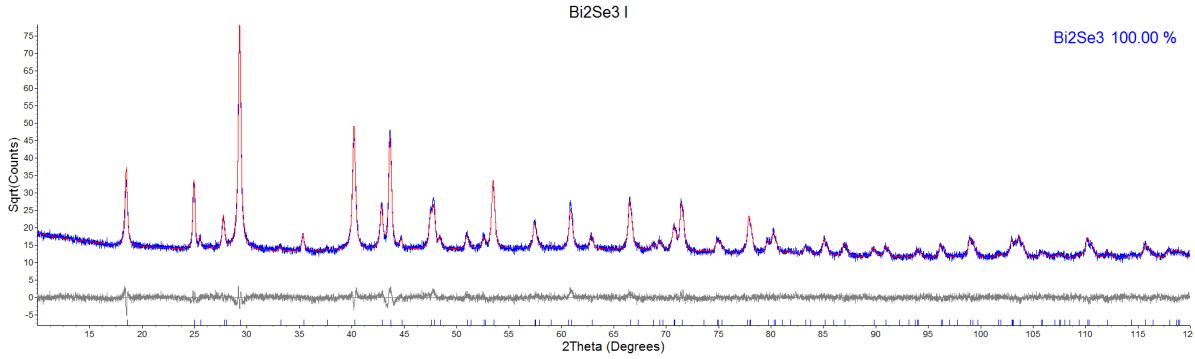
Figure 5.1: Diffraction pattern of Bi$_2$Se$_3$- Batch I.

5.1.1.2 XRD Analysis

Bruker AXS D8 AVANCE X-ray diffractometer was used to characterize the sample. The resulting powder was placed in a Si sample holder and the height of the sample was determined by scanning the primary beam, allowing to have a correct $2\theta_0$ reference. The diffractogram was obtained in the $10° - 130°$ range, with a $0.005°$ stepsize and 0.5 seconds per step. The identification of the phases was done using EVA (version 3.0) search-match option. The quantitative analysis was then determined by the Rietveld method implemented in TOPAS V5. The program allows the refinement of the microstructure parameters (grain size and microstrains), cell parameters, atomic positions, site occupancies and isotropic temperature factors. First principles calculations, which are based on the optics of the instrument, were used in order to determine the profiles for the Bragg reflections. These were convoluted with the shapes arising from the microstructure, with a lorentzian profile for the grain size distribution and a gaussian profile for the microstrain distribution.

All the diffraction peaks were successfully indexed to the rhombohedral geometry of Bi$_2$Se$_3$, suggesting the high purity of the product (see Fig 5.1). No further peaks, characteristic of impurities, were observed. The most relevant parameters from the Rietved refinement are presented in table 5.1. The cell parameters a and c agree to what is reported in the literature [37].

5.1.1.3 SEM

Scanning electron microscopy was performed using the SEM VEGA TESCAN described previously. The images presented were obtained using the SE detector and an electron beam acceleration of 5 kV. Figure 5.2 reveals the uniformity of the sample, consisting of flake-like single crystals with hexagonal form (sheets) with an average diameter of

	Bi$_2$Se$_3$ (100%)
a (Å)	4.13864(7)
c (Å)	28.6428(7)
D (nm)	65.4(5)
R_{wp} (%)	7.80

Table 5.1: Summary of the parameters from the Rietveld refinement for sample Bi$_2$Se$_3$− Batch I.

(a)

(b)

Figure 5.2: SEM images of the sample Bi$_2$Se$_3$− Batch I taken with a working distance of 10.7 mm and a magnification of (a) 10.7 k× (b) 20.0 k×.
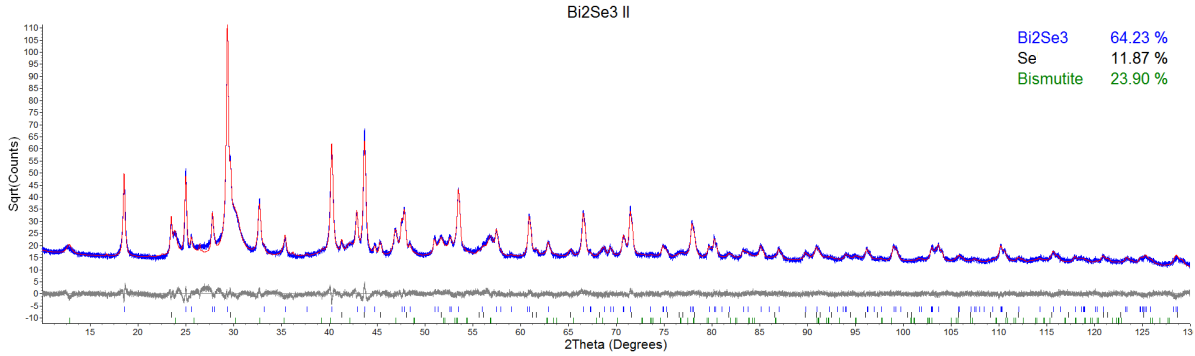
Figure 5.3: Diffraction pattern of Bi_2Se_3 - Batch II.

$\sim 2.3\,\mu$m. Note that this differs from D (table 5.1) by several orders of magnitude. The crystallite size, D, measures smaller portions of the crystal, separated by grain boundaries and, therefore, it has a lower value compared to the diameter of the particles observed by SEM.

5.1.2 Batch II

5.1.2.1 Synthesis

The synthesis was made following the previously described procedure. Since the amount of final product obtained in Batch I revealed not to be enough to prepare a pellet to measure the transport properties, the amounts of the precursors were increased in the present batch, preserving the stoichiometric ratios.

5.1.2.2 XRD Analysis

The diffractograms were obtained in the same conditions as specified before, and the identification and quantification of the samples also followed the same indications, with an exception to the bismutite phase, where the site occupancies and the temperature factors were fixed. The majority of the diffraction peaks could be indexed to Bi_2Se_3, but some other peaks, characteristic of impurities, can be observed (Fig. 5.3). We were able to identify, as impurity phases, selenium (11.9(2) %) and bismutite (23.90(13) %). The parameters from Rietveld refinement are given in table 5.2.

5.1.2.3 SEM

SEM pictures for the sample Bi_2Se_3 - Batch II were taken with an electron beam acceleration of 5 kV and a working distance of 11.80 mm. In Figure 5.4a we can observe that

	Bi$_2$Se$_3$ (64.2(2) %)	Se (11.9(2) %)	Bismutite (23.90(13) %)
a (Å)	4.13915(6)	4.36807(18)	3.8696(2)
b (Å)	—	—	3.8652(3)
c (Å)	28.6429(5)	4.9529(5)	13.784(3)
D (nm)	64.1(3)	19.0(3)$\times 10^2$	37.6(7)
R_{wp} (%)		7.68	

Table 5.2: Summary of the parameters from the Rietveld refinement for sample Bi$_2$Se$_3$ - Batch II.

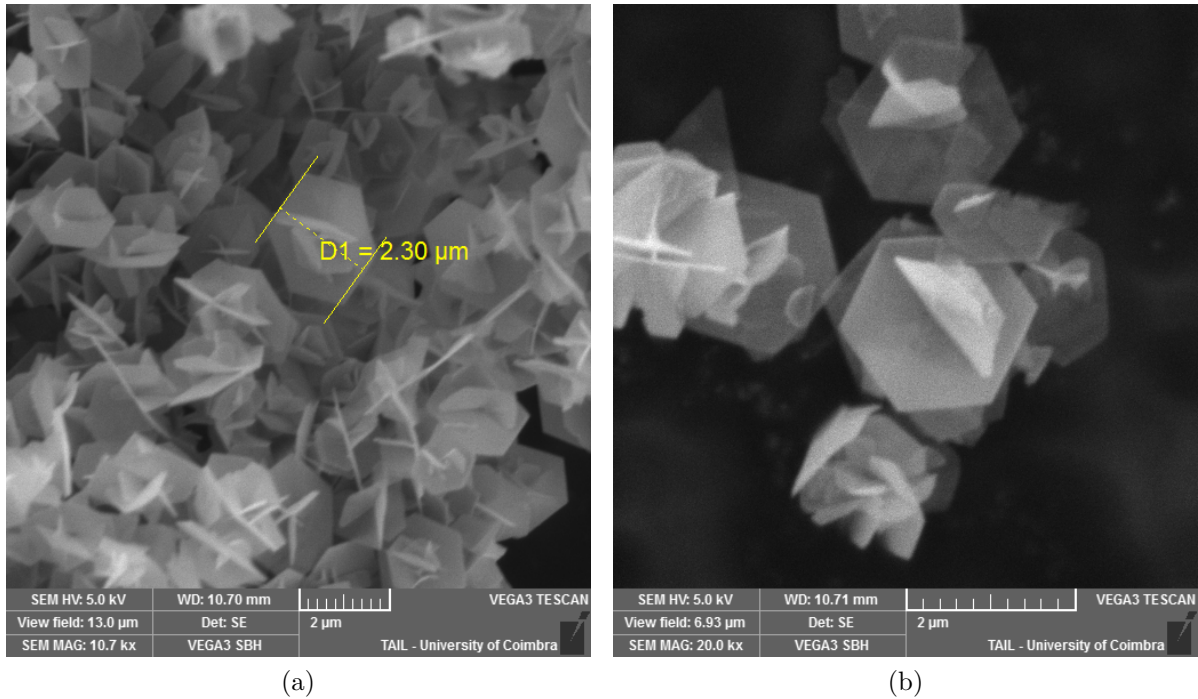Figure 5.4: SEM images of the sample Bi$_2$Se$_3$ - Batch II with a working distance of 11.80 mm and a magnification of (a) 5.00 k$\times$ (b) 7.70 k$\times$.
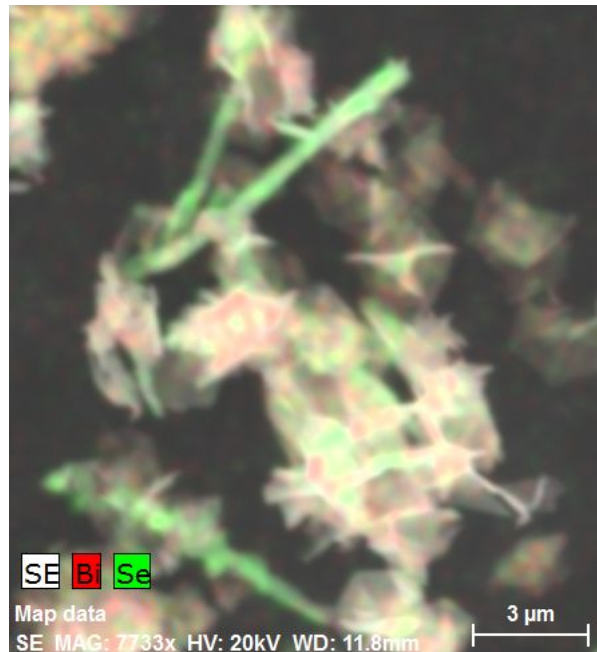
Figure 5.5: EDS mapping of the sample Bi$_2$Se$_3$ - Batch II performed with a high voltage of 20 kV and a magnification of 7.7 k×.

the structures presented are not uniform. In fact, it is possible to distinguish two differ-ent structures: one identical to what was observed in Bi$_2$Se$_3$ - Batch I - the hexagonal sheets with an average diameter of $\sim 2.3\,\mu$m; and a rod-like structure with an average length larger than to the diameter of the hexagonal structures. Further investigation was done using EDS, in order to understand possible differences in the composition of the different structures. Figure 5.5 presents the EDS analysis for the same region observed in Fig. 5.4a, using the K$_\alpha$ lines of Bi and Se. One can observe that there is a clear difference in the composition of the structures: while the hexagonal sheets have bismuth and selenium in their composition, the rod-like structures are primarily constituted by selenium. This was found to be in agreement to what was reported by Chen et al. [41], in a similar synthesis of Bi$_2$Te$_3$.

5.1.3   Batch III

5.1.3.1   Synthesis

Since the previous batch revealed some diffraction peaks that could not be indexed to the rhombohedral phase of Bi$_2$Se$_3$, its synthesis was repeated in order to avoid impurity phases. The same procedures were followed for the synthesis of Bi$_2$Se$_3$ - Batch III. The heating time was kept at 10 minutes to reach the set temperature (180 °C) plus 1 minute
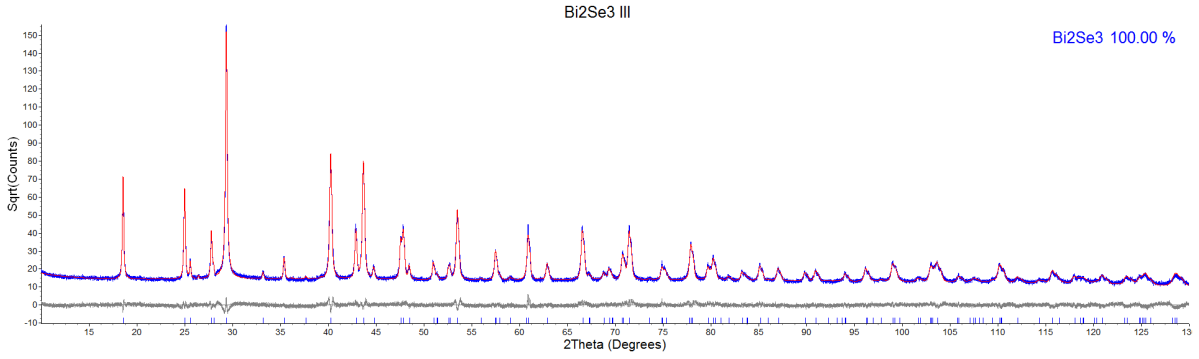
Figure 5.6: Diffraction pattern for the sample Bi$_2$Se$_3$ - Batch III.

	Bi$_2$Se$_3$ (100%)
a (Å)	4.13915(3)
c (Å)	28.6253(3)
D (nm)	145.3(8)
R_{wp} (%)	8.29

Table 5.3: Summary of the parameters from the Rietveld refinement for sample Bi$_2$Se$_3$ - Batch III.

at constant temperature.

5.1.3.2   XRD Analysis

The diffraction pattern, identification and quantification of phases followed the previously described procedures. From Fig. 5.6 we can observe the similarities with the diffraction pattern obtained for the sample Bi$_2$Se$_3$ - Batch I (Fig. 5.1). No characteristic peaks for impurities were observed. The Rietveld refinement parameters are presented in table 5.3.

5.1.3.3   SEM

The SEM images of Bi$_2$Se$_3$ - Batch III (Fig. 5.7) were obtained using an electron beam acceleration of 5.0 kV and a working distance of 11.9 mm. The images suggest an uniform sample consisting of hexagonal sheets similar to what was observed in Fig. 5.2.

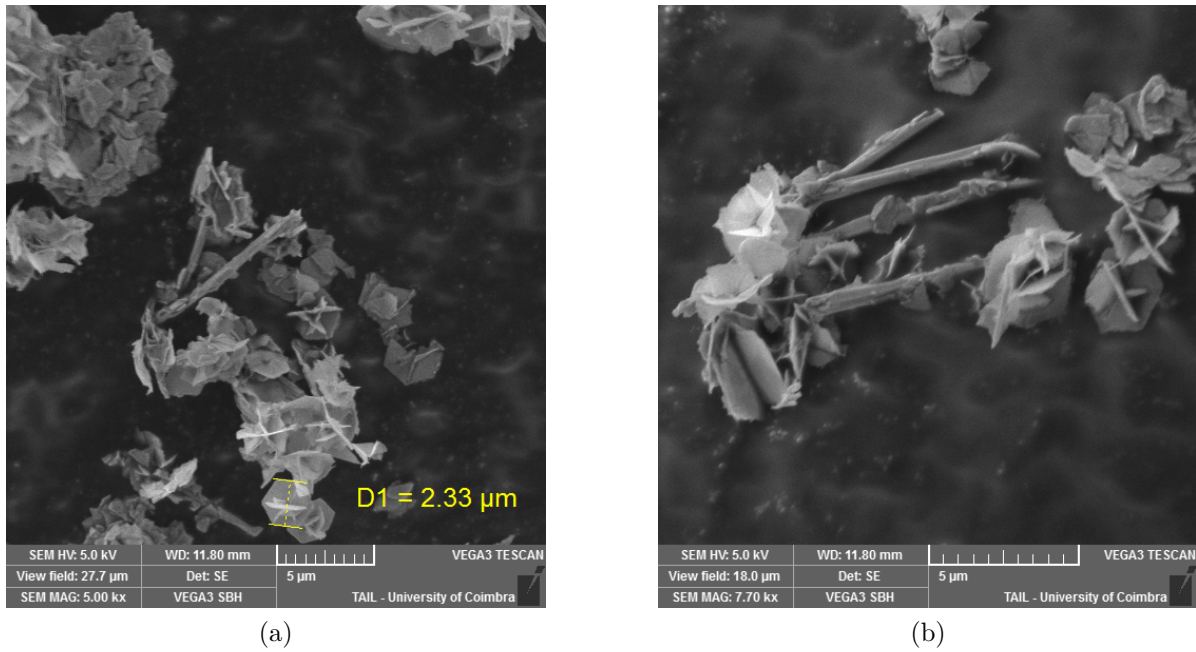(a)   (b)
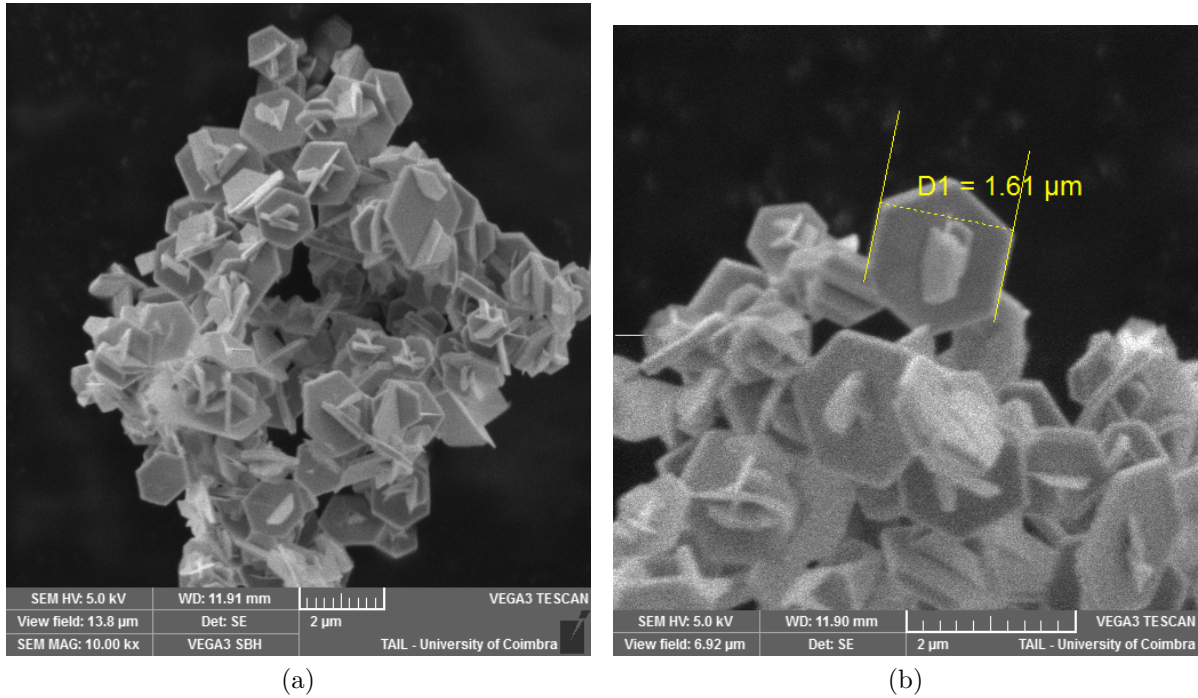
Figure 5.7: SEM images for the sample Bi_2Se_3 - Batch III performed with a working distance of 11.9 mm and a magnification of (a) 10.00 k$\times$ (b) 20.00 k$\times$.

5.2 $Bi_2Se_{2.5}Te_{0.5}$

5.2.1   Synthesis

Stoichiometric ratio of bismuth nitrate ($Bi(NO_3) \cdot 5H_2O$), sodium telluride (Na_2TeO_3), sodium selenide (Na_2SeO_3) and potassium hydroxide (KOH) were dissolved in ethylene glycol and stirred at room temperature, closely following the procedure described by Xu et al. [53]. The solution was then divided into the microwave's vessels and was subjected to a microwave cycle of 10 minutes to reach the set temperature, plus 25 minutes at 180 °C. After cooling to room temperature, the product was separated by centrifugation and washed with deionized water and ethanol several times. It was then dried at 50 °C for 3 hours.

5.2.2   XRD Analysis

The diffraction pattern, identification and quantification of phases followed the previously described procedures. Xu et al. [53] reported that all the difraction peaks were steadily indexed to Bi_2Se_3, but a slight shift to lower-angles of the peak $2\theta \sim 29.5°$ was observed due to the incorporation of tellurium, an atom of bigger dimensions, in the lat-

tice. While the majority of the diffraction peaks could be indexed to the Bi_2Se_3 phase, there was another phase with peaks next to those of Bi_2Se_3 (see Fig. 5.8). This suggested that there could be an isostructural phase, with slightly increased cell parameters. This phase would be an intermediate phase between Bi_2Se_3 and the desired $Bi_2Se_{2.5}Te_{0.5}$. In fact, while analyzing this intermediate phase and taking into account the occupancies of the elements in TOPAS, we came to the conclusion that tellurium had substituted completely the second atom of selenium in the Bi_2Se_3 structure, leading to the formation of Bi_2SeTe_2. Therefore, the final mixture was constituted not by a homogeneous phase where the tellurium substituted some of the selenium in the Bi_2Se_3 structure, but by two isostructural phases. Thus, tellurium was not homogeneously incorporated in the product, but instead it led to a segregation of phases, one without tellurium, Bi_2Se_3, and another, Bi_2SeTe_2, which incorporated all Te.

5.3 $Bi_2Se_{2.7}Te_{0.3}$

5.3.1   Synthesis

The synthesis followed what was indicated for $Bi_2Se_{2.5}Te_{0.5}$ with the correct stoichiometric ratios. The heating conditions were kept the same as well.

5.3.2   XRD Analysis

The diffraction pattern was obtained using Bruker AXS D8 AVANCE X-ray diffractometer in the $10° - 130°$ range, with a $0.005°$ stepsize and 0.5 seconds per step. EVA and TOPAS were used to identify the phases and implement a Rietveld refinement, respectively. Figure 5.9 shows many similarities to the previous diffractogram (Fig. 5.8). This suggests that the Bi_2SeTe_2 phase is still present, although the correspondent peaks are not so prominent, indicating that it has decreased. Table 5.4 shows some of the refinement parameters obtained from TOPAS.

5.4 $Bi_2Se_{2.9}Te_{0.1}$

5.4.1   Synthesis

The synthesis for $Bi_2Se_{2.5}Te_{0.1}$ followed the directions for the two previous compounds.
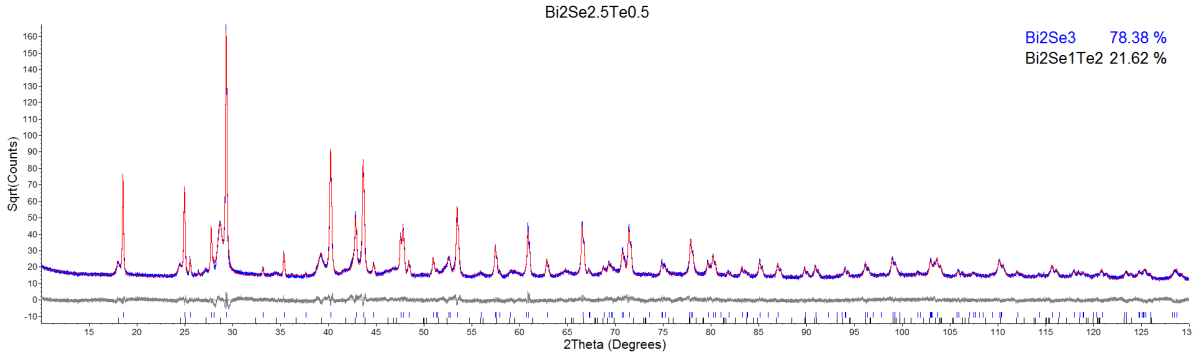
Figure 5.8: Diffraction pattern for the sample $Bi_2Se_{2.5}Te_{0.5}$.
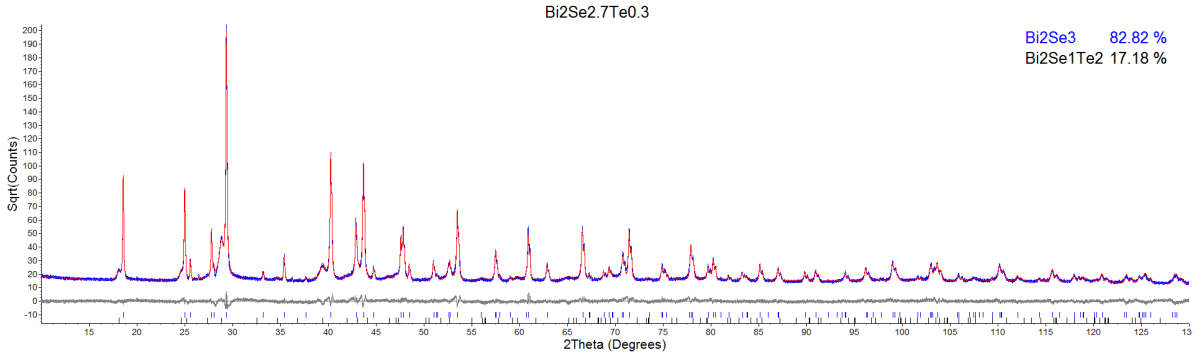
Figure 5.9: Diffraction pattern for the sample $Bi_2Se_{2.7}Te_{0.3}$.

5.4.2 XRD Analysis

The diffractogram was obtained in the conditions specified before. The Rietveld refinement was performed, including the two phases present in the samples $Bi_2Se_{2.5}Te_{0.5}$ and $Bi_2Se_{2.7}Te_{0.3}$. Since Bi_2SeTe_2 contributed with a small percentage, the parameters correspondent to this phase were kept fix. The diffraction pattern can be seen in Figure 5.10. It can be observed that Bi_2SeTe_2 has now little relevance, but it still improves the refinement.

	$Bi_2Se_{2.5}Te_{0.5}$	$Bi_2Se_{2.7}Te_{0.3}$	$Bi_2Se_{2.9}Te_{0.1}$
Bi_2Se_3	78.4(2)	82.8(2)	99.30(12)
Bi_2SeTe_2	21.6(2)	17.2(2)	0.70(12)
R_{wp} (%)	8.22	8.18	8.24

Table 5.4: Summary of the parameters from the Rietveld refinement for samples $Bi_2Se_{2.5}Te_{0.5}$, $Bi_2Se_{2.7}Te_{0.3}$ and $Bi_2Se_{2.9}Te_{0.1}$.
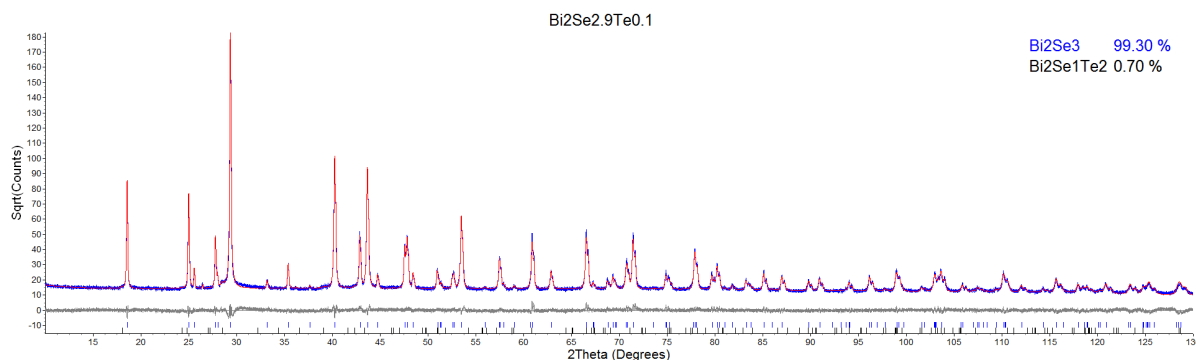
Figure 5.10: Diffraction pattern for the sample Bi$_2$Se$_{2.9}$Te$_{0.1}$.

5.5   Bi$_2$Se$_{2.5}$Te$_{0.5}$ - Repetition

5.5.1   Batch III

5.5.1.1   Synthesis

Since all three compounds from the family Bi$_2$Se$_{3-x}$Te$_x$ synthesized previously led to similar results in the XRD analysis, the synthesis was repeated. We chose to repeat, in slightly different conditions, the synthesis of Bi$_2$Se$_{2.5}$Te$_{0.5}$ since that compound had the most prominent additional phase and would be, in principle, easier to detect. Therefore, stoichiometric ratio of sodium tellurite, sodium selenide and potassium hydroxide were dissolved in ethylene glycol. Separately, a 0.5 mmol solution of bismuth nitrate in ethylene glycol was prepared. The two solutions were mixed and the final mixture was heated in the microwave in the same conditions as before. This intermediate step was done according to what was reported by Xu et al. [53], intending to make the final solution more homogeneous.

5.5.1.2   XRD Analysis

The diffraction pattern was obtained in the conditions specified before. Identification of phases was performed using EVA, and TOPAS was used to implement a Rietveld refinement. The Bragg reflections were described by a modified pseudo-voigt (PV_MOD), as the profile determined from first principles had difficulties in the description of the input. Besides the peaks indexed to Bi$_2$Se$_3$, we were able to identify some peaks characteristic of tellurium (Fig. 5.11). Moreover, we can observe the presence of other phases similar to what was reported in the section above. When we tried to implement the refinement with the phase described in the previous sections, the site occupancies pointed not to Bi$_2$SeTe$_2$ but to Bi$_2$Se$_2$Te, an isostructural phase where the atom of selenium in the

	$Bi_2Se_{2.5}Te_{0.5}$- III
Bi_2Se_3 (%)	49.1(6)
Te (%)	0.63(4)
$Bi_2SeSe_xTe_{2-x}$ (%)	41.2(6)
Bi_2Se_2Te (%)	9.0(3)
R_{wp} (%)	5.29

Table 5.5: Summary of the parameters from the Rietveld refinement for sample $Bi_2Se_{2.5}Te_{0.5}$ - Batch III.

second position is only half substituted. This, however, led to a poor description of the broadening of the peaks correspondent to Bi_2Se_3. We identified the presence of two phases with different Te content, Bi_2Se_2Te and $Bi_2SeSe_xTe_{2-x}$. The former would be responsible for the appearance of peaks next to those of Bi_2Se_3 and the latter would describe the broadening of the principal peaks. The cell parameters, site occupancies and isotropic temperature factors were kept fix for the Bi_2Se_2Te phase, as this was the only option we encountered in order to have a good Rietveld refinement. For $Bi_2SeSe_xTe_{2-x}$, the site occupancies indicated the compound $Bi_2Se_{2.68}Te_{0.32}$. A summary of the Rietveld refinement parameters, with the percentages for each phase, is included in table 5.5.

5.5.2   Batch V

5.5.2.1   Synthesis

Since in the previous batch we were still unable to eliminate the undesired phases, another change was made. In the synthesis of $Bi_2Se_{2.5}Te_{0.5}$ - Batch V we tried to avoid any possible heterogeneity in the solution. As the solution was divided into the vessels it was possible that the distribution of the precursors in the different vessels was not uniform, causing the reaction to process differently in the different vessels. In order to overcome this, we made three separated solutions (listed bellow as #1, #2, #3), one for each vessel, in which stoichiometric ratios of sodium tellurite, sodium selenide and potassium hydroxide were dissolved in ethylene glycol. Separately, a 0.5 mmol solution of bismuth nitrate in ethylene glycol was prepared and then mixed with the first. The mixture was then microwave-heated in the conditions specified before.
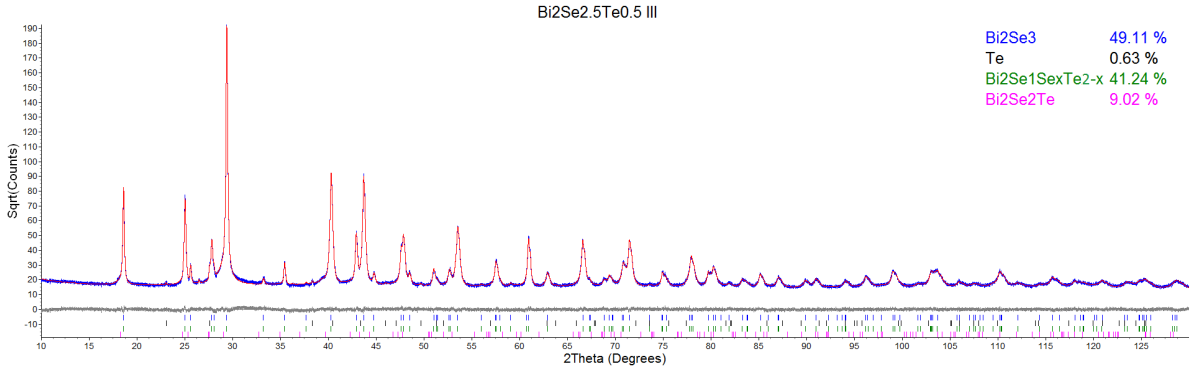
Figure 5.11: Diffraction pattern for the sample Bi$_2$Se$_{2.5}$Te$_{0.5}$ - Batch III.

	Sample #1	Sample #2	Sample #3
Bi$_2$Se$_3$ (%)	41.9(9)	46.9(9)	47.6(1)
Te (%)	4.14(11)	2.34(18)	0.24(4)
Bi$_2$SeSe$_x$Te$_{2\text{-}x}$ (%)	38.2(1)	41.3(1)	39.4(1)
Bi$_2$Se$_2$Te (%)	15.8(5)	9.7(4)	12.7(7)
R_{wp} (%)	5.29	5.77	5.46

Table 5.6: Summary of the parameters from the Rietveld refinement for sample Bi$_2$Se$_{2.5}$Te$_{0.5}$ - Batch V, samples #1, #2, #3.

5.5.2.2 XRD Analysis

The diffraction pattern, identification and quantification of the phases was performed in the conditions mentioned earlier, with a modified pseudo-voigt describing the peak type. As can be seen in Figures 5.12 to 5.14, the diffraction pattern suggests the presence of Bi$_2$Se$_3$ and Te. Moreover, the same intermediate phases indicated earlier are present. The cell parameters, site occupancies and isotropic temperature factors were kept fix for Bi$_2$Se$_2$Te. The site occupancies for Bi$_2$SeSe$_x$Te$_{2-x}$ indicated the presence of Bi$_2$Se$_{2.5}$Te$_{0.5}$ (sample #1), Bi$_2$Se$_{2.32}$Te$_{0.68}$ (sample #2) and Bi$_2$Se$_{2.24}$Te$_{0.76}$ (sample #3). These two phases (Bi$_2$Se$_2$Te and Bi$_2$SeSe$_x$Te$_{2-x}$) and Te phase incorporated again all the tellurium, leading to a non-homogeneous distribution of this element. Also, it is relevant to notice that the three initial solutions, although very similar in composition, led to significant differences in the quantitative composition of the phases. A summary of the refined parameters is present in table 5.6 (sample #1 to #3). Note that, while the parameter a is approximately constant in the three samples, c increases from sample #1 to sample #3 ($c = 28.6063(11)$ Å in sample #1 to $c = 28.6255(10)$ Å in sample #3), in agreement to the incorporation of more Te in Bi$_2$SeSe$_x$Te$_{2-x}$ structure.
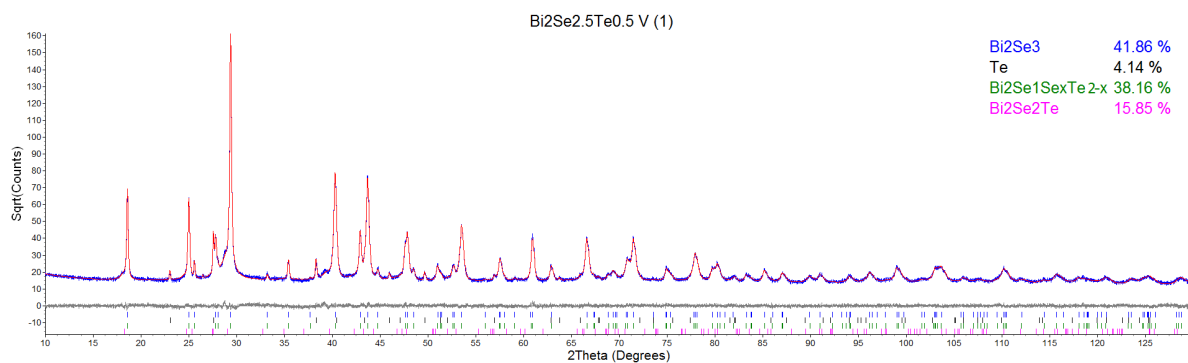
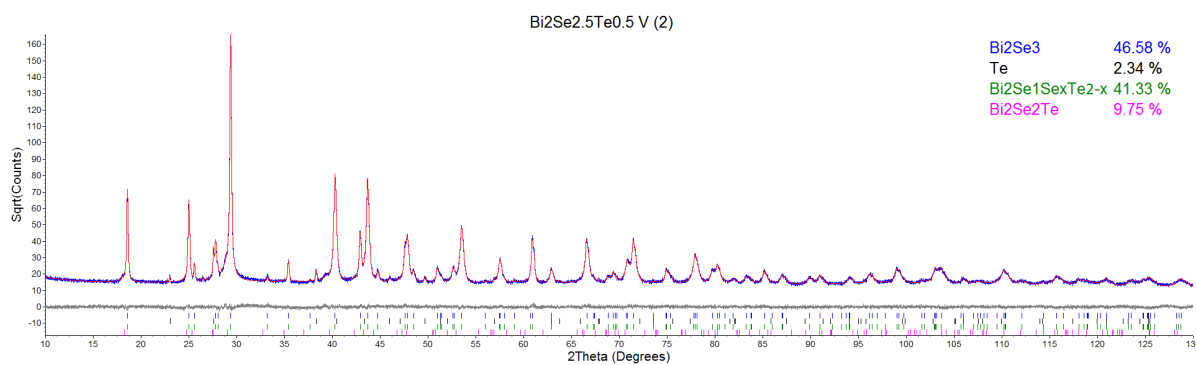Figure 5.12: Diffraction pattern for the sample $Bi_2Se_{2.5}Te_{0.5}$ - Batch V #1.

Figure 5.13: Diffraction pattern for the sample $Bi_2Se_{2.5}Te_{0.5}$ - Batch V #2.

Figure 5.14: Diffraction pattern for the sample $Bi_2Se_{2.5}Te_{0.5}$ - Batch V #3.

5.6 Bi$_2$Te$_3$

5.6.1 Batch IV

5.6.1.1 Synthesis

Following a similar procedure to what was done in the synthesis of Bi$_2$Se$_3$, stoichiometric ratio of bismuth nitrate (Bi(NO$_3$)$_3 \cdot$5H$_2$O), sodium tellurite (Na$_2$TeO$_3$) and potassium hydroxide (KOH) were dissolved in ethylene glycol and stirred for several minutes at room temperature. The mixture was placed in several vessels in the microwave. The heating was processed in a 10 min ramp to reach the set temperature of 180 °C and 12 min in that constant temperature. The increased time in relation to what was done with Bi$_2$Se$_3$ is due to the higher reduction potential of the tellurium (Te + 2e$-$ = Te^{2-}, E^0 = -1.143 V; Se + 2e$-$ = Se^{2-}, E^0 = -0.924 V), as explained by Zhou et al. [42]. Since it was suggested that a much longer time is needed to produce Bi$_2$Te$_3$ than Bi$_2$Se$_3$ under similar conditions, increasing the time from 0.5 hours in Bi$_2$Se$_3$ to 6 hours in Bi$_2$Te$_3$ [42], we tried to increase the heating time by 12 times of that of Bi$_2$Se$_3$, leading to a heating time of 12 minutes. However, when the mixture was cooled to room temperature, it was notorious that while some of the vessels had product (a dark precipitate was formed in the bottom of the vessels), there was one with a light-yellow liquid without any precipitate. Regarding this, the product resultant from each vessel was not mixed, leading to two different samples, named #1, #2, depending on the position of the vessels in the microwave. These results were also found in the batches I-III, not described here due to the similarity of the results.

5.6.1.2 XRD Analysis

The diffraction pattern was obtained in the same conditions as before. Identification of the phases was performed using EVA and their quantification using TOPAS. The profile for the Bragg reflections was determined from first principles. It can be observed in Figures 5.15 and 5.16 that the phases are the same, although their quantities vary. Note that the expected product, Bi$_2$Te$_3$, was actually the smallest phase present on both samples. Phases correspondent to Te and TeO$_2$ were also identified. There are also other phases of smaller relevance, identified by a star in the same figures, that we were unable to identify. A summary of the Rietveld refinement parameter is presented in table 5.7.

Figure 5.15: Diffraction pattern for the sample Bi_2Te_3 - Batch IV #1.
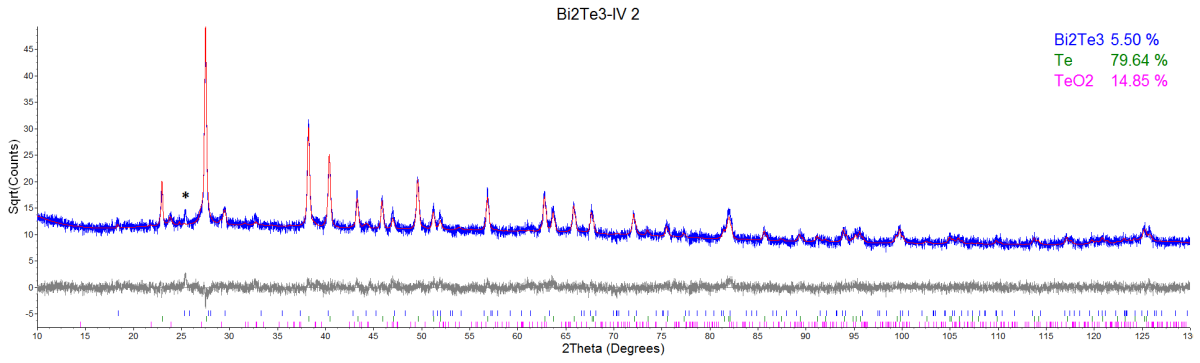
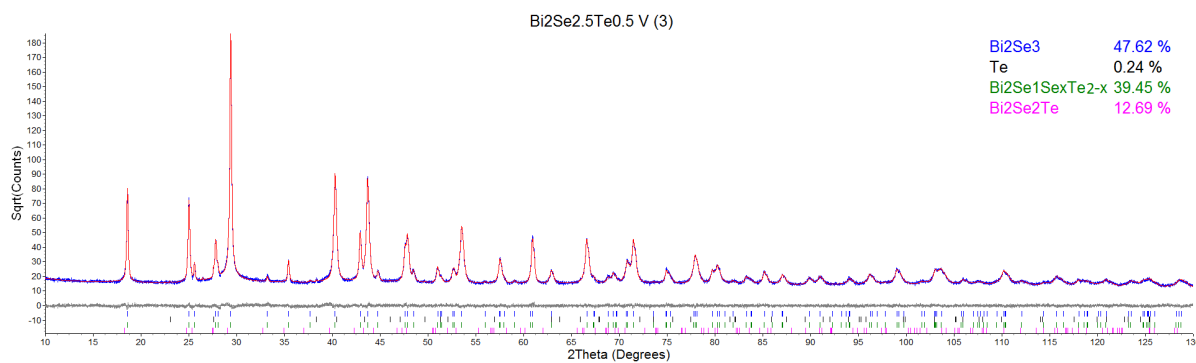Figure 5.16: Diffraction pattern for the sample Bi_2Te_3 - Batch IV #2.

	Sample #1	Sample #2
Bi_2Te_3 (%)	11.76(19)	5.5(5)
Te (%)	42.0(4)	76.6(11)
TeO_2 (%)	46.3(5)	14.9(11)
R_{wp} (%)	9.44	10.33

Table 5.7: Summary of the parameters from the Rietveld refinement for sample Bi_2Te_3 - Batch IV.
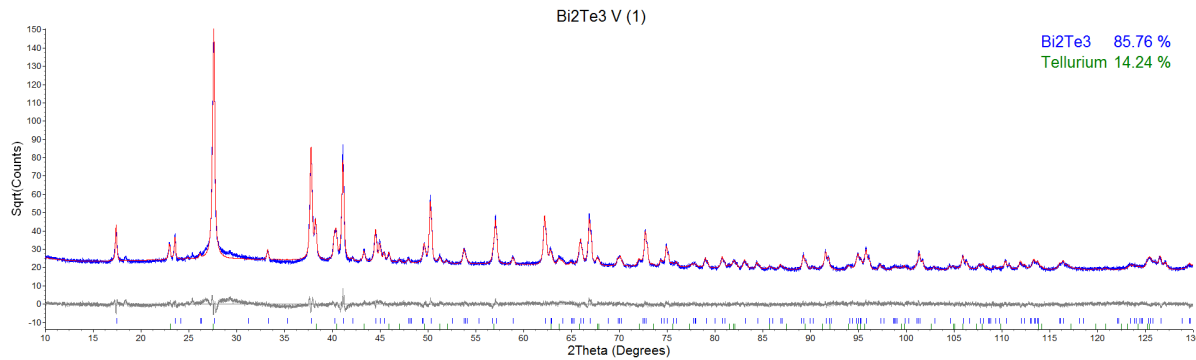
Figure 5.17: Diffraction pattern for the sample Bi$_2$Te$_3$ - Batch V #1.

5.6.2 Batch V

5.6.2.1 Synthesis

The previous results suggested that the solution could be heterogeneous, leading to an uneven distribution of the precursors in the solvent. To avoid this, three different solutions were made, one for each vessel, named #1, #2 and #3. Furthermore, the mixture was microwave-heated for 10 min in order to reach the set temperature of 180 °C plus 30 min at constant temperature. The heating time of the present batch was chosen regarding the results reported by Chen et al. [41], in which they state that 30 min is the optimum reaction time for their system (similar to the one reported here), leading to the formation of pure Bi$_2$Te$_3$. When cooled to room temperature, all the vessels had a dark precipitate in the bottom, suggesting that non-homogeneity could, in fact, have been a problem in the previous synthesis.

5.6.2.2 XRD Analysis

The samples #1, #2 and #3 were examined by X-ray diffraction. Identification and quantification of the phases present in the diffraction peaks was implemented using EVA and TOPAS, respectively. The diffractograms are presented in Figures 5.17 to 5.19. The composition of the three samples determined from Rietveld refinement is given in table 5.8. The three samples have common phases, although their contents vary from sample to sample. We can observe that, even though the solution was, in principle, homogeneous, there is a difference in the quantities of the specified phases. Keeping in mind the formation mechanism explained in section 4.1, one can deduce that the formation of Bi$_2$Te$_3$ at the expense of Te occurred with decreased success from samples #1 to #3. This could be due to possible hot spots in the microwave cavity, leading to an uneven heating process of the different vessels.
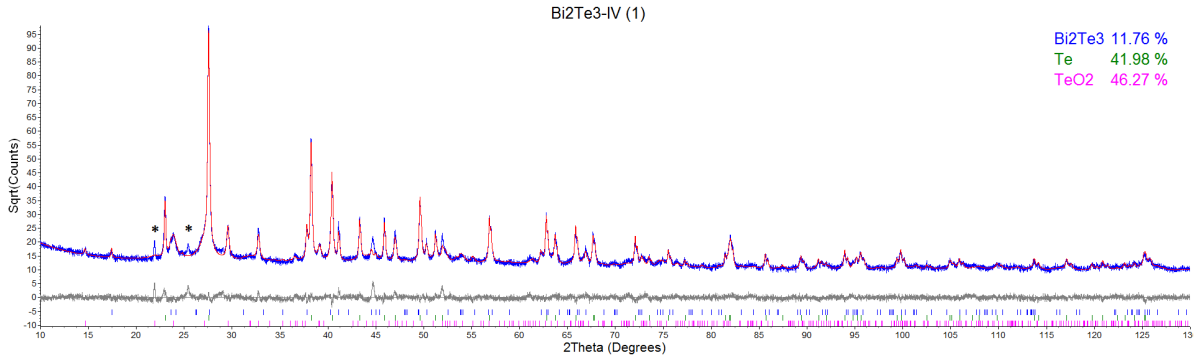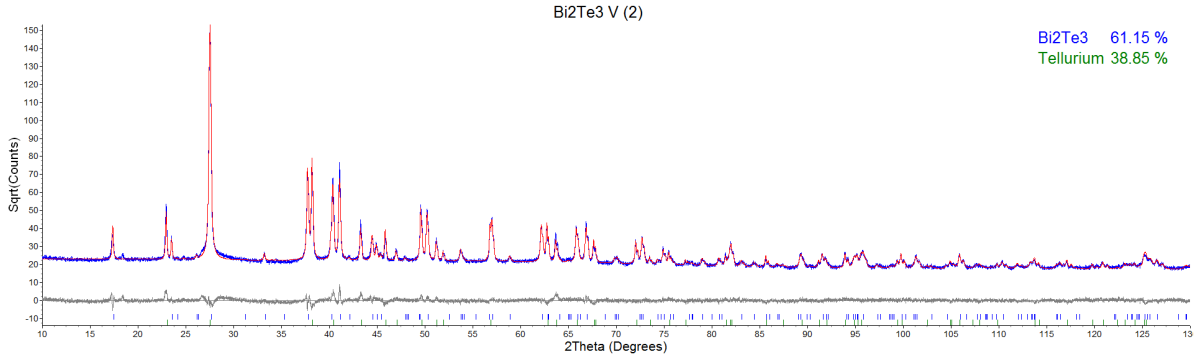
Figure 5.18: Diffraction pattern for the sample Bi_2Te_3 - Batch V #2.
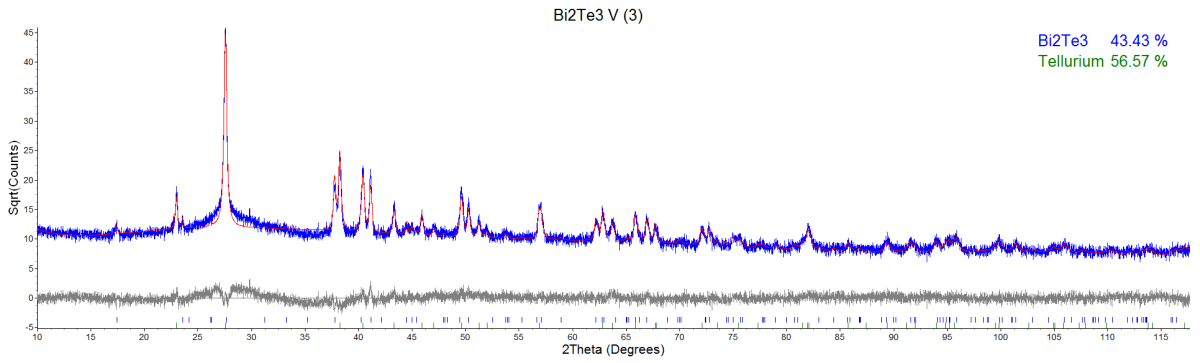
Figure 5.19: Diffraction pattern for the sample Bi_2Te_3 - Batch V #3.

	Sample #1	Sample #2	Sample #3
Bi_2Te_3 (%)	85.76(15)	61.1(3)	43.4(9)
Te (%)	14.24(15)	38.9(3)	56.6(9)
R_{wp} (%)	6.79	7.17	11.67

Table 5.8: Summary of the parameters from the Rietveld refinement for sample Bi_2Te_3 - Batch V.

Figure 5.20: Puck containing Bi$_2$Se$_3$ $-$ II, with the 4-point contacts used to measure the longitudinal resistance.

5.7 Transport properties of Bi$_2$Se$_3$ - Batch II

The powder resultant from the synthesis was pressed into a pellet by applying a pressure of 6 MPa at room temperature, and four contacts were placed in the sample, in agreement to the 4-probe measurement technique (Fig. 4.9), as can be seen in Fig. 5.20. The contacts consist of golden wires connected both to the sample and the puck by conductive silver paint. The DynaCool Physical Property Measurement System (PPMS) was used to perform all the measurements reported in the next sections.

5.7.1 Resistance vs Temperature

The temperature dependence of the longitudinal resistance for sample Bi$_2$Se$_3$ - II is illustrated in Figure 5.21. It shows a metallic behavior ($dR/dT > 0$) for a certain temperature range, compatible with a finite bulk population or with an impurity band with high conduction [23]. In the former case, SdH oscillations originated from the 3D bulk states have been reported. Furthermore, Butch et al. [54] reported the temperature dependence for several carrier concentrations in Bi$_2$Se$_3$ (Fig. 5.22). For $n > 10^{18}\,\mathrm{cm^{-3}}$, a metallic behavior is expected, while for lower concentrations, a minimum develops at around 30 K. This same anomalous behavior is observed in the present sample.

For higher temperatures, it can be observed a local maximum at ~ 200 K, representing a crossover to an activated behavior, while the concentration of extrinsic carriers decreases [54].

5.7.2 Hall Effect

In order to study the Hall effect, the contacts were now placed in the sample according to Fig. 4.9. As discussed in section 4.4.2.2, the measured Hall effect (Figure 5.23) can
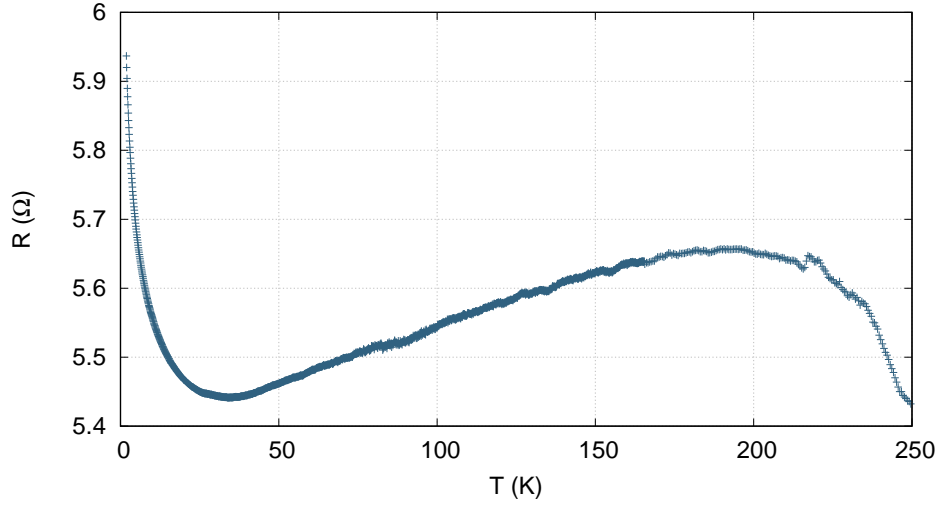
Figure 5.21: Temperature dependence of the resistance for the sample Bi$_2$Se$_3$ - Batch II. There are anomalies observed above 250 K which are not intrinsic to the sample but are due to problems in the electrical contacts, since those results were not reproducible.

include a component due to the longitudinal voltage drop, which is actually visible at low temperatures, since one can observe the WAL dip[1] around $B \sim 0$ T. In order to eliminate this, we can average the measurements for positive and negative fields following equation 4.19.

Taking into account the lead placement illustrated in figure 5.20, the positive slope identified in figure 5.24 indicates carriers with negative charge, i.e., electrons. This result agrees with the expected, since Bi$_2$Se$_3$ is naturally n-type due to Se vacancies.

Furthermore, the carrier density, $n_{\rm H}$, can be calculated from eq. 4.18, knowing the width of the sample, $w = (0.20 \pm 0.05)$ mm. The fitting illustrated in figure 5.24 was performed at 1.8 K and yields $m = (17674 \pm 6) \times 10^{-6}\,\Omega{\rm T}^{-1}$. One can then calculate the carrier density, $n_{\rm H} = 1.76 \times 10^{18}\,{\rm cm}^{-3}$. This is larger than what is usually reported for the Hall carrier density for similar topological insulators (tipically $n_{\rm H} \sim 10^{16}\,{\rm cm}^{-3}$) [55, 56].

The Hall resistivity can be interpreted in a two-band model, where conduction from both the surface and bulk states are considered. Such a situation would lead to a Hall resistivity described as

$$\rho_{xy} = \frac{(R_s\rho_b^2 + R_b\rho_s^2)B + R_sR_b(R_s + R_b)B^3}{(\rho_s + \rho_b)^2 + (R_s + R_b)^2B^2},\tag{5.1}$$

with R_b and ρ_b the Hall coefficient and resistivity of the bulk, and $R_s = w/(en_{2D})$

---

[1]In fact, the WAL feature shows in R_{xy} as a peak.
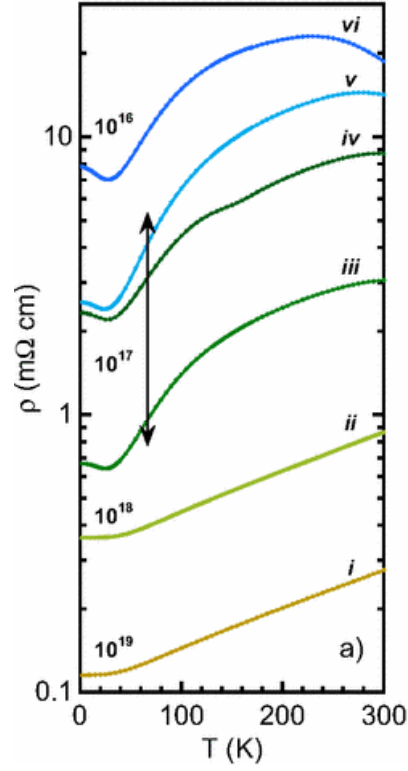
Figure 5.22: Temperature dependent electrical resistivity $\rho(T)$ between samples of Bi$_2$Se$_3$ with different carrier densities $n\,(\mathrm{cm}^{-3})$: (i) 1×10^{19}, (ii) 5.3×10^{18}, (iii) 4.9×10^{17}, (iv) 3.7×10^{17}, (v) 3.3×10^{17}, and (vi) $\sim 10^{16}$. For high carrier densities a metallic behavior is observed, while for $n < 10^{18}\,\mathrm{cm}^{-3}$ an anomalous behavior is detected, with a minimum developing ~ 30K. [54]
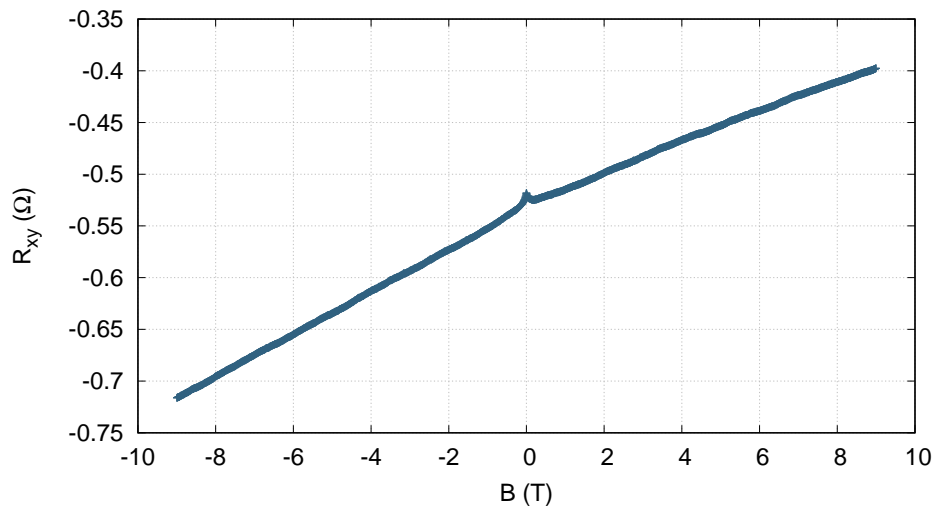
Figure 5.23: Hall effect for the sample Bi$_2$Se$_3$ $-$ II at 1.8 K.
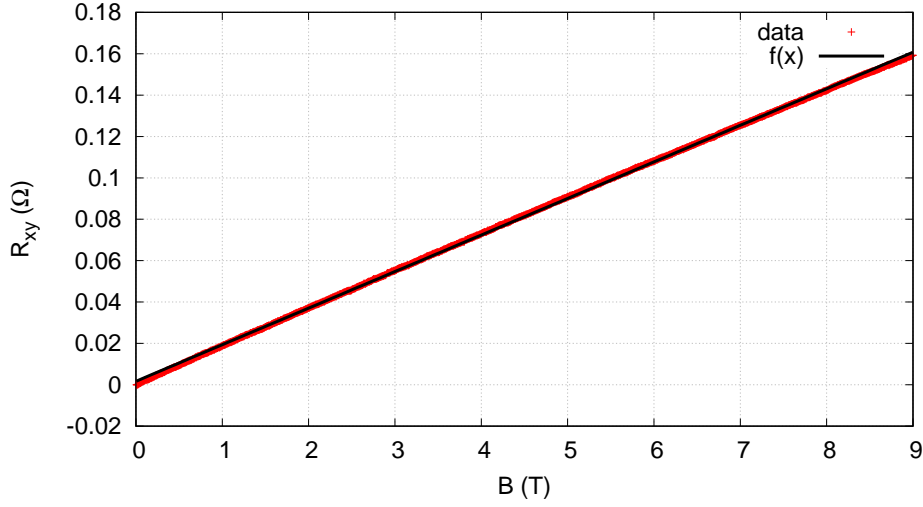
Figure 5.24: Linear fitting and anti-symmetrization of the data in Fig. 5.23 .

and $\rho_s = \rho_{surf} w$, with ρ_{surf} the surface sheet resistance. This would allow to obtain n_{2D}, n_{3D}, ρ_b and ρ_{surf}, which leads to a complicated optimization. Nevertheless, if SdH oscillations are observed in the surface, one can fix n_{2D}, which turns this analysis more reliable. The case in study, however, did not give this constraint (see discussion in 5.7.3.2). Furthermore, the obtained Hall effect is almost linear (Fig. 5.24), and the fit would be too difficult. Thus, the calculated carrier density, n_{H}, was obtained through a one-band model.

5.7.3   Magnetoresistivity

5.7.3.1   Weak anti-localization

As described by several authors, weak anti localization is a characteristic of the topological insulators, including Bi_2Se_3. The WAL effect decreases the resistivity due to the anti localization of the electrons. However, this effect is suppressed by applying a magnetic field (see section 3.1.3). When a magnetic field is applied, the weak anti localization will decrease, leading to an increase in the resistivity. Following eq. 4.12, it is necessary to average the value of the measured resistance for symmetric magnetic fields, in order to eliminate the non-linearity of the contacts. Furthermore, it is necessary to calculate the conductance, G. The resistivity ρ and the conductivity σ tensors are related by

$$\begin{pmatrix} \sigma_{xx} & \sigma_{xy} \\ \sigma_{yx} & \sigma_{xx} \end{pmatrix} = \frac{1}{\rho_{xx}^2 + \rho_{xy}^2} \begin{pmatrix} \rho_{xx} & -\rho_{xy} \\ \rho_{yx} & \rho_{xx} \end{pmatrix}. \tag{5.2}$$

Since, in the conditions of the measurements (low temperatures and low applied magnetic fields), $\rho_{xx} \gg \rho_{xy}$, one can write $\sigma_{xx} \approx \frac{1}{\rho_{xx}}$. One can then write the conductance as $R_{xx} = \frac{1}{G_{xx}}$, where G_{xx} is usually represented by G. Furthermore, we are interested in the measurement of the change of the conductance with respect to its value without a magnetic field (when the WAL effect is maximum). Thus, we choose to study the change in conductance, ΔG, due to an applied magnetic field:

$$\Delta G = G(B) - G(0) = \frac{1}{R(B)} - \frac{1}{R(0)}. \tag{5.3}$$

On the other hand, the conductivity given by the HLN formula 3.7 and the conductance are related by $\Delta\sigma = \frac{L}{W}\Delta G$, where L is the distance between the two voltage contacts ($L = 0.20(5)$mm) and W is the width of the conducting channel ($W = 3.10(5)$mm). Therefore, we can fit the previous equation to the experimental data. This was performed using a program written in Python (Appendix A). The magnetoresistance in Figure 5.25, at 1.8 K, contains a sharp dip around the zero magnetic field and a background. Although the effect for small fields tends to disappear with the increase in temperature, the background remains roughly the same. This suggests that the first has a quantum origin, while the origin of the latter appears to be classical. However, the magnetic dependence for high fields is not parabolic. Several authors reported that the dependence on the magnetic field would be intermediate between the linear and parabolic behavior [34, 57]. Furthermore, Takagaki et al. [34] report that the background dependence on the field can be described by a power-law. Therefore, the fit includes not only the HLN formula but also a power-law describing the background, given by $a \times B^b$, where a and b are fitting parameters.

For the sample in study, Bi$_2$Se$_3$ - Batch II, the fitting is presented in figure 5.26a (at 1.8 K) with entire range of magnetic field (up to 9 T) and the fitted parameters are given in table 5.9, for temperatures 1.8 K, 5 K and 15 K.

As expected, b has an intermediate value between 1 and 2, and it does not vary much with the increasing temperature. Furthermore, α should be -0.5 for each transport channel (see Chapter 3, section 3.1.3). Since $w \gg l_\phi$, one should not expect to find a diffusive channel connecting the top and bottom channels and, therefore, α should be -1. However, we found $\alpha = -4.74 \pm 0.02$ at 1.8 K, which has the same order of magnitude. Taking into account the significant errors in the measurements of L and W and the fact that we are dealing with a thin polycrystalline sample and not a true 2D system, as is the case of measurements performed on flake-like single-crystals, one can understand
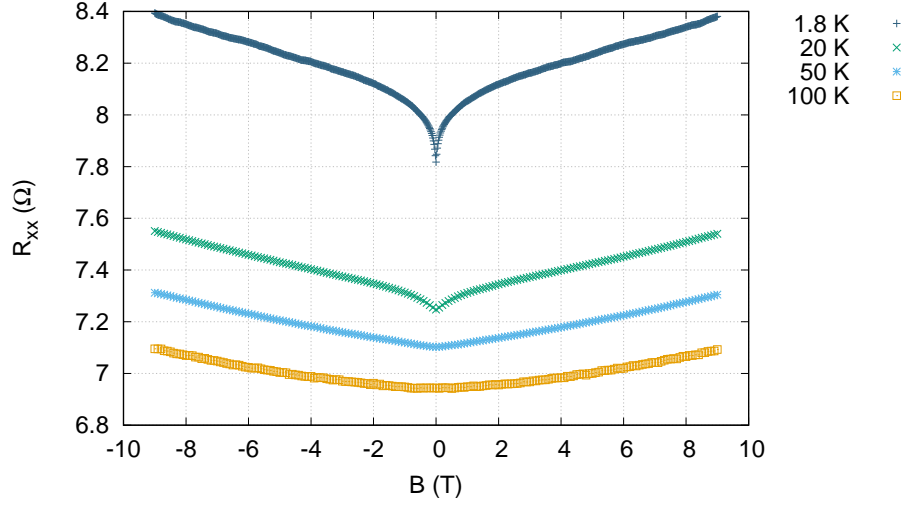
Figure 5.25: Magnetoresistance for the sample Bi_2Se_3-Batch II at different temperatures. Note that the quantum mechanical effect around 0 T disappears with the increasing temperature.

T (K)	1.8	5.0	15.0
α	-4.74 ± 0.02	-3.84 ± 0.01	-3.49 ± 0.01
l_ϕ (nm)	202 ± 1	149.0 ± 0.6	82.94 ± 0.16
b	1.86 ± 0.01	1.34 ± 0.04	1.44 ± 0.02

Table 5.9: Fitted parameters for the HLN model (α and l_ϕ) and the power-law background (b) for the sample $Bi_2Se_3 - $ II for temperatures 1.8 K, 5 K and 15 K. The fitting was performed in the entire field range (9 T).
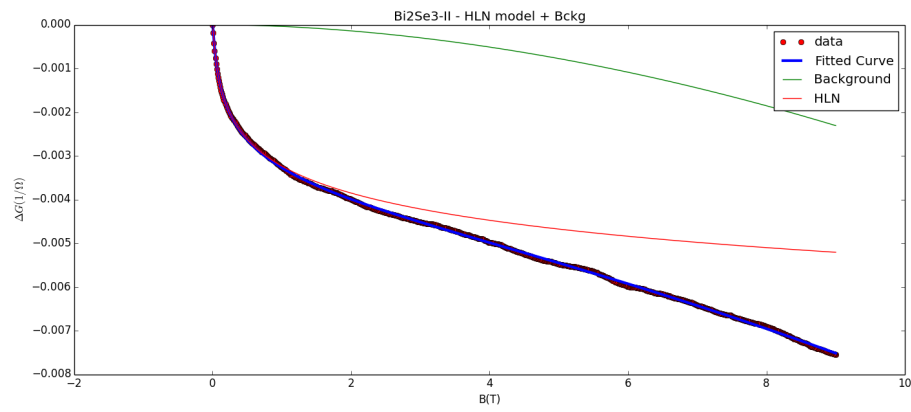
(a)
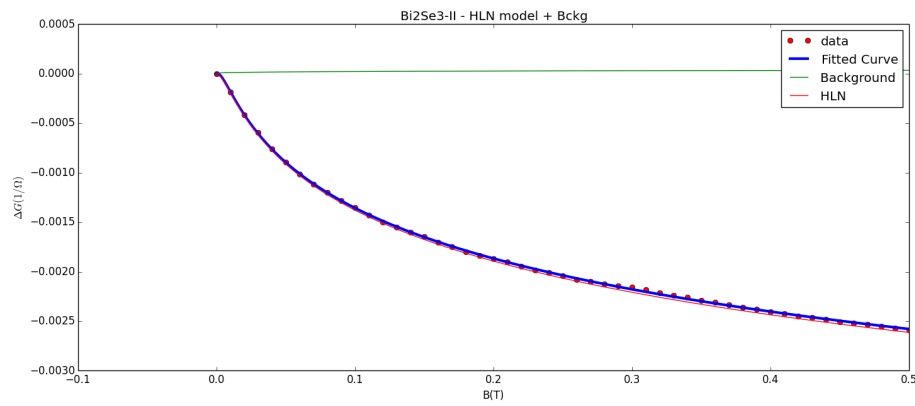
(b)

Figure 5.26: Fitting of the HLN model + background for Bi$_2$Se$_3$− Batch II at 1.8 K for fields up to (a) 9 T and (b) 0.5 T. In the latter, the background has reduced significance.
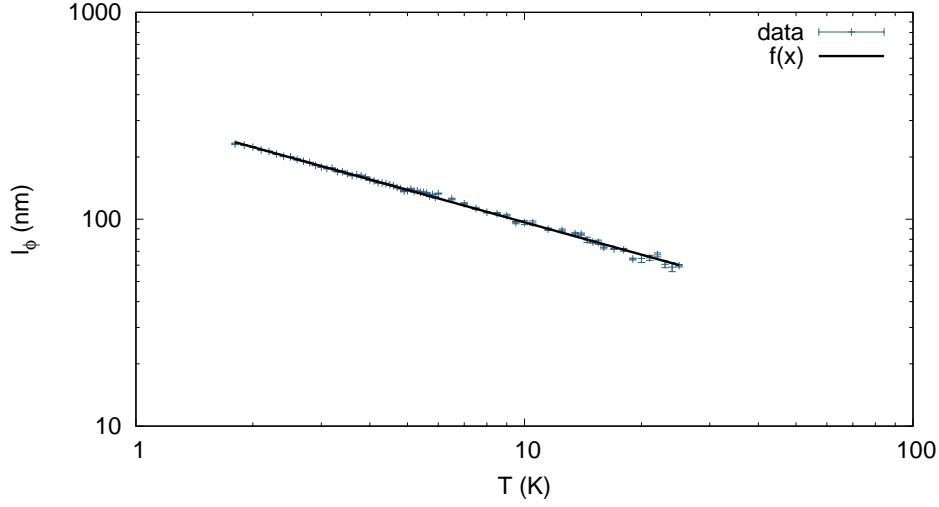
Figure 5.27: Power-law fit of coherence length, l_ϕ, with temperature for the sample Bi$_2$Se$_3$ - Batch II. The fit yields $T^{-0.519(3)}$.

why the experimental value deviates from the expected value.

It is possible to observe in table 5.9 that the coherence length, l_ϕ, decreases with increasing temperature. In fact, for two-dimensional systems, the power-law dependence of coherence length is $l_\phi \sim T^{-1/2}$, while for 3D systems the law changes to $l_\phi \sim T^{-3/4}$ [55].

From this point further, in order to obtain comparable results between the samples from batches II and III, the fit was performed using only the data up to 0.5 T^2. However, this causes the background to have little influence and the background exponent b loses physical significance (although it still improves the results for l_ϕ). This fit is shown in Figure 5.26b.

In this case, it is possible to observe the decrease of l_ϕ from (231 ± 2) nm to (96 ± 2) nm as the temperature increases from 1.8 K to 10 K. The power-law fit of l_ϕ with temperature illustrated in Fig. 5.27 yields $l_\phi \sim T^{-0.519(3)}$, which corroborates that the WAL effect at low magnetic fields originated from bidimensional surfaces.

5.7.3.2   Shubnikov-de Haas Oscillations

In Figure 5.25, at 1.8 K, it is possible to observe traces of oscillations in the resistivity, more visible at high fields. To study the phenomenon, we directly subtracted the model (HLN + power-law background) for fields $B > 1$ T, obtaining the oscillatory part of ΔG

---

[2]As can be seen in the next section, if higher values of the field were used, that would cause extreme loss in the goodness of the fitting.

visible in Figure 5.28(a). The same figure illustrates that this effect tends to disappear with the increasing temperature.

The conductance has periodic maximums and minimums with $^1/_B$.

The Lifshitz–Onsager equation discussed in 3.2 is given by:

$$2\pi(n + \gamma) = \pi k_{\mathrm{F}}^2 \frac{\hbar}{eB}, \tag{5.4}$$

where $\hbar$ is the reduced Planck constant, e is the electronic charge, B the applied magnetic field, (πk_F^2) the cross-sectional area of the Fermi surface perpendicular to B with radius equivalent to the Fermi wave vector k_{F}, n the Landau level (LL) index, and γ is the phase of the SdH oscillations, given by eq. 3.10.

When plotting the LL fan diagram (plot of n versus $^1/_B$) (Fig. 5.29), the phase of the SdH oscillations γ can be determined following eq. 5.4. Integer values of n are assigned to minimums of ΔG, while $n + ^1/_2$ values are assigned to maximums.

The linear fitting for the data retrieved at 1.8 K yields a slope $B_{\mathrm{F}} = 35 \pm 2$ T and an intercept on n-axis $\gamma = 0.1 \pm 0.4$. Thus, since for conventional metals γ should be $^1/_2$, the experimentally determined γ suggests the presence of non-trivial π Berry phase.

Furthermore, for a 2D topological surface without spin degeneracy, the carrier density and the Fermi vector are related by

$$n_{2D} = \frac{1}{(2\pi)^2} \pi k_{\mathrm{F}}^2 = \frac{k_{\mathrm{F}}^2}{4\pi} \tag{5.5}$$

and for a 3D Fermi surface where the spin degeneracy is taken into account, they are related by

$$n_{3D} = \frac{2}{(2\pi)^3} \frac{4}{3} \pi k_{\mathrm{F}}^2 = \frac{k_{\mathrm{F}}^3}{3\pi^2} \tag{5.6}$$

Therefore, from the slope $B_{\mathrm{F}} = \frac{\hbar}{2e} k_{\mathrm{F}}^2$ one can determine the Fermi wave vector, $k_{\mathrm{F}} = 0.0328\,\text{Å}^{-1}$ and, from eq. 5.5, the surface carrier density $n_{2D} = 8.56 \times 10^{11}\,\text{cm}^{-2}$. On the other hand, for a 3D system with $k_{\mathrm{F}} = 0.0328\,\text{Å}^{-1}$, the carrier density can be calculated to be $n_{3D} = 1.91 \times 10^{18}\,\text{cm}^{-3}$.

Moreover, the carrier density calculated from the Hall effect ($n_{\mathrm{H}} = 1.76 \times 10^{18}\,\text{cm}^{-3}$) agrees with the bulk density obtained from the SdH oscillations for 3D systems, which suggests that the quantum oscillations can originate from the bulk states. This effect was reported by several authors [33, 58], where the carrier density has indeed much higher values ($n_{\mathrm{H}} \sim 10^{18}\,\text{cm}^{-3}$), indicating the relevance of residual bulk carriers.

However, it should be pointed out that the discussion above only suggests the 3D
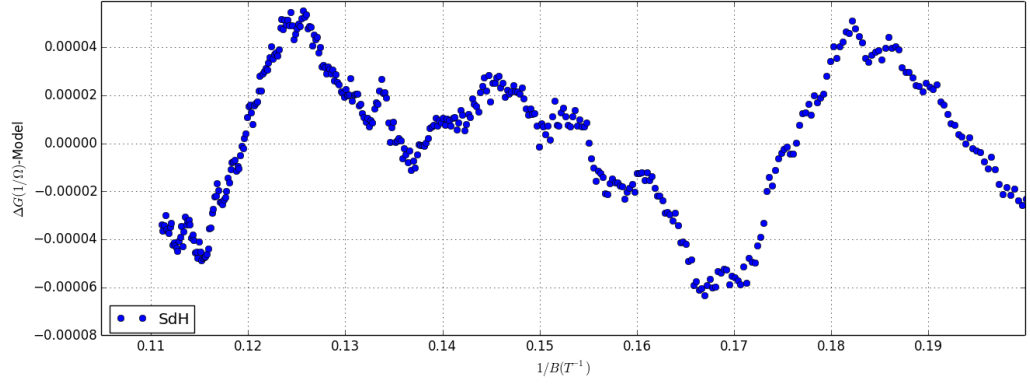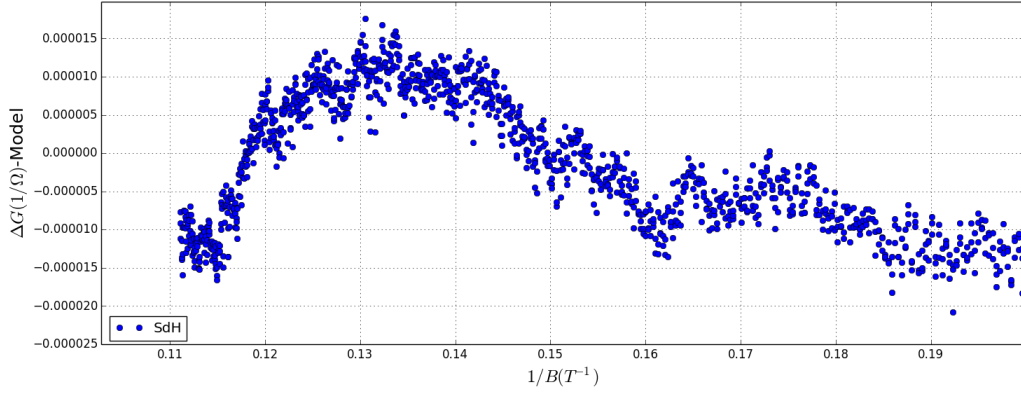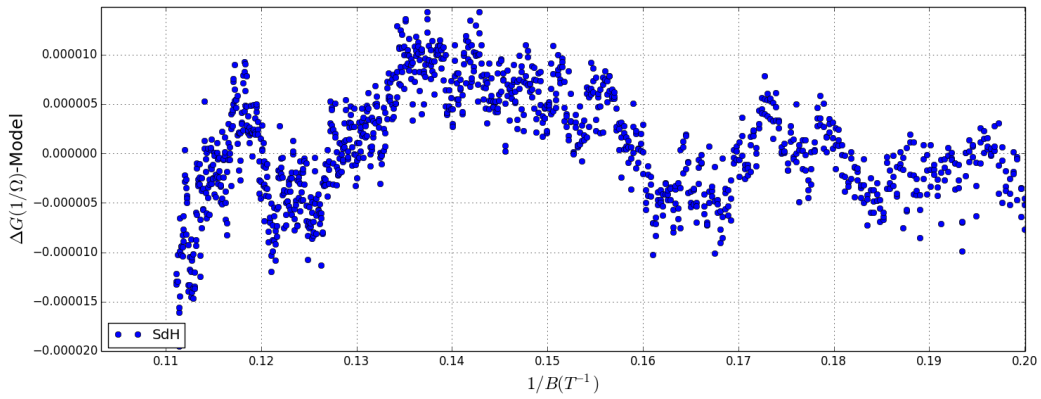
Figure 5.28: Shubnikov-de Haas oscilations for the sample $Bi_2Se_3 - II$ at (a) 1.8 K, (b)15 K, (c) 25 K.
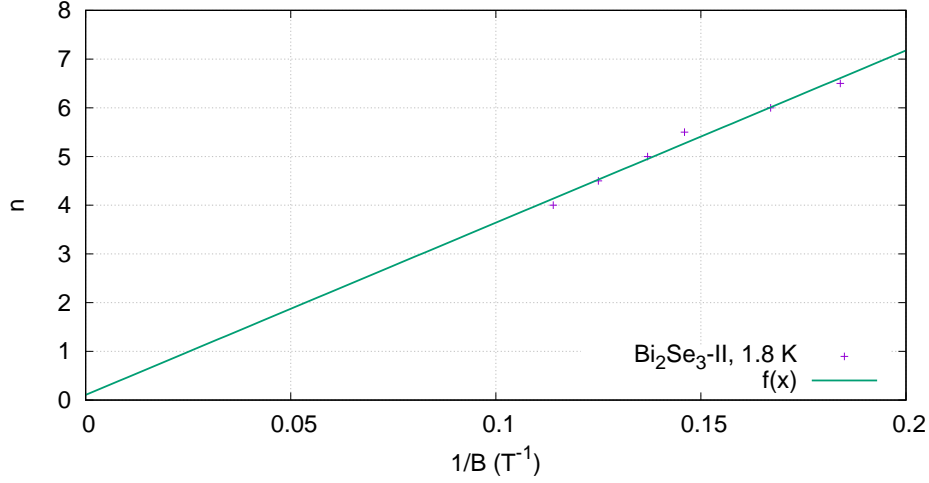
Figure 5.29: Landau level fan diagram for SdH oscillations and linear fitting of the periodic maxima and minima as a function of the index n. The fitting yields an intersect $\gamma = 0.1 \pm 0.4$.

origin of the SdH oscillations. The nature of the oscillations should be tested by its dependence on the angle. If the oscillation frequency, F, changes as $\sim 1/\cos\theta$ (for a wide range of θ), a 2D origin is expected. Moreover, the 2D nature is supported if the SdH oscillations disappear for $\theta = 90°$. Unfortunately, we did not have access to a rotator and therefore this analysis could not be performed with the available instrumental setup.

5.8 Transport properties of Bi₂Se₃ - Batch III

5.8.1 Resistance vs Temperature

When measuring the longitudinal resistance for sample Bi₂Se₃- Batch III, we noticed that the resistance would decrease with time. Even when the sample was placed inside the PPMS chamber, in a controlled environment and stable temperature of 300 K, the resistance still decreased, as can be verified in Figure 5.30. We attributed those results to the diffusion of silver (originated from the contacts) in the Bi₂Se₃ structure. This phenomena was reported by several authors [59, 60], where it is indicated that the deposition of silver atoms on the surface of Bi₂Se₃ would lead to an intercalation of those atoms between the quintuple layers, in the van der Waals gaps.

The low values observed for the resistance of sample III and the positive slope, $dR/dT > 0$, indicate a more metallic behavior, compared to sample II. Our guess is that the resistance is indeed affected by the diffusion of the metallic atoms, and the measured
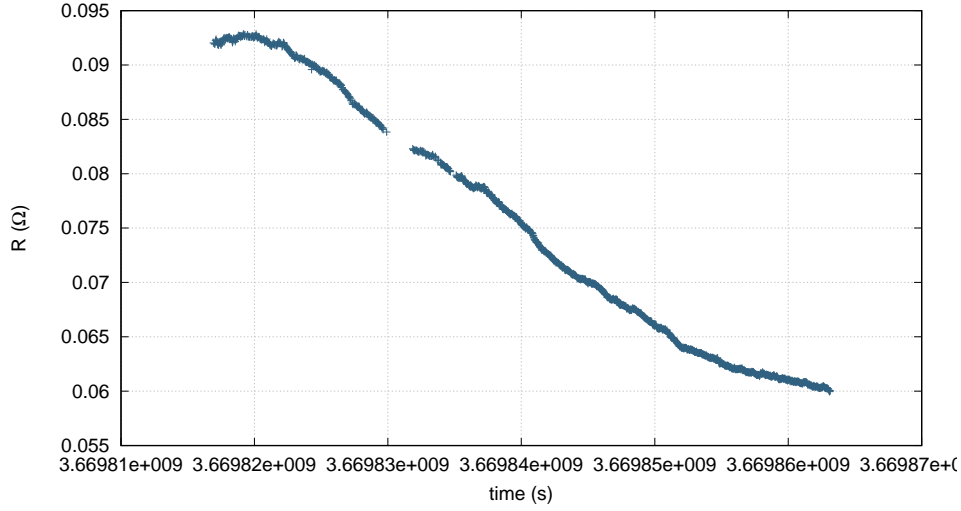
Figure 5.30: Time dependence of the resistance for sample III, at 300 K in a controlled environment.
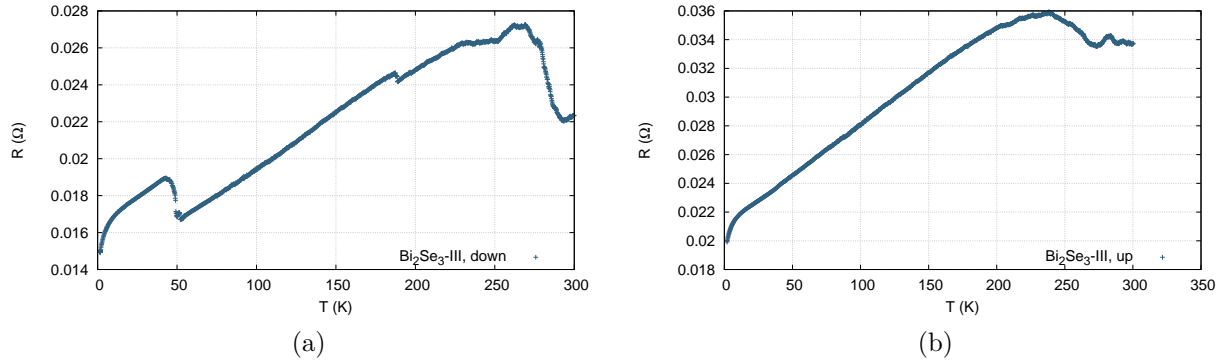
Figure 5.31: Temperature dependent resistance for sample III, (a) decreasing the temperature and (b) increasing the temperature.

resistance decrease arises from the increased electron concentration due to the diffusion of the silver atoms. An unexpected behavior for semiconductors was found at low temperatures, where the resistance decreased abruptly for $T < 10\,\mathrm{K}$. Furthermore, a rather unusual histeretic effect was corroborated in several cooling and heating cycles (Fig. 5.31(a) and (b)). When the temperature is decreased, some effects appear at around 50 K and 180 K. This anomalous hysteresis in the resistance is not really understood and we can only guess that it can be due to a damaged contact.
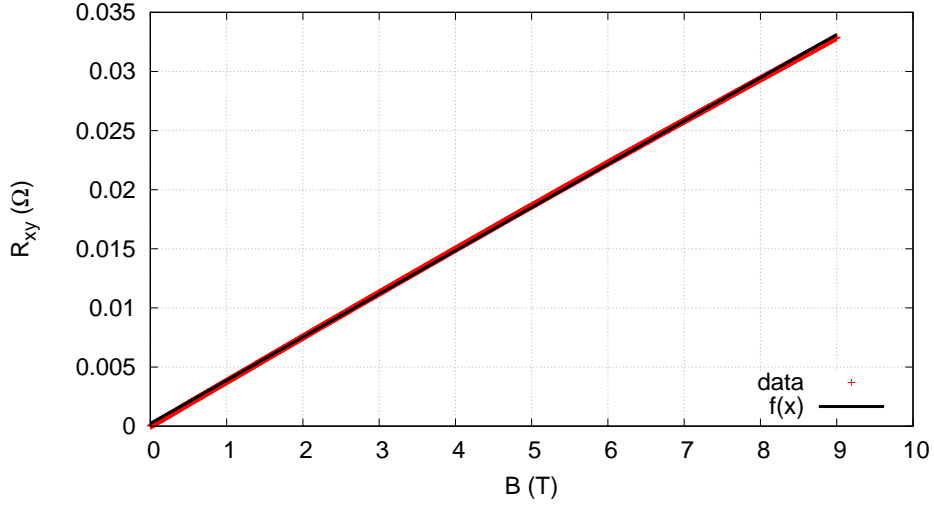
Figure 5.32: Linear fitting and anti-symmetrization of the Hall effect for sample III.

5.8.2 Hall Effect

Figure 5.32 shows the Hall effect for the sample Bi$_2$Se$_3$ − III at 1.8 K, suggesting that the main carriers are electrons. The slope $m = (36563 \pm 9) \times 10^{-7}\,\Omega\mathrm{T}^{-1}$ and width of the pellet $w = (0.20 \pm 0.05)\,\mathrm{mm}$ yield a carrier concentration of $n_{\mathrm{H}} = 8.53 \times 10^{18}\,\mathrm{cm}^{-3}$ in a one-band model. This is a higher carrier density than that of sample II, indicating a more metallic behavior, as already expected from the discussion in 5.8.1.

5.8.3 Magnetoresistivity

5.8.3.1 Weak anti-localization

The magnetoresistance at 1.8 K for the sample III is illustrated in Figure 5.33. It can be observed that the WAL effect is much weaker and the data are notoriously asymmetric. Once again, we performed a symmetrization of the data in order to eliminate the error introduced by the misalignment of the contacts.

For the study of weak anti-localization effect in sample Bi$_2$Se$_3$ - Batch II, we considered that $\rho_{xx} \gg \rho_{xy}$ and therefore we could write $G \sim 1/R_{xx}$. In this case, however, ρ_{xx} and ρ_{xy} have the same order of magnitude, and the condition would not hold. From 5.2, we know that the conductivity and resistivity are related by

$$\sigma_{xx} = \frac{\rho_{xx}}{\rho_{xx}^2 + \rho_{xy}^2}. \tag{5.7}$$
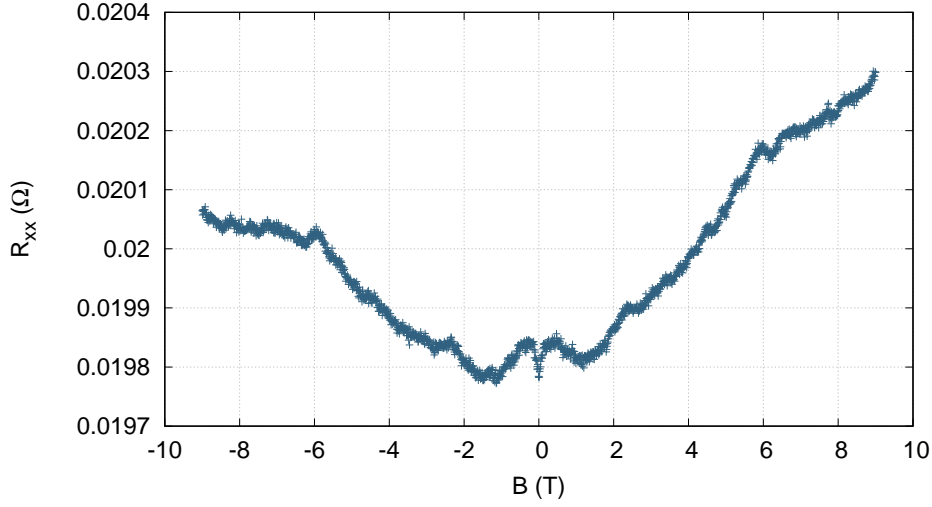
Figure 5.33: Magnetoresistance at 1.8 K for the sample Bi_2Se_3−III. Note that the WAL effect is still present, although is is less significant.

The change in conductance, ΔG will now be given by

$$\Delta G = \frac{R_{xx}(B)}{R_{xx}(B)^2 + (mB)^2} - \frac{R_{xx}(0)}{R_{xx}(0)^2}, \tag{5.8}$$

where m is the slope obtained from the fit of the Hall effect data and, therefore, $mB = R_{xy}$.

In the present sample, we measured the distance between the two voltage contacts and the width of the channel and obtained, respectively, $L = 1.10(5)\,\text{mm}$ and $W = 2.60(5)\,\text{mm}$.

When we did the plot of ΔG calculated as eq. 5.8 in the entire magnetic field range (up to 9 T), we noticed that the oscillations were no longer visible and the resultant data were significantly changed by the term $(mB)^2$. The plot described almost nothing but the background, as the term in B^2 gained too much relevance. This, of course, is not in our interest. Therefore, we tried to perform the fit of the HLN formula + background to the region of $0 − 0.5$ T, since B would not be that prominent and it is, indeed, the region where the dip is notorious (see Fig. 5.33). This analysis led to a good fit and coherent values for l_ϕ, although α had values far from the expected $\alpha = -1$, as can be confirmed in Figure 5.34. The plot of the coherence length with temperature for this analysis is presented in Figure 5.34(b). The fit yields $l_\phi \sim T^{-0.5(2)}$, which is still close to the desired value for a 2D system.

Although the previous discussion led to acceptable results, one can see that the shape of the curve ΔG is still affected by the term $(mB)^2$, even in small fields. Therefore,

(a)   (b)

Figure 5.34: (a)Fitting of the HLN model + background, accounting for the R_{xy} component, to the data of sample III at 1.8 K, up to 0.5 T. The fit yields $\alpha = (-43 \pm 6) \times 10^2$ and $l_\phi = (148 \pm 12)$ nm. (b)Power-law fit of coherence length, l_ϕ, with temperature for the sample III. The fit yields $T^{-0.5(2)}$.

(a)   (b) d = -0.624588 +/- 0.07258
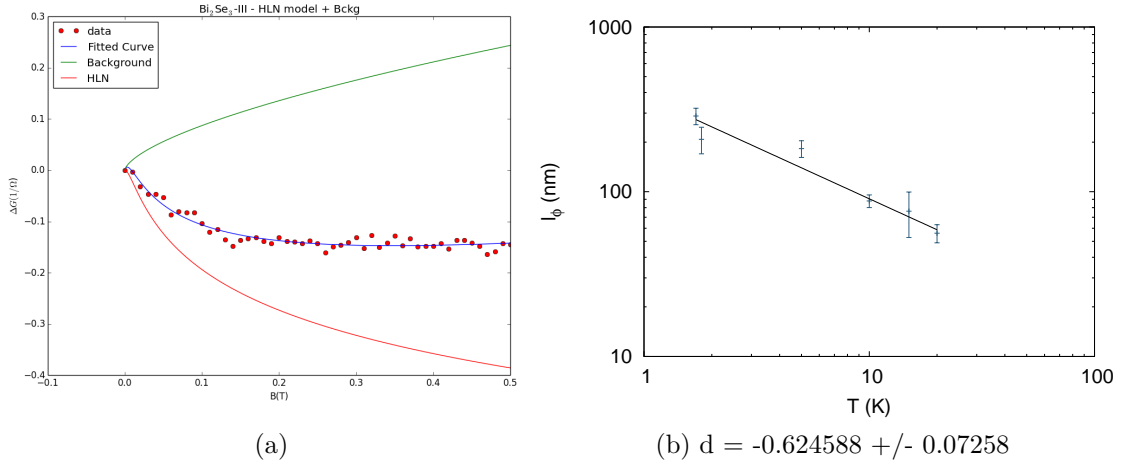
Figure 5.35: (a)Fitting of the HLN model + background, with $G_{xx} = 1/R_{xx}$, to the data of sample III at 1.8 K, up to 0.5 T. The fit yields $\alpha = (-44 \pm 6) \times 10^2$ and $l_\phi = (21 \pm 4) \times 10^1$ nm. (b)Power-law fit of coherence length, l_ϕ, with temperature for the sample III. The fit yields $T^{-0.62(7)}$.

(a)   (b)
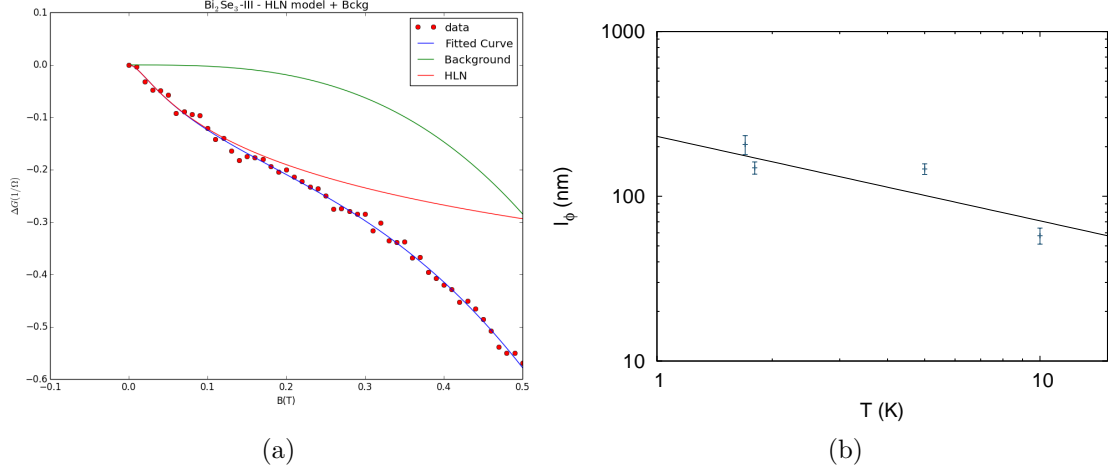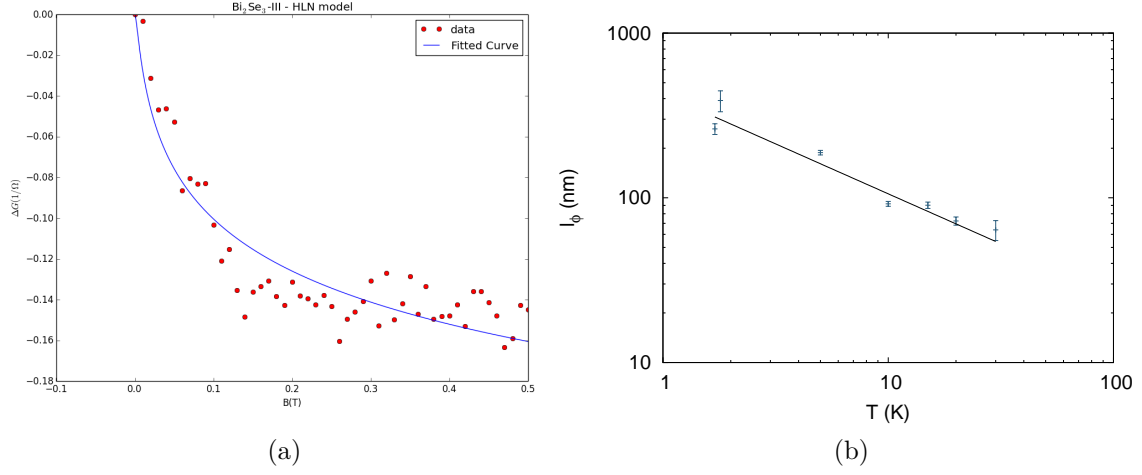
Figure 5.36: (a)Fitting of the HLN model only, with $G_{xx} = 1/R_{xx}$, to the data of sample III at 1.8 K, up to 0.5 T. The fit yields $\alpha = (-132 \pm 11) \times 10^1$ and $l_\phi = (39 \pm 6) \times 10^1$ nm. (b)Power-law fit of coherence length, l_ϕ, with temperature for the sample III. The fit yields $T^{-0.61(9)}$.

we tried to calculate G as in the previous sample ($G = 1/R_{xx}$), since for $B \sim 0$ T, that should be a good approximation. Once again the fitting was performed up to 0.5 T (see Fig. 5.35(a) for the fit at 1.8 K) and the plot of l_ϕ vs T is presented in Figure 5.35(b). The dependence of the coherence length on temperature revealed to be $l_\phi \sim T^{-0.62(7)}$. However, it is possible to observe in Fig. 5.35(a) that, despite the good fit, the background has an unusual shape and relevance for small fields, and it is more artificial than desired. In order to overcome this, the fitting was repeated, accounting for the HLN model only. This led to the results illustrated in Figures 5.36(a) and 5.36(b), giving a behavior described by $l_\phi \sim T^{-0.61(9)}$.

5.8.3.2   Shubnikov-de Haas Oscillations

The sample $Bi_2Se_3 - III$ also exhibits oscillations in the magnetoresistance (see Fig. 5.37) that disappear at high temperatures. Following the same procedure as explained for sample II (here we used the approximation $G \sim 1/R_{xx}$, since the inclusion of R_{xy} would make the SdH oscillations irrelevant) and performing the fitting in the LL fan diagram (Fig. 5.38), one finds the interception with the n-axis $\gamma = 0.1 \pm 0.5$ and slope $B_F = (130 \pm 4)$ T. The former indicates once again the presence of a non-trivial π Berry phase, while from the latter it is possible to determine the Fermi wave vector, $k_F = 0.063 \, \text{Å}^{-1}$. Using equations 5.5 and 5.6, one can calculate the carrier densities for two and three dimensions, $n_{2D} = 3.16 \times 10^{12} \, \text{cm}^{-2}$ and $n_{3D} = 8.44 \times 10^{18} \, \text{cm}^{-3}$.
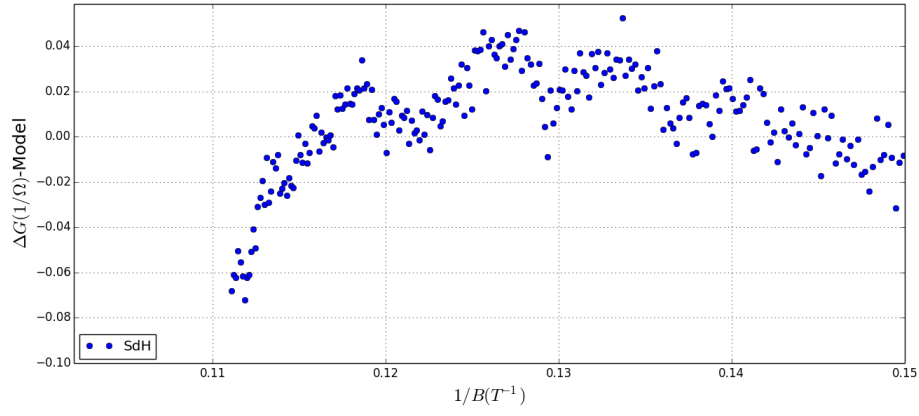
Figure 5.37: Shubnikov-de Haas oscillations for the sample Bi$_2$Se$_3$ − III at 1.8 K.
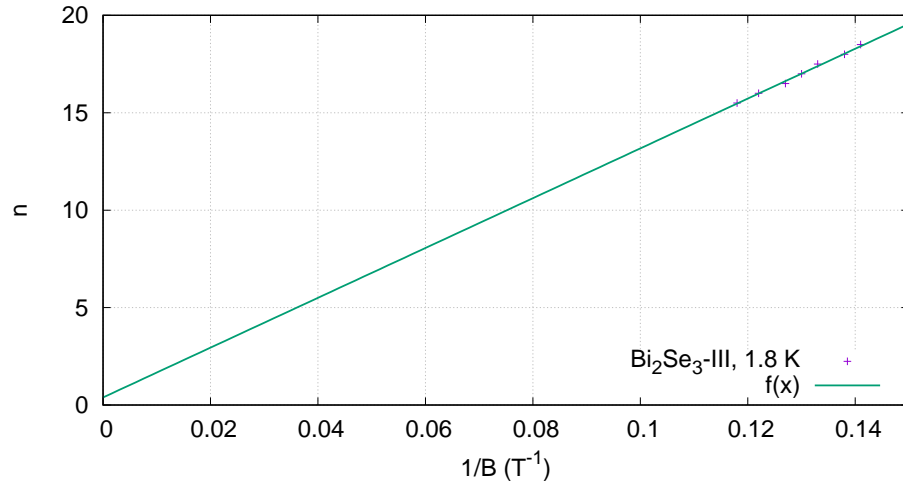
Figure 5.38: Landau level fan diagram for SdH oscillations and linear fitting of the periodic maxima and minima as a function of the index n. The fitting yields an intersect $\gamma = 0.1 \pm 0.5$.

As discussed for sample II, there is a good agreement between the carrier density obtained from the Hall effect ($n_\mathrm{H} = 8.53 \times 10^{18}\,\mathrm{cm^{-3}}$) and the one obtained from the SdH oscillations considering a three-dimensional system. This suggests that the quantum oscillations have a 3D nature, although that cannot be confirmed without further studies.

5.9   Transport properties of Bi$_2$Se$_3$ - Batch III (2)

As discussed in the previous section, the resistance in sample III varied considerably with time at a constant temperature and protected environment (He exchange gas). We attributed this effect to the involuntary diffusion of silver into the sample. We tried to overcome this by using a sputtering of gold and gadolinium on the other half of the pellet, in four small circles only, and placing the contacts on those spots. We expected that this would limit the diffusion of the silver throughout the sample.

5.9.1   Resistance vs Temperature

In Figure 5.39(a) the evolution of the resistance with time is portrayed. Although there still is a decrease of the resistance with time, it is not so prominent as before. The resistance values differ by 10^2 from those of sample III. Keeping in mind that it is the same pellet, a difference of this magnitude could not be caused by the contacts only. It is our belief that the diffusion of silver was not so efficient in the case of sample III (2) (either due to the sputtering of Au and Gd or to the lower time of exposure of the sample with the contacts before the measurements were performed), causing a more regular behavior with temperature. Indeed, the dependence of the resistance on temperature (Fig. 5.39(b)) revealed that there is, as in sample II, an upturn in the resistance for small temperatures.

5.9.2   Magnetoresistivity

5.9.2.1   Weak anti-localization

The weak anti-localization effect is now much more prominent than in sample III, without the sputtering procedure, as can be seen in Figure 5.40. The symmetrization of the data was performed and the distances L and W measured, giving $L = 1.20(5)\,\mathrm{mm}$ and $W = 1.40(5)\,\mathrm{mm}$. G was calculated as $G = 1/R_{xx}$, since R_{xx} now has values $\sim 1\,\Omega, \gg R_{xy}$ usually measured. The fitting of the HLN model + background (described previously for sample II) is shown in Figure 5.41(a) at 1.8 K. The obtained parameters
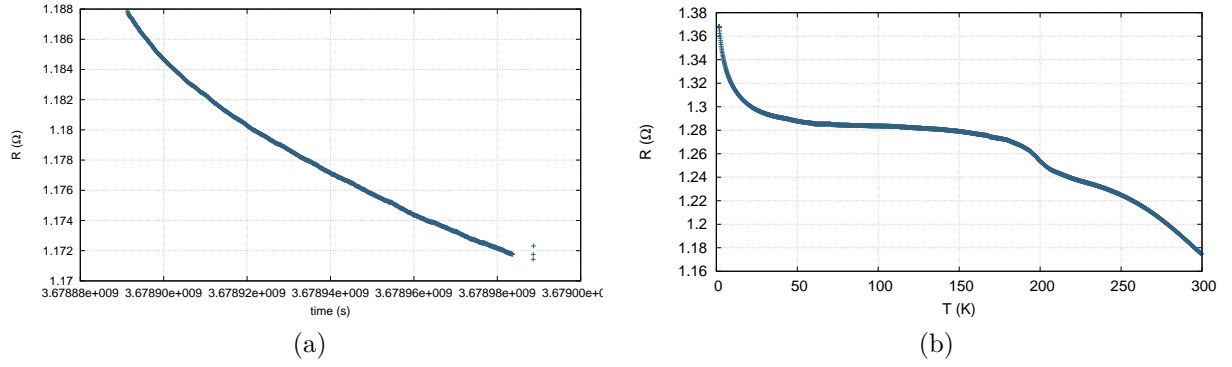
Figure 5.39: Time (a) and temperature (b) dependence of the resistance for sample III(2). Note that the resistance measured at 300 K still decays with time, although it is less relevant.
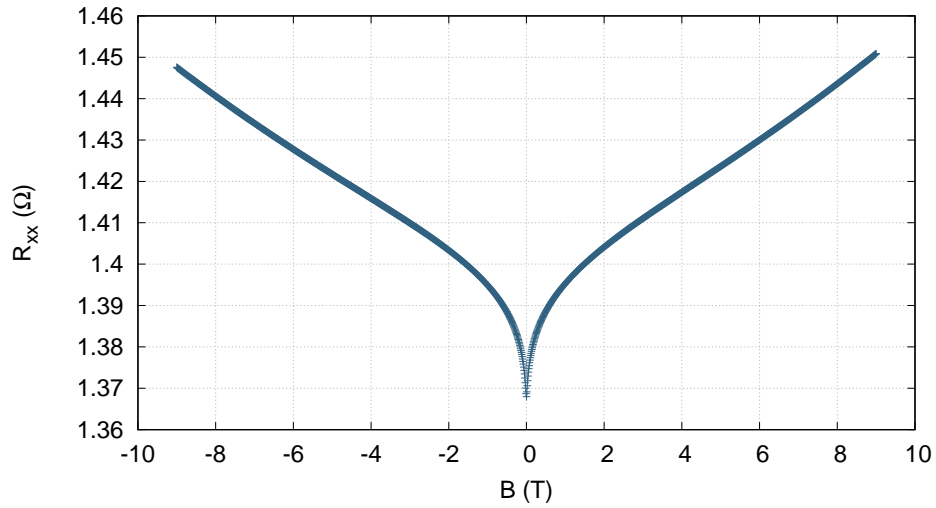
Figure 5.40: Magnetoresistance at 1.8 K for the sample Bi$_2$Se$_3-$ III(2). The WAL cusp is now much more prominent, although no SdH oscillations are visible.

(a) (b)
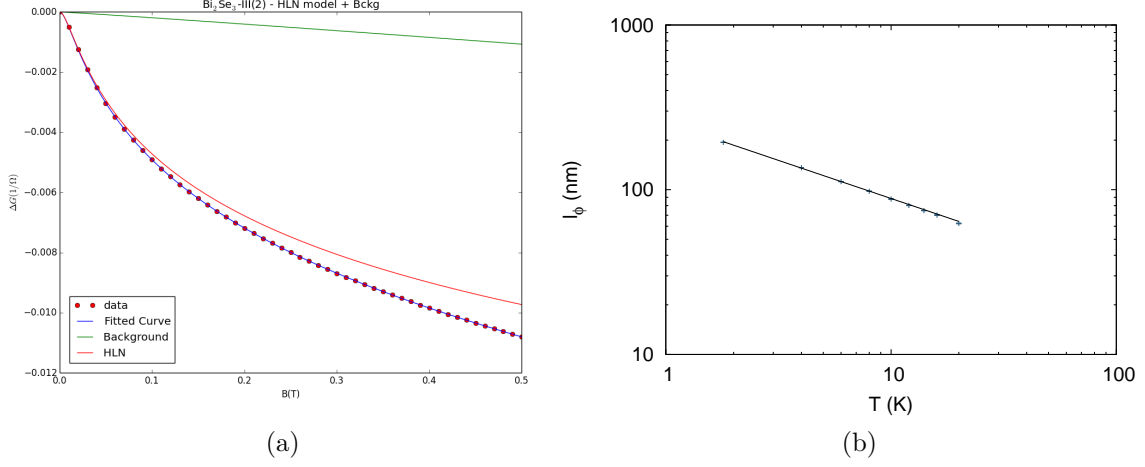
Figure 5.41: (a)Fitting of the HLN model + background, with $G = 1/R_{xx}$, to the data of sample III(2) at 1.8 K, up to 0.5 T. The fit yields $\alpha = -240.0 \pm 0.9$ and $l_\phi = (193.96 \pm 0.17)$ nm. (b)Power-law fit of coherence length, l_ϕ, with temperature for the sample III(2). The fit yields $T^{-0.463(5)}$.
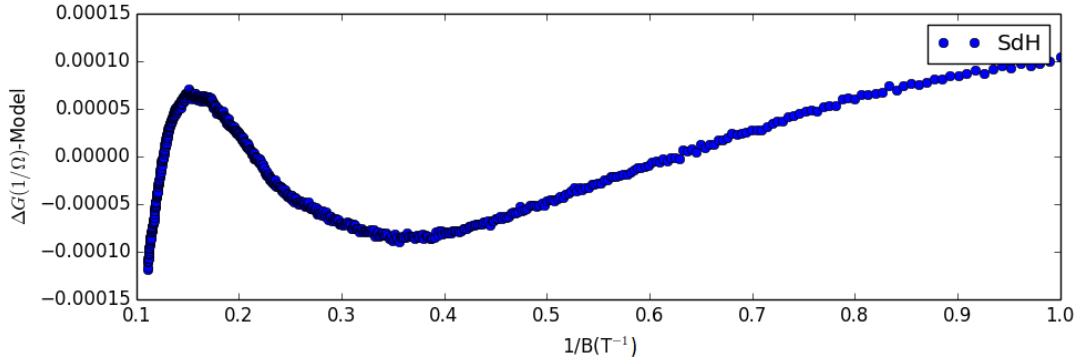
Figure 5.42: Shubnikov-de Haas oscillations for the sample $Bi_2Se_3 - III(2)$ at 1.8 K.

are $\alpha = -240.0 \pm 0.9$, $l_\phi = (193.96 \pm 0.17)$ nm and $b = 1.06 \pm 0.02$, with α, once again, extremely deviated from the expected.

The plot of the coherence length with the temperature is presented in Figure 5.41(b), where the fit is also illustrated. The values for l_ϕ were obtained from the fits of the magnetoresistance at several temperatures for fields up to 0.5 T. The fit gives a law of $l_\phi \sim T^{-0.463(5)}$.

5.9.2.2 Shubnikov-de Haas Oscillations

Although the WAL effect is much more visible in this sample, the SdH oscillations could not be observed when looking directly to the magnetoresistance (Fig. 5.40). Even

when subtracting the model from the ΔG data, we obtained only one maximum and one minimum (see Figure 5.42), which did not allow to perform a LL fan diagram and, consequently, calculate the carrier density for the cases of two and three-dimensional systems. In order to take some conclusions, we would need to perform magnetoresistance measurements up to higher fields, where the SdH oscillations are, generally, more relevant.

Indeed, it is clear that a higher resistance (reduced electron concentration) of the sample makes it harder to observe SdH oscillations. A higher resistance means, however, that the sample is closer to the desired insulator (semiconductor) behavior.

Chapter 6

Conclusion and Further Work

Although some drawbacks were encountered during the work reported in this thesis, the main goals were attained. The synthesis via a microwave-assisted method of Bi_2Se_3 granted two batches of a nanomaterial with topological insulator phases, verified by their transport properties.

The synthesis of $Bi_2Se_{3-x}Te_x$, $x = 0.1$, 0.3, 0.5 and Bi_2Te_3, however, were not successful. Despite the several synthesis in slightly different conditions, the desired compound was never obtained (in the case of $Bi_2Se_{3-x}Te_x$) or it was not the majority phase (for Bi_2Te_3). Also, even the synthesis of Bi_2Se_3 led to two batches of a highly pure compound (I and III) and one with impurity phases (II). Since all synthetic conditions were kept unchanged, the likely explanation for obtaining different results may rely on the microwave oven. In fact, the temperature control is only active in one of the vessels and the inhomogeneous microwave field may impact on the synthesis. This problem should be addressed in future work.

Regarding the electrical measurements performed on both samples of Bi_2Se_3 (batches II and III), we can conclude that the carrier concentrations calculated from the Hall effect ($n_H = 1.76 \times 10^{18}\,cm^{-3}$ and $n_H = 8.53 \times 10^{18}\,cm^{-3}$, respectively) are higher than the usually reported concentrations for a Bi_2Se_3 topological insulator. This suggests that the bulk conducting states contribute to the transport properties. Even if such conducting states should not exist in an insulator, this behavior is commonly reported, and has caused many problems to the study of these materials in the past. Unfortunately, we could not produce samples with a sufficiently high resistivity to be classified as "insulators". Furthermore, for sample Bi_2Se_3 - Batch II, we have found that the temperature dependence of the resistance followed the expected behavior for this material. The most interesting result of this work was the observation of a clear signal of a weak anti-localization effect, strong indicator of the presence of topological surfaces. Indeed,

the fit of the HLN formula to the WAL data yields values of the phase coherence length which agree with the reported, expected values. Moreover, the dependence of this length with temperature gave further evidence of the two-dimensional origin of that quantum effect. Therefore, we came to the conclusion that the polycrystalline sample in study has indeed topologically protected surface states that are robust against structural defects and non-magnetic impurities. This is a remarkable achievement, since studies of topological insulators are usually performed on single crystals. We are only aware of a very recent study that reports the existence of robust surface states in polycrystalline Bi_2Te_3 [61].

For sample Bi_2Se_3 - Batch III, the resistance dependence of temperature presented odd phenomena that, we believe, can be at least partially explained by the diffusion of silver atoms from the contacts into the compound structure. This was reported by several studies, that indicate that Ag is incorporated in the van der Waals gaps between the quintuple layers of Bi_2Se_3, although no studies of the alterations in the transport properties were found. The resistance for this sample had much smaller values, consistent with the hypothesis that the silver atoms are relevant to the measured properties. Also in this train of thought, we can explain the reason why the WAL effect was less prominent, since the two-dimensional surface states would now have less relevance than in sample II. The study of the HLN fit depending on the formula used to calculate the conductance G led to different behaviors of the coherence length with the temperature, although all the exponents were relatively close to the expected $l_\phi \sim T^{-0.5}$.

Moreover, we can conclude that the sputtering of Au and Gd on the surface of the pellet (sample III(2)) did not interrupt the diffusion of silver, although its effect was less significant. The dependence of the measured resistance with temperature had a semiconductor behavior in the majority of the temperature range, and the resistance values were higher than in the previous sample. The WAL effect was also observed, and the dependence of the phase coherence length with the temperature suggested, once again, the existence of two-dimensional surface states.

Regarding the quantum oscillations observed in the magnetoresistance for both sample II and III, they respected the periodicity in $1/B$, and the analysis of the LL fan diagram suggested that they could have a 3D origin, i.e., that they are originated from the bulk states. Although this hypothesis needs further studies to be confirmed, this result is also in agreement to the reported studies of Bi_2Se_3 with similar carrier concentrations. For sample III(2), however, the quantum oscillations were not visible in the range of magnetic field applied. In order to take any conclusions about this, a larger magnetic field would be needed.

Concerning future work, we can suggest that a larger range of dopants may be incorporated into the structure of Bi_2Se_3, and its consequences on the transport properties of the synthesized samples can be studied. Furthermore, if a rotator (which offers the possibility to rotate the sample in the applied magnetic field) becomes available in a near future, that would further highlight the origin (2D or 3D) of this phenomena.

References

[1] K. v. Klitzing, G. Dorda, and M. Pepper. New method for high-accuracy determination of the fine-structure constant based on quantized hall resistance. *Phys. Rev. Lett.*, 45:494–497, Aug 1980.

[2] F. D. M. Haldane. Model for a quantum hall effect without landau levels: Condensed-matter realization of the "parity anomaly". *Phys. Rev. Lett.*, 61:2015–2018, Oct 1988.

[3] Shun-Qing Shen. Spin transverse force on spin current in an electric field. *Phys. Rev. Lett.*, 95:187203, Oct 2005.

[4] Shuichi Murakami, Naoto Nagaosa, and Shou-Cheng Zhang. Spin-hall insulator. *Phys. Rev. Lett.*, 93:156804, Oct 2004.

[5] Joel E. Moore. The birth of topological insulators. *Nature*, 464(7286):194–198, March 2010.

[6] C. L. Kane and E. J. Mele. Z_2 topological order and the quantum spin hall effect. *Phys. Rev. Lett.*, 95:146802, Sep 2005.

[7] B. Andrei Bernevig, Taylor L. Hughes, and Shou-Cheng Zhang. Quantum spin hall effect and topological phase transition in hgte quantum wells. *Science*, 314(5806):1757–1761, 2006.

[8] M. Konig, S. Wiedmann, C. Brune, A. Roth, H. Buhmann, L. W. Molenkamp, X.-L. Qi, and S.-C. Zhang. Quantum spin hall insulator state in HgTe quantum wells. *Science*, 318(5851):766–770, November 2007.

[9] Liang Fu, C. L. Kane, and E. J. Mele. Topological insulators in three dimensions. *Phys. Rev. Lett.*, 98:106803, Mar 2007.

[10] Shuichi Murakami. Phase transition between the quantum spin hall and insulator phases in 3d: emergence of a topological gapless phase. *New Journal of Physics*, 9(9):356, 2007.

[11] Shun-Qing Shen. *Topological Insulators*, volume 174 of *Springer Series in Solid-State Sciences.* Springer-Verlag Berlin Heidelberg, 1 edition, 2012.

[12] Liang Fu and C. L. Kane. Topological insulators with inversion symmetry. *Phys. Rev. B*, 76:045302, Jul 2007.

[13] Hsieh et al. A topological dirac insulator in a quantum spin hall phase. *Nature*, 452:970–974, 2008.

[14] M. Z. Hasan and C. L. Kane. *Colloquium* : Topological insulators. *Rev. Mod. Phys.*, 82:3045–3067, Nov 2010.

[15] Tsuneya Ando, Takeshi Nakanishi, and Riichiro Saito. Berry's phase and absence of back scattering in carbon nanotubes. *Journal of the Physical Society of Japan*, 67(8):2857–2862, aug 1998.

[16] Yoichi Ando. Topological insulator materials. *Journal of the Physical Society of Japan*, 82(10):102001, 2013.

[17] M. V. Berry. Quantal phase factors accompanying adiabatic changes. *Proceedings of the Royal Society of London A: Mathematical, Physical and Engineering Sciences*, 392(1802):45–57, 1984.

[18] D. J. Thouless, M. Kohmoto, M. P. Nightingale, and M. den Nijs. Quantized hall conductance in a two-dimensional periodic potential. *Phys. Rev. Lett.*, 49:405–408, Aug 1982.

[19] Liang Fu and C. L. Kane. Time reversal polarization and a Z_2 adiabatic spin pump. *Phys. Rev. B*, 74:195312, Nov 2006.

[20] C. L. Kane and E. J. Mele. Quantum spin hall effect in graphene. *Phys. Rev. Lett.*, 95:226801, Nov 2005.

[21] P. W. Anderson. Absence of diffusion in certain random lattices. *Phys. Rev.*, 109:1492–1505, Mar 1958.

[22] A. H. Castro Neto, F. Guinea, N. M. R. Peres, K. S. Novoselov, and A. K. Geim. The electronic properties of graphene. *Rev. Mod. Phys.*, 81:109–162, Jan 2009.

[23] Topological insulators. In Marcel Franz and Laurens Molenkamp, editors, *Contemporary Concepts of Condensed Matter Science*, volume 6 of *Contemporary Concepts of Condensed Matter Science*. Elsevier, 2013.

[24] J. E. Moore and L. Balents. Topological invariants of time-reversal-invariant band structures. *Phys. Rev. B*, 75(12):121306, Mar 2007.

[25] Rahul Roy. Topological phases and the quantum spin hall effect in three dimensions. *Phys. Rev. B*, 79:195322, May 2009.

[26] Y. S. Hor, A. Richardella, P. Roushan, Y. Xia, J. G. Checkelsky, A. Yazdani, M. Z. Hasan, N. P. Ong, and R. J. Cava. *p*-type Bi2Se3 for topological insulator and low-temperature thermoelectric applications. *Phys. Rev. B*, 79:195208, May 2009.

[27] James G. Analytis, Ross D. McDonald, Scott C. Riggs, Jiun-Haw Chu, G. S. Boebinger, and Ian R. Fisher. Two-dimensional surface state in the quantum limit of a topological insulator. *Nat Phys*, 6(12):960–964, nov 2010.

[28] Hailin Peng, Keji Lai, Desheng Kong, Stefan Meister, Yulin Chen, Xiao-Liang Qi, Shou-Cheng Zhang, Zhi-Xun Shen, and Yi Cui. Aharonov-bohm interference in topological insulator nanoribbons. *Nature Materials*, dec 2009.

[29] Desheng Kong, Wenhui Dang, Judy J. Cha, Hui Li, Stefan Meister, Hailin Peng, Zhongfan Liu, and Yi Cui. Few-layer nanoplates of Bi2Se3 and Bi2Te3 with highly tunable chemical potential. *Nano Letters*, 10(6):2245–2250, jun 2010.

[30] Hai-Zhou Lu and Shun-Qing Shen. Weak localization and weak anti-localization in topological insulators. In Henri-Jean Drouhin, Jean-Eric Wegrowe, and Manijeh Razeghi, editors, *Spintronics VII*. SPIE-Intl Soc Optical Eng, aug 2014.

[31] Xiao-Liang Qi and Shou-Cheng Zhang. The quantum spin hall effect and topological insulators. *Phys. Today*, 63(1):33–38, jan 2010.

[32] Shinobu Hikami, Anatoly I. Larkin, and Yosuke Nagaoka. Spin-orbit interaction and magnetoresistance in the two dimensional random system. *Progress of Theoretical Physics*, 63(2):707–710, 1980.

[33] Devendra Kumar and Archana Lakhani. Observation of π berry phase in quantum oscillations of three-dimensional fermi surface in topological insulator Bi2Se3. *Phys. Status Solidi RRL*, 9(11):636–640, oct 2015.

[34] Y. Takagaki, B. Jenichen, U. Jahn, M. Ramsteiner, and K.-J. Friedland. Weak antilocalization and electron-electron interaction effects in Cu-doped Bi2Se3 films. *Phys. Rev. B*, 85(11), mar 2012.

[35] Joran Angevaare. The weak anti localization effect due to topological surface states of a Bi1.46Sb0.54Te1.7Se1.3 nanoflake. Master's thesis, University of Amsterdam, July 2014.

[36] Hong-Tao He, Gan Wang, Tao Zhang, Iam-Keong Sou, George K. L Wong, Jian-Nong Wang, Hai-Zhou Lu, Shun-Qing Shen, and Fu-Chun Zhang. Impurity effect on weak antilocalization in the topological insulator Bi2Te3. *Phys. Rev. Lett.*, 106(16), apr 2011.

[37] Haiming Xu, Gang Chen, Rencheng Jin, Dahong Chen, Yu Wang, Jian Pei, Yongqiang Zhang, Chunshuang Yan, and Zhuangzhuang Qiu. Microwave-assisted synthesis of Bi2Se3 ultrathin nanosheets and its electrical conductivities. *CrystEngComm*, 16:3965–3970, 2014.

[38] R. Harpeness and A. Gedanken. Microwave-assisted synthesis of nanosized Bi2Se3. *New J. Chem.*, 27:1191–1193, 2003.

[39] D. Michael P. Mingos and David R. Baghurst. Tilden lecture. applications of microwave dielectric heating effects to synthetic problems in chemistry. *Chem. Soc. Rev.*, 20:1–47, 1991.

[40] Guillaume Viau, Françoise Fiévet-Vincent, and Fernand Fiévet. Monodisperse iron-based particles: precipitation in liquid polyols. *J. Mater. Chem.*, 6(6):1047–1053, 1996.

[41] Song Chen, Kefeng Cai, and Shirley Shen. Synthesis via a microwave-assisted wet chemical method and characterization of Bi2Te3 with various morphologies. *Journal of Electronic Materials*, 45(3):1425–1432, 2016.

[42] Bo Zhou, Yu Zhao, Lin Pu, and Jun-Jie Zhu. Microwave-assisted synthesis of nanocrystalline Bi2Te3. *Materials Chemistry and Physics*, 96(23):192–196, 2006.

[43] O. Palchik, R. Kerner, Z. Zhu, and A. Gedanken. Preparation of Cu2-xTe and HgTe by using microwave heating. *Journal of Solid State Chemistry*, 154(2):530 – 534, 2000.

[44] Peter Zavalij Vitalij Pecharsky. *Fundamentals of Powder Diffraction and Structural Characterization of Materials.* Springer US, 2 edition, 2009.

[45] Bruker. The future-proof in x-ray diffraction (xrd), [Online; accessed 18-July-2016]. https://www.bruker.com/pt/products/x-ray-diffraction-and-elemental-analysis/x-ray-diffraction/d8-advance/overview.html.

[46] Slovakia Department of Experimental Physics, Comenius University. Laboratory of x-ray scattering methods, [Online; accessed 16-July-2016]. http://www.dep.fmph.uniba.sk/mambo/index.php?option=content&task=view&id=259.

[47] Frank Krumeich. Properties of electrons, their interactions with matter and applications in electron microscopy. http://www.microscopy.ethz.ch/.

[48] TESCAN. *Scanning Electron Microscope VEGA 3 SEM*, 2011. Instructions for use.

[49] Bruker Nano GmbH. *Bruker QUANTAX EDS Reference Manual*, 2011. Introduction to EDS analysis.

[50] Quantum Design. *PPMS Dynacool User's Manual*, 4th edition, 2014.

[51] Quantum Design. *PPMS ETO User's Manual*, April 2013.

[52] Quantum Design. Six things and to consider and when making and electrical transport and measurements. In *Applications Newsletter Fall*, 2013.

[53] Haiming Xu, Gang Chen, Rencheng Jin, Dahong Chen, Jian Pei, and Yu Wang. Electrical transport properties of microwave-synthesized Bi2Se3-xTex nanosheet. *CrystEngComm*, 15:5626–5632, 2013.

[54] N. P. Butch, K. Kirshenbaum, P. Syers, A. B. Sushkov, G. S. Jenkins, H. D. Drew, and J. Paglione. Strong surface scattering in ultrahigh-mobility Bi2Se3 topological insulator crystals. *Phys. Rev. B*, 81(24), jun 2010.

[55] Lihong Bao, Liang He, Nicholas Meyer, Xufeng Kou, Peng Zhang, Zhi gang Chen, Alexei V. Fedorov, Jin Zou, Trevor M. Riedemann, Thomas A. Lograsso, Kang L. Wang, Gary Tuttle, and Faxian Xiu. Weak anti-localization and quantum oscillations of surface states in topological insulator Bi2Se2Te. *Sci. Rep.*, 2, oct 2012.

[56] Shira Hollanders. Exploratory research of the 3D topological insulator Bi1.5Sb0.5Te1.3Se1.7 by means of magnetotransport. Master's thesis, University of Amsterdam, July 2012.

[57] Jian Wang, Ashley M. DaSilva, Cui-Zu Chang, Ke He, J. K. Jain, Nitin Samarth, Xu-Cun Ma, Qi-Kun Xue, and Moses H. W. Chan. Evidence for electron-electron interaction in topological insulator thin films. *Phys. Rev. B*, 83(24), jun 2011.

[58] Kazuma Eto, Zhi Ren, A. A. Taskin, Kouji Segawa, and Yoichi Ando. Angular-dependent oscillations of the magnetoresistance in Bi2Se3 due to the three-dimensional bulk fermi surface. *Phys. Rev. B*, 81(19), may 2010.

[59] M. M. Otrokov, S. D. Borisova, V. Chis, M. G. Vergniory, S. V. Eremeev, V. M. Kuznetsov, and E. V. Chulkov. Efficient step-mediated intercalation of silver atoms deposited on the Bi2Se3 surface. *Jetp Lett.*, 96(11):714–718, feb 2013.

[60] M. Ye, S. V. Eremeev, K. Kuroda, M. Nakatake, S. Kim, Y. Yamada, E. E. Krasovskii, E. V. Chulkov, M. Arita, H. Miyahara, T. Maegawa, K. Okamoto, K. Miyamoto, T. Okuda, K. Shimada, H. Namatame, M. Taniguchi, Y. Ueda, and A. Kimura. Relocation of the topological surface state of Bi2Se3 beneath the surface by Ag intercalation. *ArXiv e-prints 1112.5869*, 2011.

[61] H B Zhang, J D Yao, J M Shao, and G W Yang. Robust topological surface transport with weak localization bulk channels in polycrystalline Bi2Te3 films. *Journal of Physics D: Applied Physics*, 49(9):095003, 2016.

Appendix A

Python script

```python
1.  import numpy as np
2.  from math import *
3.  from scipy.special import digamma
4.  import csv
5.  import matplotlib.pyplot as plt
6.  from scipy.optimize import curve_fit
7.  import sys
8.
9.  e = 1.60217662E-19
10. hbar = 1.0545718E-34
11. data = []
12. Col2=[]
13. Col3=[]
14. L = 0.2
15. W = 3.1
16. Rmed=[]
17. Bmed=[]
18. IBmed= []
19. deltaG=[]
20.
21. Bmax = 9.
22.
23. csv.register_dialect('ssv', delimiter=' ', skipinitialspace=True)
24.
25. with open('MR_1.8K_3', 'r') as f:
26.     reader = csv.reader(f, 'ssv')
27.     for row in reader:
28.         floats = [float(column) for column in row]
29.         data.append(floats)
30.
31. for a in data:
32.     if abs(a[1]*0.0001)<=(Bmax+0.001):
33.         Col2.append(a[1]*0.0001)
34.         Col3.append(a[2])
35.
36. #Rmed=(R+ + R-)/2
37. for i in range(len(Col3)/2):
38.     Bdiff = Col2[i]+Col2[-(i+1)]
39.     if abs(Bdiff) >= 0.001:
```

```python
40.         print abs(Bdiff),Col2[i], Col2[-(i+1)], "ERROR!"
41.         sys.exit()
42.     rmed = (Col3[i]+Col3[-(i+1)])/2.
43.     #print "%10.5f %10.5f %10.5f %10.5f %10.5f %10.5f" % (Col2[i],Col2[-(i+1)],Col3[i],Col3[-(i+1)],rmed,Bdiff)
44.     Rmed.append(rmed)
45. Rmed.append(Col3[len(Col3)/2])
46.
47. for k in Rmed:
48.     deltaG.append(1./k-1./Rmed[-1]) #1/R(B)-1/R(0)
49.
50. for j in range(len(Col2)/2):
51.     bmed=(abs(Col2[j])+Col2[-(j+1)])/2.
52.     Bmed.append(bmed)
53. Bmed.append(Col2[len(Col2)/2])
54.
55. col2=np.array(Bmed)
56. col3=np.array(deltaG)
57.
58.
59. #DeltaG Function
60. def G(B, alpha, l,a,b):
61.     g = hiro(B, alpha, l)+backg(B,a,b)
62.     return g
63.
64. #Background
65. def backg(B,a,b):
66.     bkg = a*abs(B)**b
67.     return bkg*W/L
68.
69. #HLN Formula
70. def hiro(B, alpha, l):
71.     bphi = hbar/(4.*e*l**2)
72.     alpha = alpha*e**2/(2.*pi**2*hbar)
73.     g=alpha*(np.log(bphi/abs(B+0.00001))-digamma(0.5+bphi/abs(B+0.00001)))
74.     return g*W/L
75.
76.
77. #Initial guess
78. parametros=[1.,100E-9,-0.0001,1.]


79.
80. B=np.linspace(0., Bmax, 10000)
81.
82. #Fit
83. popt, pcov = curve_fit(G, col2, col3, p0=parametros, maxfev=1000)
84. perr = np.sqrt(np.diag(pcov))
85.
86. #Generate SdH data
87. col4=[]
88. col5=[]
89. for i in range(len(col2)):
90.     B = col2[i]
91.     if B >1.0:
92.         col4.append(col3[i]-G(B,*popt))
93.         col5.append(1./(B))
94.
95. print "Fit Results:"
96.
97. print "Alpha",popt[0], '+-', perr[0]
98. print "Coherence length", popt[1]/1E-9, "nm +-",perr[1]/1E-9
99. print "Background alpha",popt[2],"+-",perr[3]
100.    print "Background exponent",popt[3],"+-",perr[3]
101.
102.    #Plot
103.    plt.subplot(2,1,1)
104.    plt.plot(col2, col3, 'ro',label="data")
105.    plt.title("Bi2Se3-II - HLN model + Bckg")
106.    plt.xlabel("B(T)")
107.    plt.ylabel(r"$\Delta G (1/\Omega)$")
108.    B=np.linspace(0, Bmax, 10000)
109.    plt.plot(B, G(B, *popt), linewidth=3.0, label="Fitted Curve")
110.    plt.plot(B,(backg(B, popt[2],popt[3]))+0.*hiro(100.,popt[0],popt[1]), label="Background")
111.    plt.plot(B,hiro(B, popt[0],popt[1]), label="HLN")
112.    plt.legend(loc='upper right', bbox_to_anchor=(1.1,1))
113.    plt.legend().draggable()
114.
115.    plt.subplot(2,1,2)
116.    plt.xlabel("$1/B(T^{-1})$", fontsize=18)
117.    plt.ylabel(r"$\Delta G (1/\Omega)$-Model", fontsize=18)
```

```
118.    plt.plot(col5,col4,'o',label="SdH")
119.    plt.legend(loc='best')
120.    plt.legend().draggable()
121.    plt.grid()
122.    plt.xticks(np.arange(0.1, 0.21, 0.01))
123.    plt.show()
```